Space-Based High-Resolution Optical-Electronic Systems with Distributed Apertures: Optimization of Design and Operating Parameters

Iouri Tcherniavski

A thesis

in

The Department

of

Electrical and Computer Engineering

Presented in Partial Fulfillment of the Requirements

for the Degree of Doctor of Philosophy at

Concordia University

Montreal, Quebec, Canada

February 2006

Your file Votre référence
ISBN: 978-0-494-16293-4
Our file Notre référence
ISBN: 978-0-494-16293-4

ABSTRACT

Space-Based High-Resolution Optical-Electronic Systems with Distributed Apertures: Optimization of Design and Operating Parameters

Iouri Tcherniavski, Ph.D.
Concordia University, 2006

The optical systems with distributed/sparse apertures have a number of distinctive features in comparison with the systems with monolithic ones. Among them the possible existence of zero-value regions of the optical transfer function (OTF) and the existence of a beam combination system which forms a combined image in a common focal plane. Using the fast-convergent gradient methods for nonlinear constrained optimization, the first feature can result in a suspension of a calculation process if an intermediate solution falls into a zero-value region of the OTF. The second feature gives rise to introducing of some optical errors influencing the quality of the combined image due to the limited accuracy of a beam combination control system. In this thesis, the possibility of applying a gradient optimization method to optimize the distributed/sparse optical aperture configuration is shown. An appropriate approach based on approximation of the step pupil functions with zero-value regions by continuously differentiable functions with non zero-value regions is proposed. This method is demonstrated using examples of circular and annular subapertures. Further, the influence of the residual random image alignment (IA) and optical path difference (OPD) errors of the beam combination system on the OTF is investigated. On the basis of the Fraunhofer approach to the Kirchhoff diffraction

theory, an analytical expression showing the dependence of an instantaneous OTF on the IA and OPD errors is derived. Using the Gaussian probability distributions for the random errors, an analytical expression determining an average OTF (AOTF) depending on statistical parameters of the errors is obtained. The calculation results permit to produce the necessary requirements to the accuracy of the beam combination control system. Finally, possible optimization variants utilizing the step pupil function approximation and the AOTF conception are presented. They use a gradient constrained optimization method with objective functions depending on a signal-to-noise ratio which is expressed in terms of the optimized parameters, in particular, the parameters of the aperture configuration, the effective focal length, and the geometrical parameters of a charge coupled device. Presented results show optimal solutions of the considered optimization problems for the distributed apertures consisting of two and three annular subapertures.

ACKNOWLEDGEMENTS

I would like to thank my Ph.D. supervisor, Dr. Mojtaba Kahrizi, for working with me throughout the last three years and providing the assistantship that supported me during my Ph.D. research; Dr. Kash Khorasani who together with my supervisor has determined the direction of my Ph.D. research.

I am grateful to my professional mentor, Yuriy Th. Yurchenko, the USSR State Prize laureate, DS, who has introduced me to the interesting world of space systems. Unfortunately, he has passed away.

I thank my colleagues in Russia, Evgeny V. Tsukerman, PhD, Boris M. Miller, DS, Sergey N. Bezdidko, DS, for their continuous trust to my professional qualities.

I am also grateful to my friend, Victor Rossokhaty, PhD, for his continued willingness to help me in any situation. Unfortunately, Victor has tragically passed away last year.

Last, I thank my wife, Elena, for her support and sacrifices during all our joint life.

The research was supported in part by Natural Sciences and Engineering Research Council of Canada (NSERC) and the Faculty of Engineering and Computer Science at Concordia University.

CONTENTS

List of Figures

List of Tables

List of Abbreviations

AOTF	Average OTF
BCEO	Bar Chart Equivalents of the Object
CCD	Charge-Coupled Device
GSD	Ground-Sampled Distance
IA	Image Alignment
IMTF	Instantaneous MTF
IOTF	Instantaneous OTF
IQE	Image Quality Equation
IR	Infra-Red
ISS	Image Sensing System
MRF	MTF Reduction Factor
MTF	Modulation Transfer Function
NES	Noise Equivalent Signal
NIIRS	National Imagery Interpretability Rating Scale
OES	Optical-Electronic System
OPD	Optical Path Difference
OS	Optical System
OTF	Optical Transfer Function
PSF	Point Spread Function
SIM	Space Interferometry Mission

SNR	Signal-to-Noise Ratio
TDI	Time Delay and Integration
TIP	Time Integration Procedure
TO	Test-Object
TPF	Terrestrial Planet Finder

List of Symbols

Latin

A_0	area of the aperture
A_n	area of the *n*th subaperture
$AOTF(f_u, f_v, \lambda)$	average spectral OTF
$AOTF_\eta(f, \lambda)$	AOTF depending on η
$B_{bg}(\lambda)$	spectral radiance of the background
$B_E(x, \lambda, R)$	spectral radiance distribution in the object plane
$B_h(\lambda)$	spectral radiance of the atmospheric haze
$B_{ob}(\lambda)$	spectral radiance of the object
C_f	maximal vertical (along the *x*-axis) clock frequency of the CCD
$C_n^2(x)$	refractive index structure function of the atmosphere
c	the light velocity
c_{nm}^{kl}	direction cosines
$D_w(r, \lambda)$	wave structure function of turbulence
d_d	junction depth in the CCD material
d_n	ideal path delay for the beam from the *n*th subaperture
$d_x \times d_y$	single CCD element sensitivity region
d_{x1} and d_{x2}	lower and upper bounds of d_x

d_{y1} and d_{y2}	lower and upper bounds of d_y
E_A	energy incident on the aperture
E_{A_n}	energy incident on the nth subaperture
E_D	density of energy incident on the entrance pupil of the OS
$\mathbf{E}_\nu(z,\Theta)$	the incomplete Weber function
$\mathfrak{I}\{\Phi(.)\}$	some transform of a function $\Phi(.)$
F	effective focal length of the system
F_1 and F_2	lower and upper bounds of F
$\vec{f}$	spatial frequency
$\vec{f}'$	relative spatial frequency
f_{cut}	aperture cutoff frequency
f_{Nq}	minimal spatial Nyquist frequency in the focal plane
f_R	operating spatial frequency in the focal plane
f_{Rx} and f_{Ry}	x- and y-components of the spatial frequency in the ground plane
(f_u, f_v)	u-, v-components of $\vec{f}$
(f_u', f_v')	u-, v-components of the relative spatial frequency
G	the universal gravitational constant
G_c	vector of constraint functions
$G_n(f_u)$	degradation of the signal charge packet after n transfers
g_n, g_{nm}	constraint functions for the optimization problem

H	altitude of observation
h	the Planck's constant
h_0	constant determining the $C_n^2(x)$ altitude distribution
$I_{bg}(f,\lambda)$	spectral irradiance from the background in the focal plane
$I_E(\lambda)$	solar spectral irradiance on the earth surface
$IOTF(f_u, f_v, \lambda)$	instantaneous spectral OTF
$I_h(\lambda)$	spectral irradiance from the atmospheric haze in the focal plane
$I_{ob}(f,\lambda)$	spectral irradiance from the object in the focal plane
$J(.)$	objective function for an optimization problem
$J_n(z)$	the Bessel function of the first kind
$\mathbf{J}_v(z,\Theta)$	incomplete Anger function
K_{Nq}	desirable coefficient determining the relationship between f_R and f_{Nq} $(= f_R / f_{Nq})$
k	wave vector $(= 2\pi/\lambda)$
L_d	diffusion length in the CCD material
$L_E(x,\lambda,R)$	spectral light irradiance distribution in the object plane
L_n	length of the beam combiner lever for the nth subaperture
M	number of TDI lines
M_1 and M_2	lower and upper bounds of M
M_E	Earth's mass
$MRF_A(f,\lambda)$	MRF associated with the atmospheric turbulence

$MTF_{CCD}(f,\lambda,\theta_R)$	CCD MTF
$MTF_{CCD,x}(f_u,\lambda)$	x-component of the CCD MTF
$MTF_{CCD,y}(f_v,\lambda)$	y-component of the CCD MTF
$MTF_{diff}(f,\lambda)$	MTF of the charge diffusion
$MTF_{disc,x}(f_u)$	MTF of the discrete charge motion
$MTF_{\text{int},x}(f_u)$	MTF of the charge integration in the x-direction
$MTF_{\text{int},y}(f_v)$	MTF of the charge integration in the y-direction
$MTF_{OS}(...)$	MTF of the OS
$MTF_{\Delta\vec{V},x}(f_u)$	MTF of the speeds mismatch in the x-direction
$MTF_{\Delta\vec{V},y}(f_v)$	MTF of the speeds mismatch in the y-direction
$MTF_{\varepsilon,x}(f_u)$	MTF of the charge transfer inefficiency
$mtf_{des}(f_u,f_v)$	desirable MTF of the sparse aperture
N	number of subapertures
$N_{bg}(f,\theta_R)$	number of CCD electrons from the image of the background, taking N_{sat} into account
$N_{bg}^{c}(f,\theta_R)$	number of CCD electrons from the image of the background, not taking N_{sat} into account
N_{dc}	dark current shot noise of one CCD element
N_h	number of electrons from the atmospheric haze, taking N_{sat} into account

N_h^c	number of electrons from the atmospheric haze, not taking N_{sat} into account
$N_{ob}(f,\theta_R)$	number of CCD electrons from the image of the object, taking N_{sat} into account
$N_{ob}^c(f,\theta_R)$	number of CCD electrons from the image of the object, not taking N_{sat} into account
N_R	number of θ_R
N_{ro}	CCD readout noise
N_{sat}	saturation charge (electrons) of the CDD TDI lines
$N_{tot}(\theta_R)$	total number of noise electrons at the output of the CCD
n_φ	number of charge transfers per one CCD element
$P(u, v)$	aperture pupil function
$P_D, P_D(.)$	detection probability
$P_{\max}$	maximal probability of the correct decision
$P_{\min}$	minimal probability of the correct decision
$p(x_n, y_n)$	probability distribution function
$p(\Delta_n)$	probability distribution function
$p_n(u,v)$	pupil function of the *n*th subaperture
p_x	distance between the centers of CCD elements in the *x*-direction
p_{x1} and p_{x2}	lower and upper bounds of p_x

p_y	distance between the centers of CCD elements in the y-direction
p_{y1} and p_{y2}	lower and upper bounds of p_y
R	spatial resolution in the object plane
R_1 and R_2	lower and upper bounds of the radii of circular subapertures
R_{11} and R_{12}	lower and upper bounds of the inner radius of annular subapertures
R_{21} and R_{22}	lower and upper bounds of the outer radius of annular subapertures
R_A	radius of the aperture
R_E	Earth's radius
r_0	Fried parameter
r_{1n} and r_{2n}	inner and outer radii of the nth annular subaperture
r_n	radius of the nth circular subaperture
S_f	domain of the frequencies of interest
$S_{ph}(\lambda)$	spectral quantum efficiency of the photodetector
S_R	set of the spatial resolutions
$S_{tot}(f,\theta_R)$	total value of the signal expressed in electrons
$SNR(R,\theta_R)$	SNR at the output of the photodetector
$SNR_{\max}$	maximal SNR over Ω_R
$SNR_{\min}$	minimal SNR over Ω_R
SNR_P	perceived SNR

SNR_{Th}	threshold value of the SNR
s_{12}, s_{13}, s_{23}	distances between the centers of the corresponding subapertures: $1-2, 1-3, 2-3$
T_{el}	time of integration by one CCD element
$U(...)$	total field in the focal plane
$U_n(...)$	field in the focal plane from the nth subaperture
(u,v), (u',v')	pupil plane coordinates
(u_f, v_f)	pupil plane coordinates corresponding to $\vec{f}$
(u_n, v_n)	coordinates of the nth subaperture center
(u_n^0, v_n^0)	coordinates of the nth subaperture center in absence of the IA errors
V_0	wind velocity averaged over the altitude
$\vec{V}_{ch}$	average CCD charge packets motion velocity
$\vec{V}_{img}$	image motion velocity in the focal plane
$w_n(u,v)$	function of the wave aberration of the nth subaperture
x_e	x-coordinate of the CCD element center
x_n	x-component of the IA errors corresponding to the beam from the nth subaperture
$\bar{x}_n$	mathematical expectation of x_n
y_n	y-component of the IA errors corresponding to the beam from the nth subaperture

$\bar{y}_n$	mathematical expectation of y_n

Greek

α	parameter $\left(=\frac{k}{F}\right)$
$\alpha(\lambda)$	spectral absorption coefficient of the CCD material
α_V	parameter of synchronization of the velocities V_{img} and V_{ch}
β_V	angle between the vectors $\vec{V}_{img}$ and $\vec{V}_{ch}$
$\gamma(a,b)$	the incomplete gamma function
γ_n	angle of the random error beam tilt from the *n*th subaperture
Δ_n	piston error of the beam combiner for the beam from the *n*th subaperture
$\bar{\Delta}_n$	mathematical expectation of Δ_n
$\widetilde{\Delta}_n$, $\widetilde{\Delta}_n(x_n, y_n)$	phasing error of the beam from the *n*th subaperture
$\Delta\varphi_n(f_u)$	phase shift of the signal charge packet after *n* transfers
$\delta_n(x_n, y_n)$	phasing error dependent on x_n and y_n
ε	charge transfer inefficiency
η	parameter of the accuracy of the arctangent-approximation
η_n, $\eta_n(..)$	parameter of an accuracy of the *n*th subaperture arctangent-approximation
θ_R	angle of the direction of resolution

λ	wavelength of radiation
μ_P	value characterizing the perceived probability
$\rho_1(\lambda)$, $\rho_2(\lambda)$	reflection coefficients of the TO
$\rho_{bg}(\lambda)$	reflection coefficient of the background
$\rho_{ob}(\lambda)$	reflection coefficient of the object
$\rho_{x_n y_n}$	correlation coefficient between x_n and y_n
σ_P	rms deviation of the detection probability
σ_{x_n}	rms deviation of x_n
σ_{y_n}	rms deviation of y_n
σ_{Δ_n}	rms deviation of Δ_n
τ_0	wavefront coherence time
$\tau_A(\lambda)$	spectral transmittance coefficient of the atmosphere
τ_e	exposure time
$\tau_n(...)$, τ_n	transmittance coefficient of the *n*th subaperture
ϕ_n	phase of the wave incident on the *n*th subaperture
Ω'_{nk}	part of an intersection area of two subapertures
Ω_R	domain of θ_R on the earth surface

Chapter 1

Introduction

From the time of the first launches of space-based Optical Systems (OSs),[1] scientists and specialists of the world continually have been searching and considering various ways of increasing the angular and spatial resolution of such systems. Since the value of the resolution capability is proportional to the size of a receiving aperture of the OS, the obvious way of increasing the resolution of mirror and mirror-lens space-based OSs was increasing the diameter of the system head mirror. Unfortunately, technological problems of manufacturing and adjustment of a large-sized optics impose some restrictions on the maximal size of optical details and, therefore, such increasing the resolution could not occur indefinitely. Further, the increase in the diameter of the head mirror implies an increase in the weight and overall dimensions of the OS as a whole but its mass and size are limited by volume and mass constraints imposed by a launch vehicle, as well as by the scaling laws of manufacturing costs.[2,3] The slope of the telescope cost line follows a 2.7-power relationship for telescopes built in the first half of

the twentieth century, and about a 2.5-power in the second half as a result of considerable engineering innovations. Extrapolation of a telescope diameter up to 30 m indicates a cost of over $1 billion. Because of such a cost dependence of monolithic optics, efforts were taken to overcome the tendency of increasing the diameter of the monolithic head mirror. Further development of the space telescopes had been divided into some branches, among which the following technological trends can be named:

- lightweight optics
- deployable optics
- adaptive and active optics
- membrane mirrors and inflatables
- distributed optical arrays.

It is necessary to note two intensively developed technical directions: deployable segmented mirror telescopes and distributed aperture telescopes using interferometry.

The segmented systems form a continuous (to some degree) surface of the head mirror and continue development of the idea of increasing the diameter of the receiving aperture, not only on the earth but also in the space at telescope assemblage.

The distributed (or sparse, diluted) aperture telescopes have no single monolithic head mirror. The aperture of such systems is formed by several subapertures which either are fixed rigidly at the certain distances from each other and mounted, as a rule, on a single satellite, Figure 1.1a, or are dynamically independent and mounted on different satellites like micro-satellites, Figure 1.1b.

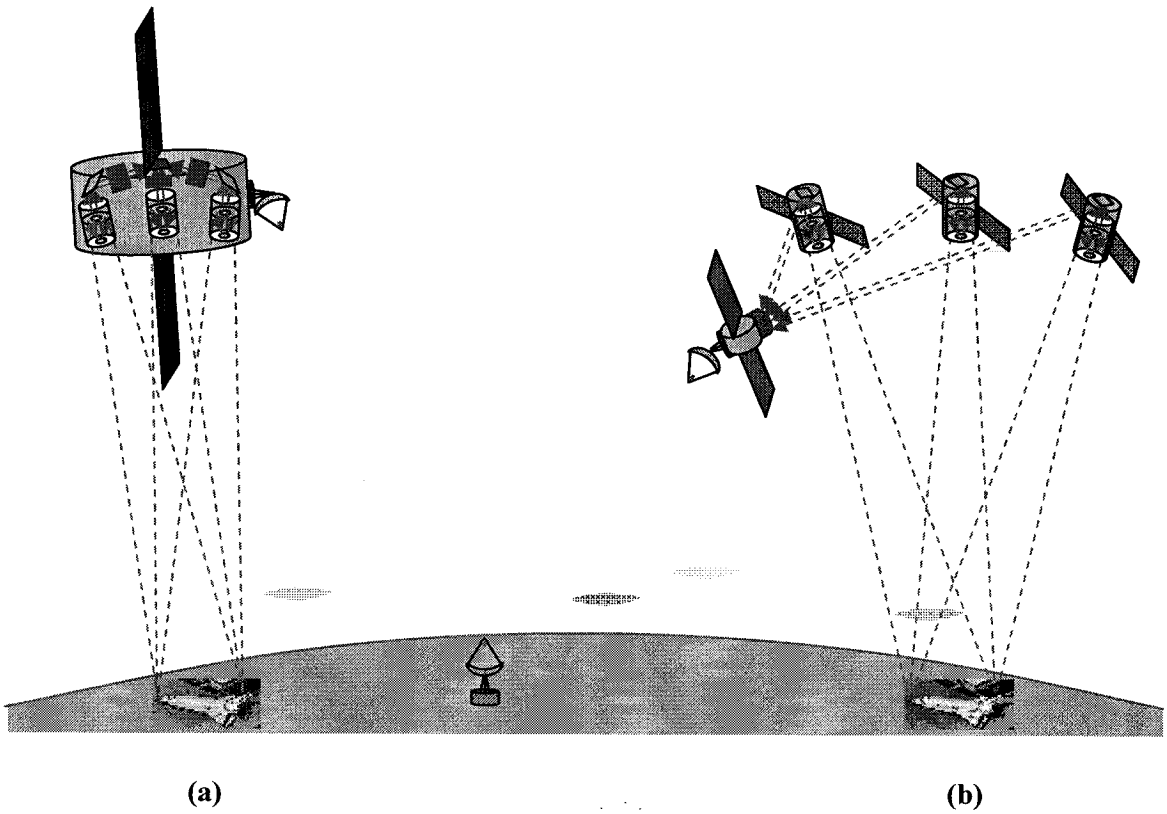

Figure 1.1. Subapertures: (a) fixed, (b) independent.

The image formation in the distributed aperture systems can be realized by both optical and electronic ways, at that, the optical way is typical for both the fixed and independent subapertures, while the electronic ways is more used for independent systems. In this thesis, we only consider a case of an optical image formation for which the fixation of subapertures or the independence of the satellites with telescopes does not matter, but only the optical path differences between beams do matter.

The development of sparse aperture telescopes is driven by a desire to achieve relatively high resolution with relatively small collecting area whose weight and size are

especially important in air- and space-borne systems. Viewing the tendencies of changing the conceptions in a telescope design from monolithic to distributed aperture constructions, some design constraints leading to a multiple telescope array are indicated in [4]. The origins of the sparse aperture imaging and its general principles of operation are discussed in the historic review,[5] tracing the history of sparse aperture imaging from early radio measurements to the current generation of optical interferometers. It is noted that the sparse aperture imaging has its roots in the work on optical interferometry by Fizeau and Michelson over one-hundred years ago, and the development of radio astronomy nearly fifty years later.

Since Labeyrie's first interferometric experiment with two independent telescopes,[6] several long-baseline optical interferometers have been built or are being planned. The samples of systems with fixed and dynamically independent subapertures, respectively, are the Space Interferometry Mission (SIM)[7] which is designed as a space-based 10-m baseline optical Michelson interferometer, and the Terrestrial Planet Finder (TPF)[8] whose baseline varies between 75 and 1000 meters. There are both advantages and disadvantages of these architectures. The main advantage of the fixed architecture is that the relative distances between the subapertures are fixed (in bounds of flexible boom vibrations), hence there is no need of a control system for controlling the relative positions of the satellites. The main disadvantage is small enough distances between the subapertures whose positions are defined by the length and construction of the booms and the launch vehicle fairing. At the same time, the absence of the fixation of the subapertures for the unfixed architecture is a disadvantage, since there is need of the

relative position control system. And it is a benefit, since the subapertures can be set to any optimal desirable relative positions.

The work on creation of the distributed aperture systems is planned to be continued in the future. Possible future instruments, ground or space-based, can be split into three main categories:[9,10] extremely large filled aperture telescopes, diluted interferometric arrays for direct imaging, and diluted interferometric arrays for aperture synthesis imaging. These concepts have been compared in terms of observing capabilities, performances and technological issues. As it is noted, these future instruments will be extremely complex and require strong R&D programs. The list of scientific criteria for comparing the main categories is also given, and the identified R&D priorities are emphasized.

In the context of the NASA's long-term programs for development of the earth observation systems in the 2010 – 2020th years, some advanced technologies for the earth science measurements are examined in [11], including sparse aperture collection systems and large array detectors to provide enhanced temporal and spatial resolution.

1.1. Optical-electronic systems

An Optical-Electronic System (OES) can be defined as a device with the help of which the information contained in a stream of radiation about size, form, position, spectral properties of an object, after transformation of radiation to an electric signal, is processed for the purpose of extracting it from noise for a subsequent registration. The

wide range of use of the modern OESs and tasks solved by them has led to the fact that now it is practically impossible to list all types of the systems manufactured serially or as separate unique samples. However, some general features of OESs are listed below.

1.1.1. Functioning of the OES

Generally, considering operation of an OES, it is necessary to take into account all the functional elements which can influence the quality of the final image: from a source of radiation up to an output device. The functional scheme of the OES – the basic functional element structure of the OES operation and the sequence of transformations – is shown on Figure 1.2 followed by some descriptions.

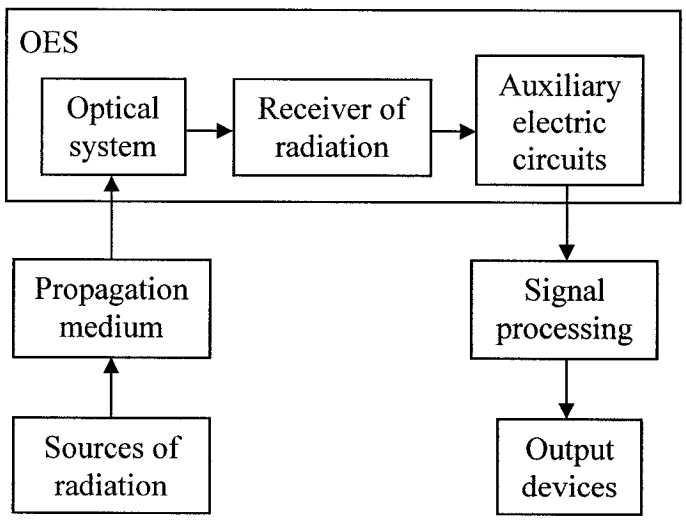

Figure 1.2. Functional scheme of the OES.

Sources of radiation

The sources of radiation can be physical processes or phenomena proceeding in the space of subjects, or external sources of both natural and artificial origin. In the presence of the external sources, the space of subjects can be considered as a radiator generating reflected or scattered radiation – a field of radiation whose characteristics change in space and time. Depending on the purposes of use of the system, some subjects are objects of observation, and some ones are components of a background. The presence of a varying background is the first cause making difficulties for observation. Another cause is chaotic fluctuations and noise. Despite amplifying small electric signals, practically it is impossible to distinguish weak signals due to these reasons.

Propagation medium

In our case, it is Earth's atmosphere through which the radiation passes from the space of subjects to a received part of the OES. The atmosphere absorbs (molecules of water, carbonic gas, ozone), scatters (molecules of atmospheric gases, particles of dust, droplets of water), and distorts (turbulence, heterogeneity of the refractive index) the passing optical signal.

Optical system

An OS is one of two basic parts (the other one is the photo-receiver of radiation) of the OES. It can consist of various types of details, such as protective glasses, blends,

aperture stops, mirrors, micro-optoelectromechanical systems (MOEMSs), lenses, prisms, filters, gratings, etc. It carries out functions of primary processing of the information in the optical range of spectrum according to the OES functionality. Such functions can be: an image formation, division of radiation by spectral structure and a polarization degree, splitting and changing the direction of a radiation stream, summation of streams of radiation, etc. In any case, the OS carries out two main functions. The first function is to collect a maximally great stream of coming radiation and, with minimal losses, to direct it on a following processing element. The second function is optical filtration of the incoming signal.

There are two main types of the optical filtering: spectral and spatial. The spectral filtering is realized with the help of optical filters (absorbing, dispersive, reflecting, interference) to limit the radiation incident on the receiver by fixed wavelength intervals. The spatial filtering is realized with the help of different spatial filters such as aperture stops, slits, and rasters. The focusing property of an OS can be considered as the aperture spatial filtration of the formed image.

The additional functions of the OS can be: providing the necessary field of view, providing the process of target tracking, modulation of a constant component of radiation, protection of an internal part of the device against harmful influences of environment, etc. During passage of a radiation flux through an OS, there are unavoidably energy losses in cowlings, mirrors, lenses, spatial and spectral filters. These losses are caused by absorption of the energy in optical materials, partial reflection from lenses, incomplete reflection from mirrors, vignetting, and other causes. The internal structure and

aberrational properties of a concrete focusing OS are subjects for consideration by the computational optics, and are not considered here.

The image formation with a sparse aperture system occurs due to imposing the light beams from the subapertures, hence it is possible to talk about the interference of these beams in a common focal plane. Generally, interferometers for imaging can be divided, depending on a combining method, into two types: a pupil-plane combination type (for example, the Michelson interferometer, Figure 1.3), and an image-plane combination type (for example, the Fizeau interferometer, Figure 1.4).

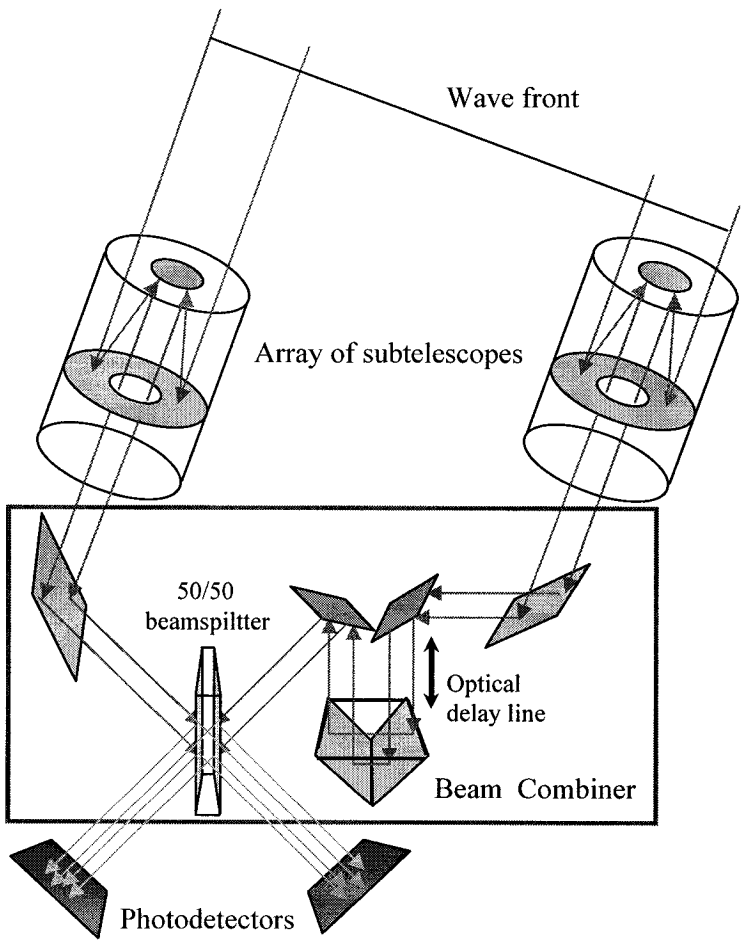

Figure 1.3. Michelson-type interferometer.

The Michelson interferometer generally consists of an array of spatially separated segments, the beams of which are usually reduced in size and then mixed together on a 50/50 (for two beams) beamsplitter. It gives interfered fringes (the inverse Fourier transform is needed for image restoration of objects), and a narrow field of view. It is suitable for astronomical targets – unchanged over a long period of time.

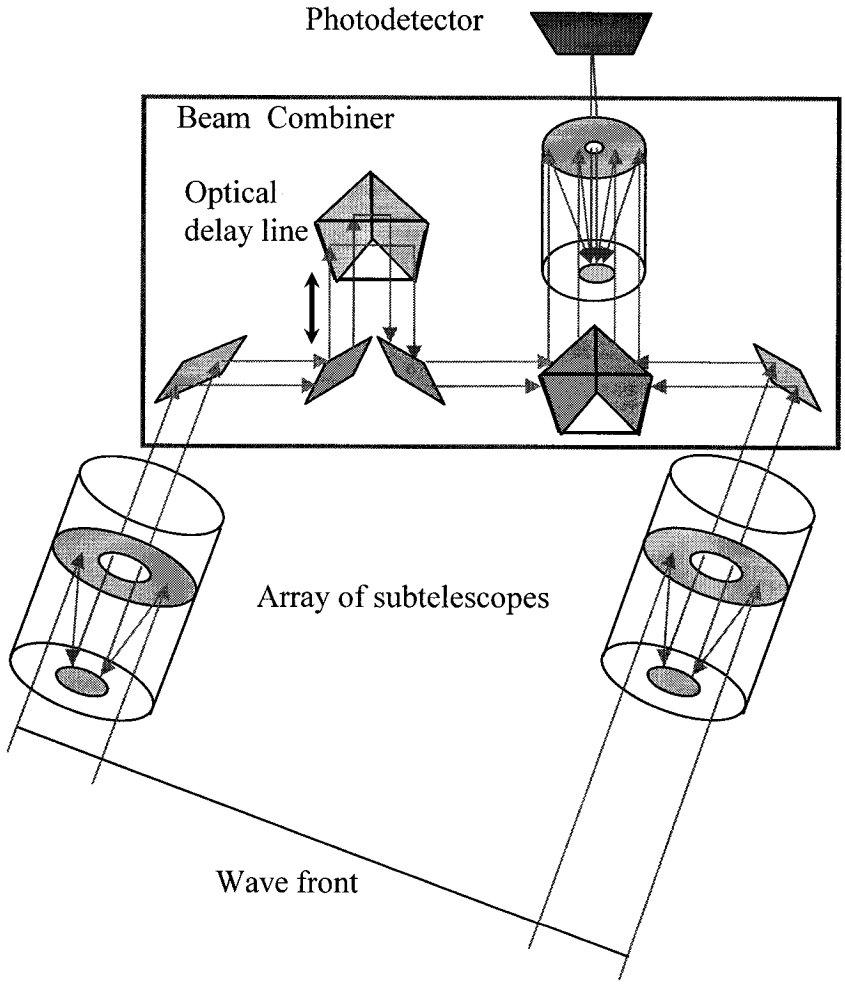

Figure 1.4. Fizeau-type interferometer.

The Fizeau interferometer consisting of an array of spatially separated segments has a common focus. It gives a direct image of objects and a wide field of view. It is suitable for the wide angle astrometry, remote sensing, and for rapidly changing targets (Terrestrial, Earth objects). Besides, the Fizeau approach can possibly utilize[12] a larger number of simpler and less expensive spherical mirrors distributed on a spherical surface.

For separated telescopes, the "golden rule"[13] was formulated: "beams from separated telescopes must be recombined so that they appear to be coming directly from a single large telescope which has been masked so as to reproduce exactly the ensemble of collecting telescopes". Only ten years later, it appeared that this rule can be evaded,[14] with considerable benefit for future applications. It was shown that a "densified" pupil can provide direct images in a non-Fizeau mode if the subpupil centers are preserved in terms of their relative locations. It is asserted[15] that a densified-pupil or "hypertelescope" imaging mode can concentrate most light into a high-resolution Airy peak.

Pros and cons of Michelson and Fizeau type interferometer configurations are compared[16] for systems in space having baselines in the 5 to 100 meter range. Depending on the baseline, two preferable configuration types are defined: for baselines less than 10 meters, a Fizeau type is preferable; for baselines greater than 10 meters, a Michelson type is preferable; since, although the size of the coherent field-of-view is larger in a Fizeau type interferometer, the tolerances required by wide field operation are easier to achieve in the Michelson type.

For our consideration, we have chosen the Fizeau-type interferometer consisting of an array of spatially separated segments, and having a common focal plane.

Receiver of radiation

The receiver of radiation is the second (after the OS) basic element of the OES on a way of the signal propagation. In essence, the name "*optical-electronic*" is obliged to the property of a system, in particular, receiver to transform an optical radiation stream to an electric signal. Receivers can be classified by various attributes among which it is necessary to note the classification by the energy form to which the receiver transforms radiation incident on it. In this connection, we are interested in a photo-electric or photon receiver of radiation.

In the photo-electric (photon) receivers, the energy of radiation is transformed to the mechanical energy of electrons of the irradiated substance. These receivers are distinguished in accordance with the external photo-effect (vacuum and gas-filled photo-elements, photo-multipliers), and with the internal photo-effect (photo-resistors, photodiodes, galvanic elements, charge-coupled devices (CCDs)).

Type of the used photodetector. At the observation of the earth surface with the help of the space-based OES not using motion compensation elements, the formed image continuously moves in the focal plane of the OS. Since the sensitive plane of the photodetector is coincided with the focal plane, the image continuously moves on the surface of the photodetector. Such movement determines the type of photodetector which should be used in the system.

For example, with a film as the sensitive element, it would be possible to use a shutter device similar to one used in usual cameras much greater in size. However, when the image is moving fast, to avoid appreciable dither of the image on the film, a high

speed mechanical shutter is necessary which, together with a discrete motion of the film, creates additional sources of vibrations in the system, thus increasing the dither of the image. Another way of using a film is forcing it to move together with the image at the same direction. For this purpose, it is necessary to use complex mechanical devices of a high accuracy to match the speed of the film motion with the one of the image motion, keeping the film surface in the focal plane – that creates additional problems of the control in operation.

In such a situation, the application of non-mechanical photodetecting devices such as CCDs seems obvious. Using a one-dimensional (linear array) CCD, the motion of the object image relative to the photodetector is used for creating a one-dimensional field of the image. Such a method of observation called the "pushbroom" mode, creates an observation object image consisting of strips. The schematic diagram of the CCD operation in the "pushbroom" mode is shown on Figure 1.5.

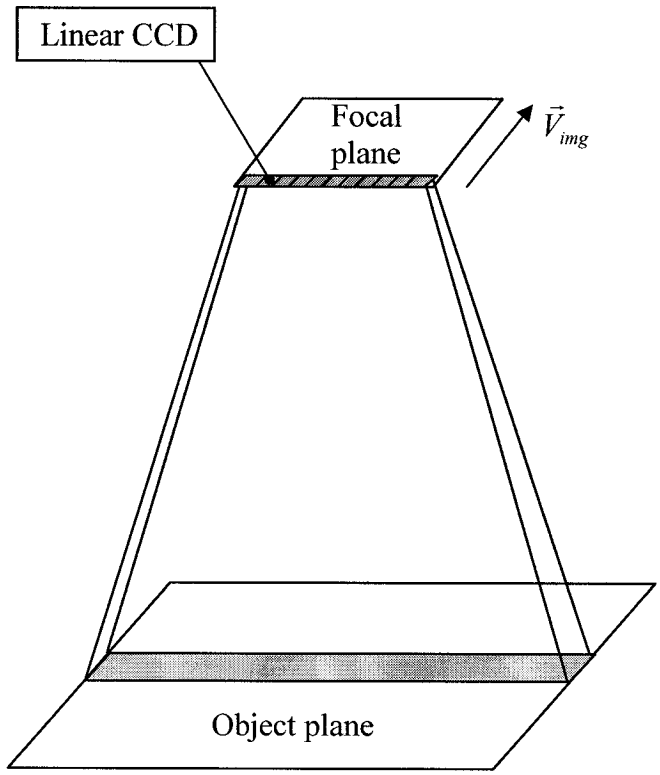

Figure 1.5. Schematic diagram of the linear CCD operating in the "pushbroom" mode (the OS is not shown).

Now let us imagine, that some number (M-1) of the other linear array CCDs are mounted in parallel to the first one, and the charge packets from each element of each linear CCD move to the corresponding element of another at an average speed $\vec{V}_{ch}$ equal to the speed of the image motion $\vec{V}_{img}$. We have used such a CCD operating in the so-called mode of *Time Delay and Integration* (TDI). This TDI-CCD is schematically shown on Figure 1.6. The full output signal will be by M times larger than the signal received from only one-line array. This method allows increasing the sensitivity of photodetecting and, consequently, the sensitivity of the system as a whole.

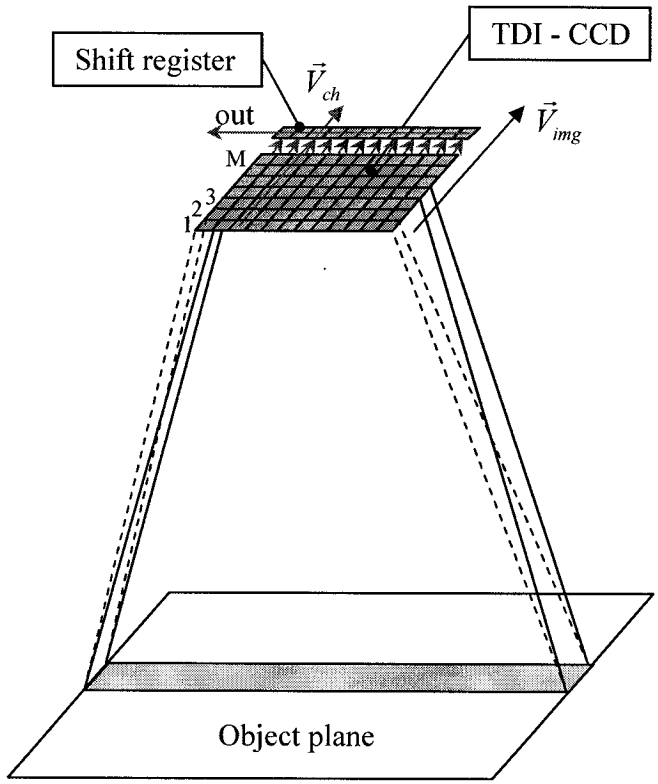

Figure 1.6. Schematic diagram of operating the CCD in the TDI mode (the OS is not shown).

Auxiliary electric circuits

The electric signal produced by a receiver is usually small. To take the useful information from it, the signal must be amplified. Important parameters concerning amplifiers are: coefficient of amplification, dynamic range, pass band, and level of noise. Besides, the form of frequency and phase characteristics, total dimensions, weight, power consumption are sometimes stipulated. Usually an amplifier is structurally divided in two parts, one part (preamplifier) is mounted in immediate proximity from the radiation

receiver and serves for preliminary amplification of the signal up to a level sufficient for subsequent transferring with a long cable surrounded by electric and magnetic fields. Another part (the main amplifier) contains necessary elements of adjustment of amplification, pass bands, and other parameters.

Signal processing

The output signal from the auxiliary electric circuits contains both the helpful information (a signal) and noise. For the extraction and processing of the useful signal from a mix of the signal and noise, different linear and nonlinear elements which carry out the necessary logic operations follow the electric circuits. In the elementary case, the operation of the signal extraction consists in the frequency analysis of the mix of the signal and noise with the help of narrow-band electric filters, and the operation of the signal processing – in the signal detection. However, more complex algorithmic solutions are usually required. Besides, the tasks of automatic detection and classification, decoding, special tasks of the system destination can be resolved at this stage with the use of computer environment.

Output devices

Various devices of the image visualization and the information storage are used for registration of the processed signals; for example, photographic, television, automatic systems. The type and function of the registration device is determined by the OES functionality.

1.1.2. Types of the OESs

Depending on the functionality, any OES can be related to one of the main following types:

- *measuring*
- *tracking*
- *informational*

Measuring OESs

The measuring OESs are destined for measurement of some characteristics and parameters of radiating objects: the distance, sizes, coordinates and motion speed with respect to some coordinate system, an energy density, a spectral structure and polarization degree of radiation, mutual orientation of objects, etc. The information can be displayed or transformed into a signal for the control of object motion, physical and technological processes. The basic requirement for the measuring OESs is the maximal accuracy of measuring the corresponding parameters.

Tracking OESs

The tracking OESs are destined for automatic tracking some radiating objects or maintaining the radiation parameters at defined levels. Their prominent features are measurement of radiation parameters using compensation schemes, the presence of negative feedback from an output of the system to its input, and the presence of executive

devices eliminating the mismatches between input and output magnitudes of the controlled values or processes. Typical samples of such OESs are devices of tracking the isolated small-sized sources of radiation (for example, thermal and laser homing missiles), devices for automatic joining of mobile objects, devices for part cutting in accordance with design drawings, systems for maintenance of the regime of technological processes on basis of integral and spectral transmittance coefficients, and other devices operating on basis of compensating schemes. The basic requirement to the tracking OESs is the maximal accuracy of object tracking or maintaining the defined levels of controlled processes.

Informational OESs

The informational OESs are destined for gathering, processing, recording the information about the microstructure of brightness fields of radiation in various spectrum intervals. Typical samples of such systems are cameras for photography of thermal fields of region maps, television systems, devices for controlling electro-circuits in accordance with their thermal relief in working state, devices for medical diagnostics by a temperature skin relief, laser locators, devices for recognition of objects and images, etc. These OESs should transform maximally comprehensively and accurately all the details of radiating objects and surrounding background in a predefined spectrum interval of radiation to an electric signal. Then, on basis of it, the visible spectrum image can be restored, or the research of characteristics of the microstructure of the radiation field of the objects and background can be made.

1.1.3. Main characteristics of the OESs

The quantitative estimation of properties and efficiency of various OESs can be given with the help of some main characteristics. Depending on the practical destination and use of the system, some characteristics can be more important, others – less important, but almost always the significant parameters are: threshold of sensitivity, field of overview, time of overview, field of view, *resolution capability*, accuracy. There are some more various characteristics of the OES operation but they are either derivatives from the just listed ones, or are used in certain very specialized systems. For the space based OESs, *the spatial resolution* in the plane of observation objects is usually used.

Resolution capability

The resolution has always been, and still is, an important notion. It is interpreted in many ways. The resolution capability is usually characterized by the least angle between two point sources of radiation which can be detected by the system as separated. It can be also expressed by a number of lines per angle unit or per all the field of overview which can be distinguished on an output device. Past and present approaches to the concept of optical resolution are reviewed and discussed in [17].

Spatial resolution

The spatial resolution is a value deduced from the *resolution capability* and unambiguously connected with it through the distance of observation. We use this

characteristic as the key parameter describing the quality of the space-based OES operation.

1.2. Problem statement

In accordance with the Merriam-Webster Online Dictionary,[18] optimization is "an act, process, or methodology of making something (as a design, system, or decision) as fully perfect, functional, or effective as possible; *specifically* : the mathematical procedures (as finding the maximum of a function) involved in this". Optimization of the OES's design parameters is a complex industrial process carried out at a design stage by teamwork of system managers, designers, technologists, engineers, etc. It is impossible to consider all aspects of optimization of the OES within the bounds of a single thesis. We consider the optimization only from the point of view of calculation of some design and operating parameters, namely, a distributed aperture configuration, an effective focal length, geometrical size of a CCD pixel, and a number of TDI lines.

1.2.1. Optimization of the distributed optical aperture configuration

The parameters of the aperture configuration affect essentially[19] the diffraction-limited imaging characteristics of a phased telescope array. The characteristics of image formed by a sparse aperture depend substantially on the dilution aperture ratio. For direct-

imaging phased telescope arrays, when it is necessary to have fine details of observed objects, the aperture configuration must not be so dilute that to produce substantial areas of zero modulation within the cutoff frequency of the Modulation Transfer Function (MTF)[20] which depends on a large number of factors, including the aperture configuration.[21–23] Investigating the effects of dilution on a six-element synthetic aperture of a type proposed by Meinel,[24] it is shown[25] that small degrees of dilution result in a significant gain over the performance of a single element, whereas more dilute apertures are inferior for direct imagery.

The images can contain artifacts and spurious images that are undesirable. The results of imaging show[26] that the severity of the multiple ghost images[27] increases with decreasing the dilution ratio. In this situation, multiple ghost images produced by the given feature could easily be mistaken for actual features in the object. A comparison of the diffraction images corresponding to the MTFs of different arrays indicates that the ghost images vanish if the array is optimized to produce the MTF exhibiting uniform spatial frequency response.[26,28] Hence, the uniformity of the MTF (Figure 1.7) representing a subaperture array is highly desirable to achieve the good image quality.

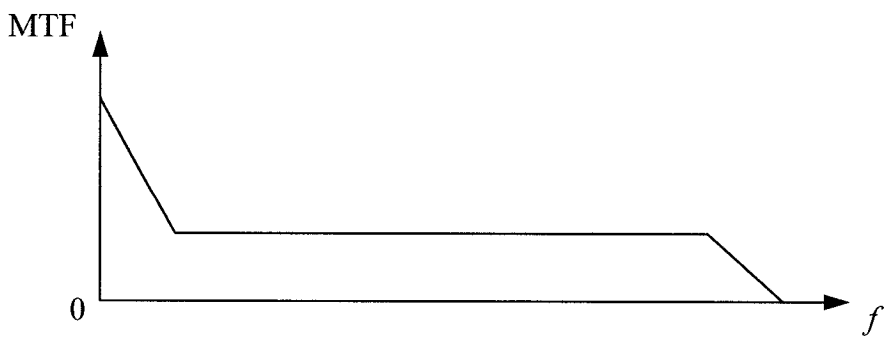

Figure 1.7. Uniform spatial frequency response.

The MTF should be smooth continuous function with no ups and downs and should have nearly the same function values for all azimuth orientations.[29] Removing artifacts can be done in some cases by special algorithms,[30] using multiple narrow bandwidths and the fact that the Signal-to-Noise Ratio (SNR) can be improved by filling different portions of the MTF with different wavelengths.

For a fixed amount of optical surface, the image quality improves with decreasing a fill fraction due to an increase in resolution.[31] At the same time, sparse apertures can make large-diameter telescopes affordable but at expense of increased integration time. For example, to achieve a given image quality, the integration time for a fixed sparse aperture goes as the inverse square-, cube-, or fourth-power[32] of the fill factor, depending on a noise identity; and square or cube[33] of the fill factor, depending on a sparse aperture design. This dependence has been examined[34] for monochromatic imaging. The performed numerical experiments investigating the relationship between the fill factor and exposure time have indicated that the cubic relationship holds only if the aperture is scaled properly as the fill factor decreases. It is shown that the relationship between the integration time and fill factor is more complicated than a simple power law if the scaling of the aperture configuration with fill fraction is not done properly.

Increasing the imaging time can be accomplished by placing the satellite in a higher orbit, but it reduces the resolution of the systems because of the greater distance between the satellite and a target. Reducing the fill factor decreases the weight, but also reduces the optical MTF and the system SNR. The image simulations for different sparse aperture systems show[35] that the image quality varies dramatically for the different apertures as

the fill factor decreases. A psychophysical evaluation was also conducted[36] to determine the integration time necessary to maintain the image quality as the fill factor decreases.

Objective functions

One of the first tasks in the formulation of an optimization problem is to determine an optimized objective function. At the separate optimization of the optical part, the objective function can be determined, for example, in the imaging (focal) or pupil (aperture) plane. The imaging plane is a one of interest of the Point Spread Function (PSF), while the aperture plane is used for tasks taking into account the Optical Transfer Function (OTF) and/or the MTF. Various approaches have been taken in literature to choose the objective function for optimization of the aperture configuration. Some authors use the criteria based on the shape of the PSF such as the encircled energy or the sidelobe levels.[37-39] Others use criteria based on properties and behavior of the MTF,[22,27,40-43] minimal spatial frequency redundancy,[27] the phase,[44] and the error of restoration of the original object from the recorded image.[45] From the point of view of the resulting PSF and MTF, the merits of different types of aperture configurations are discussed in [46], including the minimally redundant Golay type configurations[47] having the property of maximizing frequency-plane coverage for a given number of circular subapertures. Often different SNR criteria are used.[32,34,48,49] Researching the redundant and nonredundant beam recombination, it is shown[48] that nonredundant beam recombination is the optimal strategy for object reconstruction when the SNR exceeds some level that is a decreasing function of the input pupil redundancy. When the SNR is too small for this condition to be met, redundant beam recombination is preferred. The

maximum entropy method is also applied to efficiently incorporate very high spatial frequency information with "low-resolution" data.[50] The overview[51] gives some ideas about complex optical and image processing techniques required for the modern systems such as deployable segmented aperture systems, sparse aperture systems, interferometric imaging system, computational deconvolution and super-resolution techniques.

Computation methods

The computation methods used for the sparse array optimization are mainly, so-called, direct-search. The direct-search methods are used[52] when the derivatives of the objective function or constraints are not continuous, or their computation is difficult enough, and also when they are equal to zero within some area of arguments. Usually, these methods give a good solution but not optimal. Besides, the criteria of termination tests are not clear and are based on the current calculation results.

Other methods which might be used for optimization are the well known gradient optimization methods[53] based on the use of gradients of the objective function and constrained equalities and inequalities, and having a higher rate of convergence and clear criteria of the termination tests. Thus, the gradient methods seem more attractive if deducing of the analytical expressions for the derivatives is not very complicated. But there is a feature of the OSs with the sparse aperture which forces to use the direct-search methods for objective functions defined on basis of the OTF or MTF. It consists of a possible existence of zero-value areas of the OTF. In this case, the gradient of the minimized function can also contain zero-value areas. Such a situation can result in suspension of the calculation process if an intermediate solution falls into such an area. It

is one of the main difficulties when one wants to use the gradient method for sparse aperture optimization. In this case, the problem of optimization can be solved only for some aperture configurations and some initial conditions of the iterative process, which limits types of current tasks and complicates a solution process.

1.2.2. Influence of residual errors of a beam combination system

The OSs with a distributed aperture have a number of essential differences from ones with a monolithic aperture. For systems forming a united image in a common focal plane, the main difference is a presence of a beam combination system joining together the beams from the subapertures. It is well understood[54] that one of the major challenges in implementing a sparse aperture imaging system is the need to maintain a constant phase relationship among the segments of the wavefront from the subapertures for all relevant field locations. Some physical models of the phase control of different phased errors and results of computer simulation of the beams control via the fast Fourier transform computational methods in synthetic aperture systems are presented in [55].

The problem of combining the beams is regarded[56] as the most challenging aspect of the sparse optical arrays. Complexity of the problem is confirmed indirectly by the fact[57] that, having experimented designing the beam combiner with a variety of optical software tools such as ZEMAX (Focus Software), Optima (Lockheed Martin) and ASAP (Breault Research), it was found no one tool capable of satisfying all design requirements. It is noted[9] that the combiners need particular R&D. They have to integrate several functionalities, among them: pupil stabilization, field rotation compensation,

residual piston correction, internal alignment and metrology tools. Multi-stage combiners can be also considered depending on the interferometer design. It is obvious that the optical control system for the beam combination is necessary to compensate diverse errors in real dynamical operations.

The dependence of the spectral irradiance distribution of a diffraction-limited, properly phased, aligned, and focused sparse aperture telescope consisting of N circular subapertures is well known[58] as well as an analytic expression for the OTF.[59] But it is obvious that the process of the beam combination is not deterministic, and it depends on various random factors. First of all, such factors are random errors of dynamic positioning of movable optical elements of the beam combiner – the result of the limited accuracy of its control system. In this case, the telescope becomes not properly phased and aligned, and the residual random errors such as the Image Alignment (IA) and Optical Path Difference (OPD) errors should be taken into account.

Different investigations are carried out in this direction. Researchers present the basic diagrams of the combined image formation,[60,61] technical characteristics[61] and specificities[62,63] of the beam combiners. Various estimations are applied[56,57,61,64,65] to determine the influence of the beam combination errors on the quality of the formed image, including the OTF,[66] aperture redundancy and dilution,[67] and the standard technique of expansion of the wave-front aberration function in a series.[60]

The tilt errors of the wave fronts of the beams from an array of afocal telescopes limit the achievable field of view. It has been shown[68] that adjusting the optical delay lines permits sharp imaging to be obtained at off-axis angles, but the size of the field of view decreases as the off-axis angle increases. Parametric studies and sensitivity analyses

were performed[60] for a variety of subaperture configurations and telescope design parameters to determine the variety of the off-axis performance of a phased telescope array subject to size of the telescopes.

The computation of the sparse aperture array OTF depending on random phase errors are calculated both numerically,[69] in particular, by Monte-Carlo numerical simulations, and analytically,[70] including the calculation of the Strehl ratio. There is also an analytical accounting of the influence of the static phasing errors on the irradiance distribution in a focal plane.[71] But it does not give the analytical concept of what quality of the image will ensue as a result of the dynamic process of the image formation, especially for the systems with a dynamic aperture reconfiguration during an active process of observation.

1.3. Goal of the thesis

1.3.1. Motivation

The adduced review of the selected literature shows permanent interest of scientists in diverse problems of research of the OSs with a distributed aperture. We see that a lot of aspects have been studied and developed. Meanwhile, there are some problems that were not covered in literature:

1. The use of the gradient optimization methods for optimization of the sparse aperture configuration.

2. The analytical description of the influence of the IA and OPD errors of a beam combination system on the average OTF expressed in terms of statistical parameters of the function of the error probability distribution.

1.3.2. Solution principles

1. To have a possibility of using a gradient method for the optimization of the distributed aperture configuration with the MTF-based objective function, we need to have this function with no zero-value regions. At the same time, the MTF of the distributed OS can have such regions. To overcome this difficulty, we redefine the subaperture step pupil functions by functions that continuously differentiable and have no zero-value regions. In particular, we use approximation. Some results of using of the subaperture step pupil function approximation by an arctangent are presented in our paper.[72] This approach can be used for both the Michelson- and Fizeau-type interferometers for multi-aperture optical telescopes, and for both space and earth sciences missions.

2. The presence of a beam combination system which forms a united image in a common focal plane is one of the features of the optical sparse array system operating as the Fizeau-type interferometer. Any control system of a beam combiner has a limited accuracy and, as a result, introduces some optical errors influencing the quality of the united image. It is especially concerned to the systems with a dynamic aperture reconfiguration during an active process of observation. The analytical expressions deduced in a general form for the spectral Instantaneous OTF (IOTF) of the optical sparse

array consisting of N circular and annular subapertures, depending on the residual random IA and OPD errors, and the spectral Average OTF (AOTF) for the Gaussian probability distributions depending on the statistical parameters of the last are presented in our paper.[73] The formulas are deduced on basis of the Fraunhofer approach to the Kirchhoff diffraction theory. The results can be used for both space and earth sciences missions.

1.3.3. Application of the solutions

Optimization of design parameters of the space-based OES is a complex computation procedure including the consideration of influence of all components of the system on the resulting values of interest. Considering the OES optimization from the point of view of calculation of design parameters, it is necessary to take a lot of specific characteristics into account. Among them the characteristics of: assumed observation objects and spreading backgrounds, conditions of object and background illumination, the atmosphere, the orbital parameters and dynamics of carrying satellites, the OES, communication, and types of final information.

Depending on the criteria of operation quality, imposed constraints, as well as the purposes of use of both single parts of the OES and the OES as a whole, it is possible to consider optimization of only one part of the system or optimization of two or more parts simultaneously. An example of the first optimization is optimization of the receiving OS aperture configuration to maximize the optical MTF on predetermined intervals of spatial frequencies in the focal plane. An example of the second optimization is optimization of

the OS and photodetector to maximize the earth surface spatial resolution which is one of the very important operation parameters of the OES used for the earth surface observation.

In this connection, the first two parts presented in this work related to the separated optimization of the aperture configuration are:

1) Optimization of a distributed optical aperture configuration, which is shown in Chapter 2;
2) Influence of residual errors of a beam combination system on the OTF, which is shown in Chapter 3.

Considering the optimization of the OES on basis of more general SNR criteria, we should use the design parameters of both the OS and the Image Sensing System (ISS). If parameters of the ISS are constant, we have a separate optimization of the OS only. If parameters of the OS are constant, but the parameters of the ISS vary, we have a separate optimization of the ISS only. Finally, considering the optimization of the OS and the ISS simultaneously, we have a joint optimization of the OS and ISS. All these tasks are covered in Chapter 4 which is the third part of this thesis:

3) Optimization of the OES:
   - optimization of the OS: the aperture configuration and the effective focal length;
   - optimization of the CCD: the pixel sizes and the number of TDI lines;
   - joint optimization of the OS and the CCD.

The results of the first two parts are presented in our first and second papers[72,73] correspondingly. The contents of the third part are reflected in our third paper.[74]

1.3.4. Objective

This thesis is an attempt to show a possibility of using the gradient optimization methods for the optimization of the space-based OESs with distributed apertures, and to show the description of the influence of the IA and OPD errors of a beam combination system on the AOTF expressed in terms of the statistical parameters of the function of the error probability distribution. Such an approach gives an opportunity to use existent methods of calculation and optimization of the OESs with a monolithic aperture to the OESs with a distributed aperture. We hope that this research will help to calculate the OESs with the optimal parameters of the optical and electronic subsystems, and to produce the necessary requirements to the accuracy of the beam combination control system, and to the CCD characteristics in a stage of the engineering design of the OES on basis of the MTF or SNR criteria which are directly connected with the spatial resolution of the system. It is the goal of this thesis and it is expected that the results of this work will be a base to investigate the more complicated systems of several micro-satellites whose relative positions are continuously changing in space.

Chapter 2

Optimization of a distributed optical aperture configuration

2.1. Approximation of the step pupil function

For our consideration, it is convenient to use the pupil function,[75] $p_n(u,v)$ of the nth subaperture in the following form:

$$p_n(u-u_n, v-v_n) = \begin{cases} [\tau_n(u-u_n, v-v_n)]^{1/2} \exp[-ikw_n(u-u_n, v-v_n)], & (u,v) \in A_n \\ 0, & (u,v) \notin A_n \end{cases}, \quad (2.1)$$

where:

u, v are pupil plane coordinates

u_n, v_n are coordinates of the subaperture center

$\tau_n(u-u_n, v-v_n)$ is a transmittance coefficient

k is a wave vector $(= 2\pi/\lambda)$

λ is a wavelength of radiation

$w_n(u-u_n, v-v_n)$ is a function of the wave aberration

A_n is an area of the subaperture.

We see that it is a step-type function. Considering the diffraction-limited OS $(w_n(u-u_n, v-v_n) \equiv 0)$ with a unit transmittance coefficient $(\tau_n(u-u_n, v-v_n) \equiv 1)$, the pupil function is

$$p_n(u-u_n, v-v_n) = \begin{cases} 1, & (u,v) \in A_n \\ 0, & (u,v) \notin A_n \end{cases}. \tag{2.2}$$

As an approximation of this function, it is possible to use the arctangent function in the form of

$$\arctan[\eta \cdot (x-a)], \tag{2.3}$$

where: $\eta \neq 0$ is a parameter defining the accuracy of approximation, a is some number. Figure 2.1 shows the comparative graphic for $\eta = 1$ and $\eta = 10$, and $a = 4$.

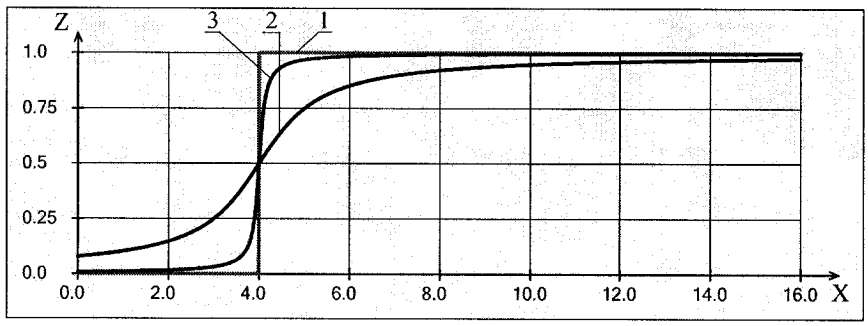

Figure 2.1. Comparative graphic: approximation of the step function:

1 : the step function; 2 : $0.5 + \frac{1}{\pi}\arctan[1 \cdot (x-4)]\}$;

3 : $0.5 + \frac{1}{\pi}\arctan[10 \cdot (x-4)]\}$.

To illustrate the approximation approach to optimization of the optical sparse array configuration, we used the arctangent function in the form of

$$\arctan\{\eta \cdot [(u-u_n)^2 + (v-v_n)^2 - r_n^2]\}, \tag{2.4}$$

where r_n is a subaperture radius. Then the approximation of the step pupil function can be written in the following forms which we use in our consideration:

for a circular subaperture:

$$p_n(u-u_n, v-v_n) = 0.5 - \frac{1}{\pi}\arctan\{\eta \cdot [(u-u_n)^2 + (v-v_n)^2 - r_n^2]\}, \tag{2.5}$$

and for an annular subaperture:

$$p_n(u-u_n, v-v_n) =$$

$$= \frac{1}{\pi}\{\arctan[\eta \cdot ((u-u_n)^2 + (v-v_n)^2 - r_{1n}^2)] - \arctan[\eta \cdot ((u-u_n)^2 + (v-v_n)^2 - r_{2n}^2)]\}, \tag{2.6}$$

where r_{1n} and r_{2n} are the inner and outer radii of the nth subaperture. Figure 2.2 shows the comparative graphic of a center section of the circular subaperture approximation at $\sqrt{u_n^{\,2} + v_n^{\,2}} = 6$ and $r_n = 2$; $l \equiv \sqrt{u^{\,2} + v^{\,2}}$.

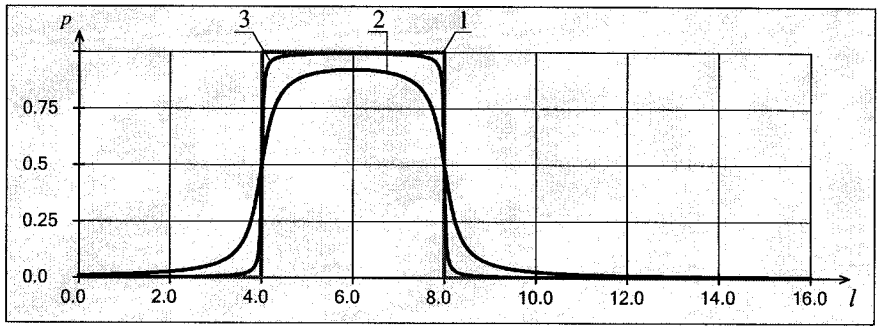

Figure 2.2. Comparative graphic: approximation of the step pupil function of the circular subaperture:

1: the ideal pupil function; 2: $0.5-\frac{1}{\pi}\arctan\{1\cdot[(l-6)^2-2^2]\}$;

3: $0.5-\frac{1}{\pi}\arctan\{10\cdot[(l-6)^2-2^2]\}$.

Figure 2.3 shows the similar graphic for the annular subaperture at $\sqrt{u_n^{\,2}+v_n^{\,2}}=6$, $r_{1n}=1$, and $r_{2n}=4$.

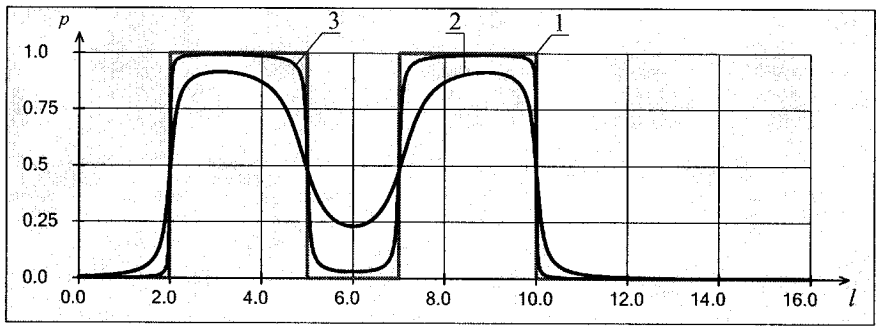

Figure 2.3. Comparative graphic: approximation of the step pupil function of the annular subaperture:

1: the ideal pupil function; 2: $\frac{1}{\pi}\{\arctan[1\cdot((l-6)^2-1^2)]-\arctan[1\cdot((l-6)^2-4^2)]\}$;

3: $\frac{1}{\pi}\{\arctan[10\cdot((l-6)^2-1^2)]-\arctan[10\cdot((l-6)^2-4^2)]\}$.

It is easy to see that the expression (2.5) gives

$$\lim_{\eta\to+\infty} p_n(u-u_n, v-v_n) = \begin{cases} 1, & (u-u_n)^2 + (v-v_n)^2 < r_n^2 \\ 0, & (u-u_n)^2 + (v-v_n)^2 > r_n^2 \end{cases}, \tag{2.7}$$

and the (2.6) gives

$$\lim_{\eta\to+\infty} p_n(u-u_n, v-v_n) = \begin{cases} 0, & (u-u_n)^2 + (v-v_n)^2 < r_{1n}^2 \\ 1, & r_{1n}^2 < (u-u_n)^2 + (v-v_n)^2 < r_{2n}^2 \\ 0, & (u-u_n)^2 + (v-v_n)^2 > r_{2n}^2 \end{cases}, \tag{2.8}$$

which correspond to (2.2). More generally, it is possible to use the approximating arctangent function in the form of

$$\arctan\left\{\eta_n \cdot \left[h\left((u-u_n)^2 + (v-v_n)^2\right) - h\left(r_n^2\right)\right]\right\}, \tag{2.9}$$

where: $\eta_n \equiv \eta_n\left(J(S_f), \nabla J(S_f)\right)$ is the subaperture approximation parameter depending on the objective function $J(S_f)$ and its gradient at the current iteration, S_f is a domain of the frequencies of interest $\vec{f}$; $h(.)$ is a continuous strictly monotone function, for example, the square root $\sqrt{x}$ or the logarithm $\log x$. It must be increasing for $\eta_n > 0$, and decreasing for $\eta_n < 0$. Other approximation functions can be also used as the bounded function such as the error function erf(x), and so on.

2.2. Definition of the problem

Let us use the objective function $J(S_f)$ as an integral square measure of deviations of the MTF $MTF_{OS}(f_u, f_v)$ of the OS from the desirable MTF $mtf_{des}(f_u, f_v)$ within some domain of the frequencies of interest S_f:

$$J(S_f) = \iint_{S_f} [MTF_{OS}(f_u, f_v) - mtf_{des}(f_u, f_v)]^2 df_u df_v, \tag{2.10}$$

where f_u, f_v are spatial frequency components.

It is well known[76] that for incoherent imaging systems, the OTF is given by the normalized autocorrelation of the complex pupil function $P(u,v)$:

$$OTF(f_u, f_v) = \frac{\int_{-\infty}^{+\infty} \int P(u,v) P^*(u - u_f, v - v_f) du dv}{\int_{-\infty}^{+\infty} \int |P(u,v)|^2 du dv}, \tag{2.11}$$

where:

$$u_f = \lambda F f_u, \qquad v_f = \lambda F f_v, \tag{2.12}$$

F is an effective focal length of the system.

The sparse aperture pupil function $P(u,v)$ is the sum of all the subaperture pupil functions:

$$P(u,v) = \sum_{n=1}^{N} p_n(u - u_n, v - v_n), \tag{2.13}$$

where N is the number of subapertures.

Since the optical MTF is the modulus of the OTF, and the pupil functions (2.5) and (2.6) are nonnegative real, then the optical MTF is

$$MTF_{OS}(f_u, f_v) = \left|OTF(f_u, f_v)\right| =$$

$$= \frac{\iint_{A_0} \sum_{n=1}^{N} p_n(u-u_n, v-v_n) \sum_{m=1}^{N} p_m(u-u_m-u_f, v-v_m-v_f)\,du\,dv}{\iint_{A_0} \left[\sum_{n=1}^{N} p_n(u-u_n, v-v_n)\right]^2 du\,dv}; \qquad (2.14)$$

and the objective function (2.10) can be written as

$$J(S_f) =$$

$$= \iint_{S_f} \left\{ \frac{\iint_{A_0} \sum_{n=1}^{N} p_n(u-u_n, v-v_n) \sum_{m=1}^{N} p_m(u-u_m-u_f, v-v_m-v_f)\,du\,dv}{\iint_{A_0} \left[\sum_{n=1}^{N} p_n(u-u_n, v-v_n)\right]^2 du\,dv} - mtf_{des}(f_u, f_v) \right\}^2 df_u\,df_v$$

(2.15)

where A_0 is the area of the aperture. In our case, it is a circle with a radius of R_A.

Now we can formulate the problem. For an aperture consisting of circular subapertures, we need to find the values of u_n, v_n, r_n to obtain the minimum of the function (2.15) subject to the following constraints:

$$g_n \equiv R_A - \left(\sqrt{u_n^2 + v_n^2} + r_n\right) \geq 0, \qquad n = 1, \ldots, N; \qquad (2.16)$$

$$g_{nm} \equiv (u_n - u_m)^2 + (v_n - v_m)^2 - (r_n + r_m)^2 \geq 0, \quad n = 1, \ldots, N\text{-}1, \quad m = n\text{+}1, \ldots, N, \qquad (2.17)$$

$$R_1 \leq r_n \leq R_2, \qquad n = 1, \ldots, N. \qquad (2.18)$$

For an aperture consisting of annular subapertures, the problem is to find the values of u_n, v_n, r_{1n}, r_{2n} to provide the minimum of the function (2.15) subject to the following:

$$g_n \equiv R_A - \left(\sqrt{u_n^2 + v_n^2} + r_{2n}\right) \geq 0, \qquad n = 1, \ldots, N, \qquad (2.19)$$

$$g_{nm} \equiv (u_n - u_m)^2 + (v_n - v_m)^2 - (r_{2n} + r_{2m})^2 \geq 0, \quad n = 1, \ldots, N\text{-}1, \quad m = n\text{+}1, \ldots, N. \qquad (2.20)$$

$$R_{11} \le r_{1n} \le R_{12}, \qquad n = 1, \ldots, N, \tag{2.21}$$

$$R_{21} \le r_{2n} \le R_{22}, \qquad n = 1, \ldots, N. \tag{2.22}$$

Besides, for all the subapertures:

$$-R_A \le u_n \le R_A, \qquad n = 1, \ldots, N, \tag{2.23}$$

$$-R_A \le v_n \le R_A, \qquad n = 1, \ldots, N. \tag{2.24}$$

Here $R_1, R_2, R_{11}, R_{12}, R_{21}, R_{22}$ are bounds of the subaperture radii.

The inequalities (2.16), (2.19) define the conditions that the subapertures are wholly inside the aperture; the inequalities (2.17), (2.20) define the conditions of non-overlap of the subapertures. The double inequalities (2.18), (2.21), (2,22) define bounds of the radii; the (2.23) and (2.24) define possible values of the coordinates of the subaperture centers.

The area S_f can be defined as a circle, ellipse, circular/elliptic annulus, circular/elliptic sector, circular/elliptic annular sector, line segment, and point. In case of the line segment, we have a one-dimensional integral. In case of the point, the objective function shows a square measure of the MTF deviation from the desirable MTF at this frequency point.

2.3. Numerical results

The applied approximation expressions (2.5) and (2.6) have shown good calculation results for some taken arbitrarily test samples of initial aperture configurations. Below four optimization examples are presented.

Tables below show the initial and optimal subaperture parameters: the coordinates of centers and radii. Figures 2.4 – 2.9, 2.11, and 2.12 show the initial and optimal aperture configuration, and the MTFs depending on $f' = \sqrt{f_u'^2 + f_v'^2}$, where the values f_u', f_v' are normalized spatial frequencies relative to the aperture cutoff frequency $f_{cut} = 2R_A / \lambda F$: $f_u' = f_u / f_{cut}$, $f_v' = f_v / f_{cut}$. The angle of the frequency section of the 2-D MTF is shown in the right-top corner of the MTF plots. Figures 2.10 and 2.13 give an opportunity to compare visually the initial and optimal 2-D MTFs for Examples 3 and 4.

The results are calculated with the help of the IMSL® DNCONG routine solving a general nonlinear programming problem using the successive quadratic programming algorithm and a user-supplied gradient. The necessary gradient expressions are shown in Appendix A.

Some parameters for the test calculation are as follow:

- R_A = 1.000,
- $R_1 = R_{21}$ = 0.120,
- $R_2 = R_{22}$ = 0.150,
- R_{11} = 0.050, R_{12} = 0.080,
- η = 1000 for Examples 1, 2, 3; η = 400 for Example 4.

Example 1. Aperture consists of two circular subapertures.

Table 2.1. Initial subaperture parameters.

u_n	v_n	r_n
-0.580	0.070	0.130
-0.710	-0.260	0.140

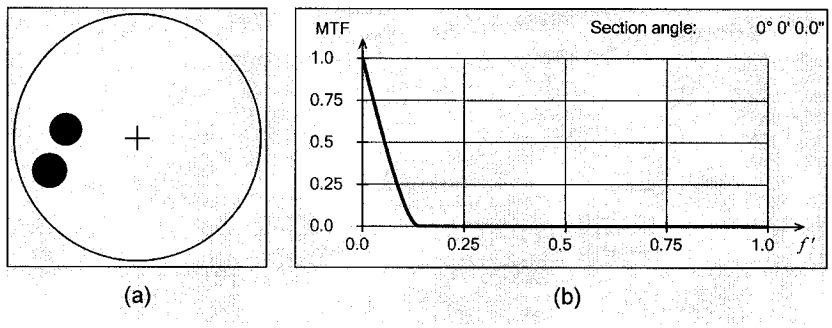

Figure 2.4. Initial configuration (a) and MTF (b).

Table 2.2 and Figure 2.5 show the result of optimization for $mtf_{des}(f_u, f_v) \equiv 0.7$, and for the line segment area of $S_f = \{(f_u, f_v) : 0.495 \le f_u' \le 0.505, \ f_v' = 0.0 \}$.

Table 2.2. Optimal parameters.

u_n	v_n	r_n
0.153	0.109	0.146
-0.847	0.109	0.146

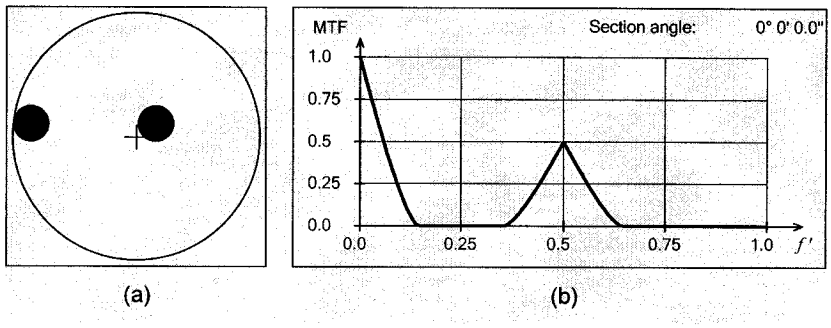

Figure 2.5. Optimal configuration (a) and MTF (b).

We see that the radii of the subapertures become equal, and the distance between the subaperture centers equals 1.0, which corresponds to the maximum possible MTF value, equal to 0.5.

Example 2. Aperture consists of three circular subapertures.

Table 2.3. Initial subaperture parameters.

u_n	v_n	r_n
-0.580	0.070	0.130
-0.710	-0.260	0.140
-0.420	-0.740	0.135

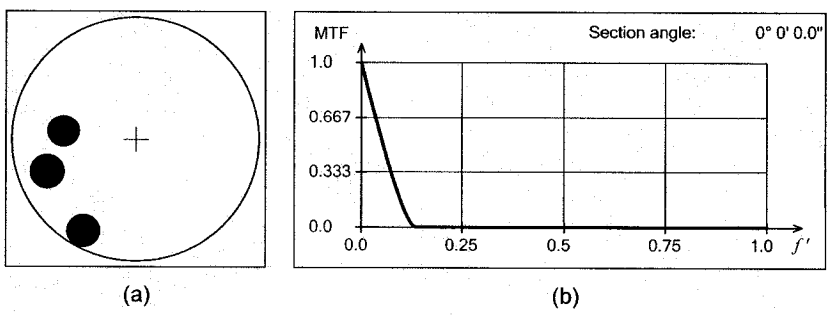

Figure 2.6. Initial configuration (a) and MTF (b).

The following (Table 2.4 and Figure 2.7) are the result of optimization for $mtf_{des}(f_u, f_v) \equiv 0.333$, and for the annular segment area of $S_f = \{(f_u, f_v) :$

$-0.5025 \le f_u' \le 0.5025 \cap 0 \le f_v' \le 0.5025 \cap 0.4975 \le \sqrt{f_u'^2 + f_v'^2} \le 0.5025 \}$.

Table 2.4. Optimal parameters.

u_n	v_n	r_n
-0.337	0.199	0.150
-0.040	-0.740	0.150
0.628	-0.003	0.150

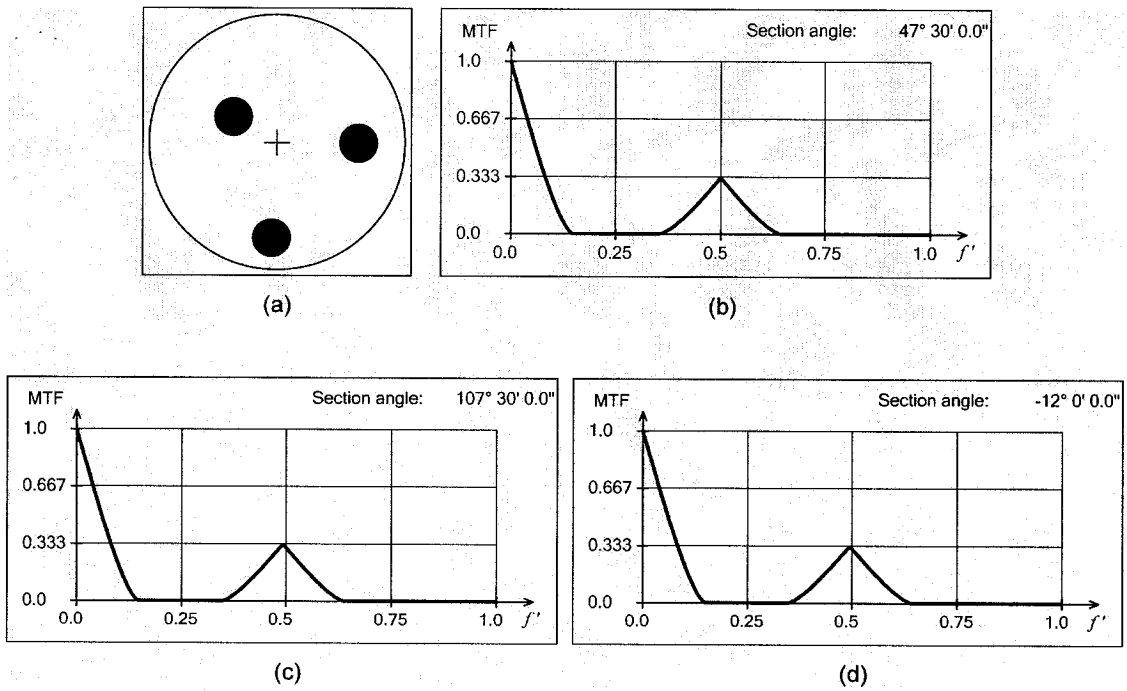

Figure 2.7. Optimal configuration (a) and MTFs for the frequency sections: 47° 30' (b), 107° 30' (c), and -12° 00' (d).

This result shows that the radii of the subapertures become maximal, and the subapertures tend to the vertices of an equilateral triangle (an optimal Golay-3 array[47]). Such behavior of the elements was expected, since the frequency area of interest includes all the possible directions of the frequency vector. The actual value of the distance between the subapertures is defined by the annular bounds of the frequency segment.

Example 3. Aperture consists of three annular subapertures.

Table 2.5. Initial subaperture parameters (3 annuli).

u_n	v_n	r_{1n}	r_{2n}
-0.580	0.070	0.050	0.130
-0.710	-0.260	0.050	0.140
-0.420	-0.740	0.050	0.135

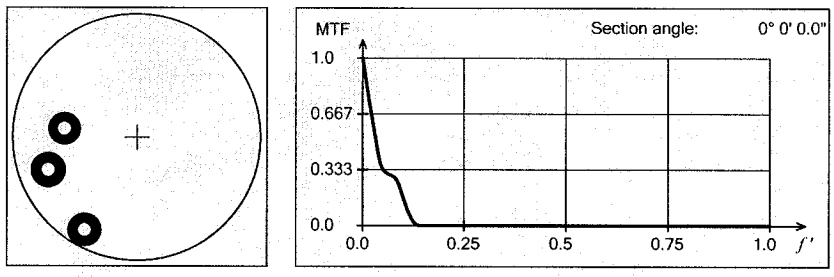

Figure 2.8. Initial configuration and MTF (3 annuli).

Table 2.6 and Figure 2.9 show the result of optimization for $mtf_{des}(f_u, f_v) \equiv 0.333$, and S_f as the frequency annular area: $S_f = \{(f_u, f_v)$:

$-0.5025 \le f_u' \le 0.5025 \cap 0 \le f_v' \le 0.5025 \cap 0.4975 \le \sqrt{f_u'^2 + f_v'^2} \le 0.5025 \}$.

Table 2.6. Optimal parameters (3 annuli).

u_n	v_n	r_{1n}	r_{2n}
-0.158	0.499	0.050	0.150
-0.781	-0.280	0.050	0.150
0.181	-0.437	0.050	0.150

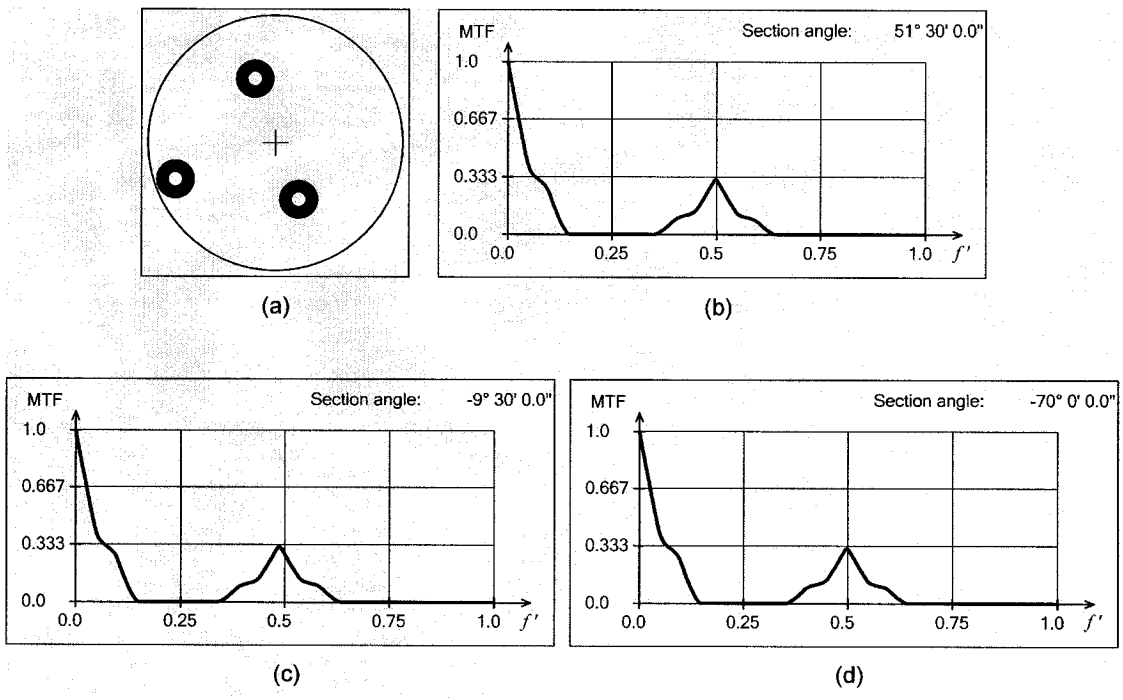

Figure 2.9. Optimal configuration and MTFs for three frequency sections (3 annuli).

We see that, like in Example 2, the outer radii of the subapertures become maximal, and the subapertures tend to the vertices of an equilateral triangle. Moreover, we also see the obvious tendency of the inner radii to be minimal.

Below (Figure 2.10) we can compare visually the initial and optimal 2D MTFs.

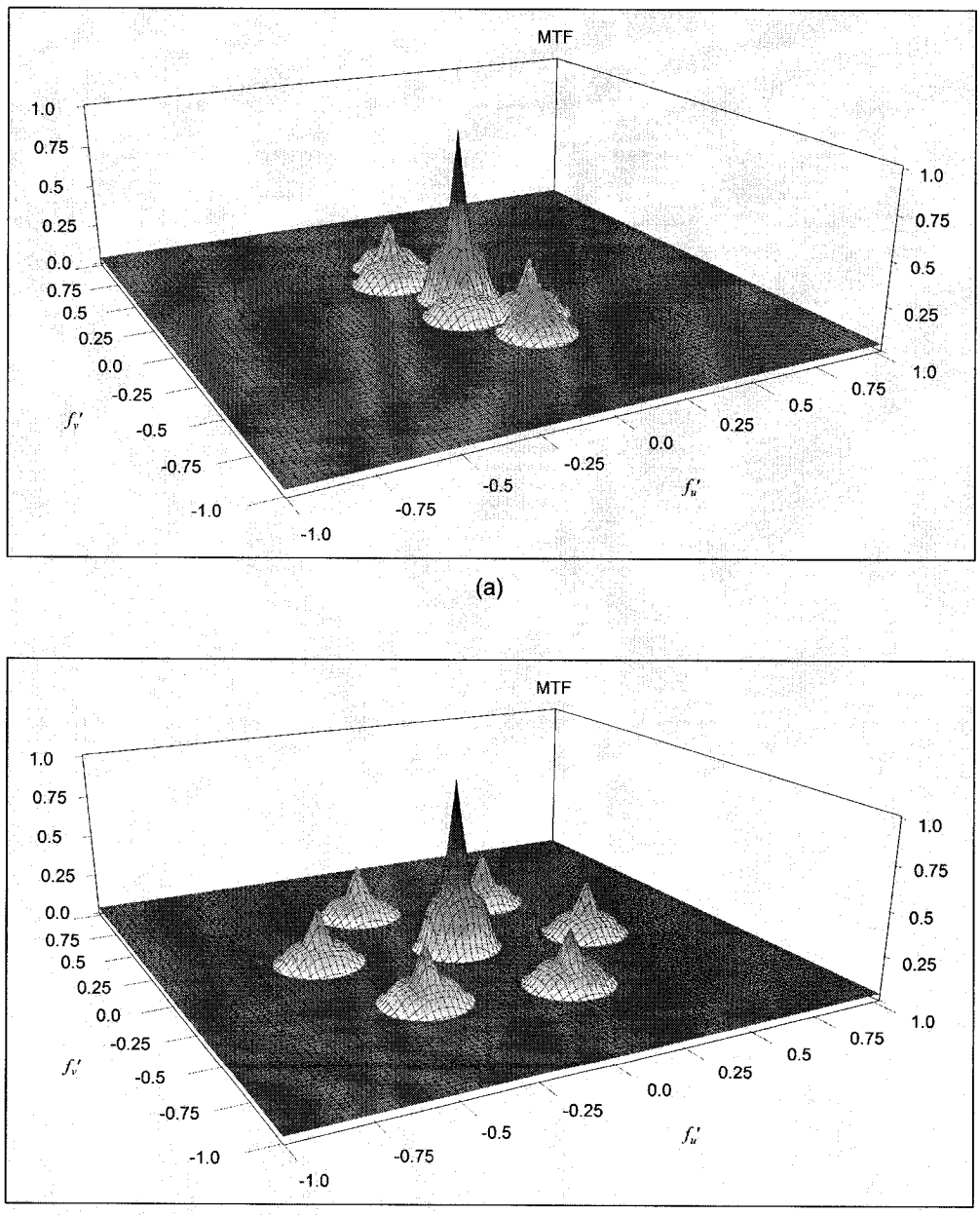

Figure 2.10. Initial (a) and optimal (b) 2D MTFs.

Example 4. Aperture consists of twelve circular subapertures.

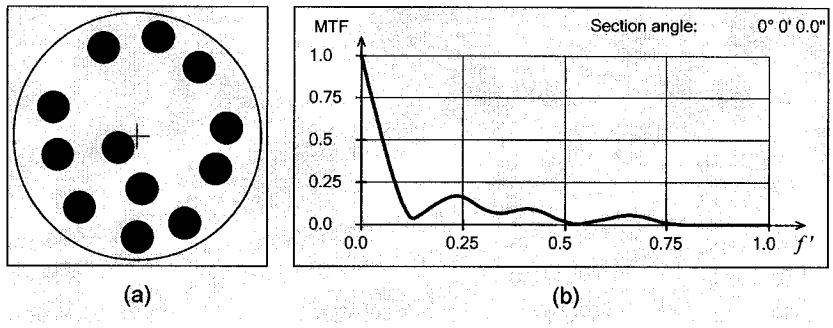

Figure 2.11. Initial configuration (a) and MTF (b) (12 circles).

Figure 2.12 shows the result of optimization for $mtf_{des}(f_u, f_v) \equiv 0.5$, and S_f as the line segment: $S_f = \{(f_u, f_v) : 0.4975 \le f_u' \le 0.5025,\ f_v' = 0.0\}$.

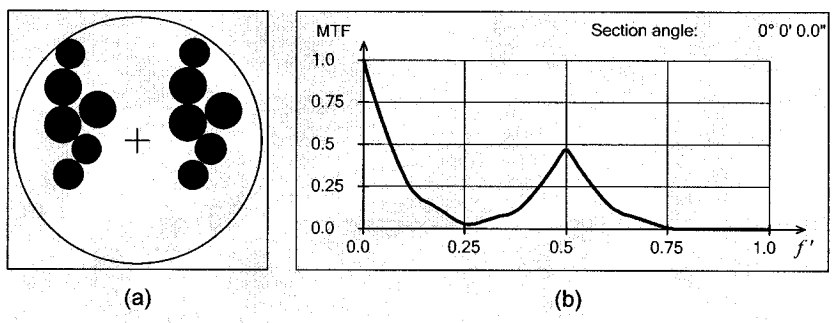

Figure 2.12. Optimal configuration (a) and MTF (b) (12 circles).

The figure shows the aperture that consists of two separated almost identical parts. Such a configuration is typical for the apertures providing the maximal MTF equal to 0.5 at a frequency greater than the maximal cutoff frequency of the subapertures while their maximal diameters are smaller than the aperture radius.

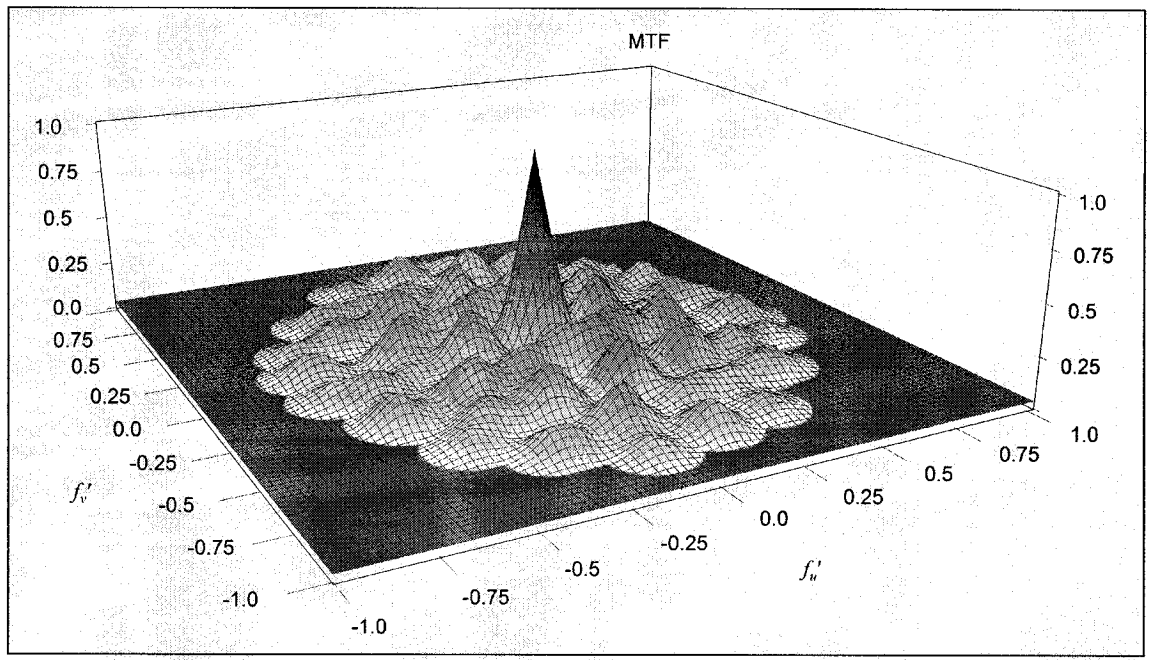

(a)

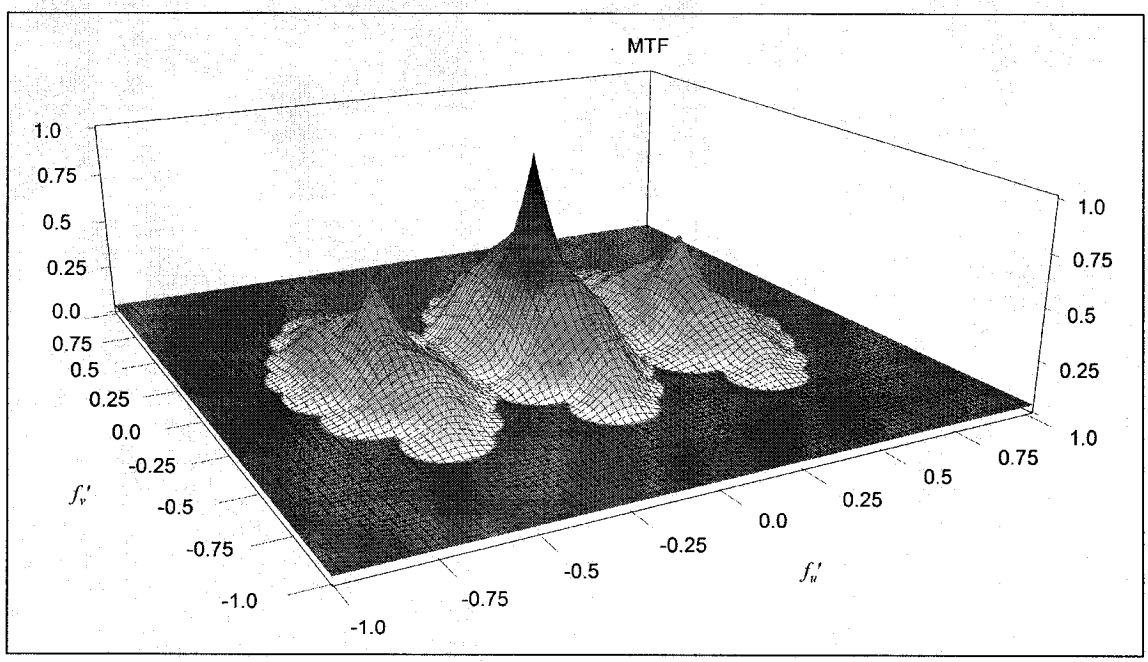

(b)

Figure 2.13. Initial (a) and optimal (b) 2D MTFs.

It is necessary to note that the presented optimal solutions are not unique for a fixed number of subapertures. Their realizations, in our case for the objective function (2.15) and the constraints (2.16) – (2.24), depend on the initial configuration and on the approximation parameter η. However, in a real engineering design, the objective function is more complicated and constraints are more numerous, which can supply a unique solution. In any case, if the optimal solution is not unique and other solutions have the same values of an objective function, any such solution may be accepted for the preliminary developmental work.

2.4. Summary

The results presented in this chapter show an opportunity for solving the problem of aperture configuration optimization using the well-developed fast-convergent gradient methods for nonlinear constrained optimization. It is achieved by approximating the subaperture step pupil functions by functions that are continuously differentiable and have no zero-value regions. The method is demonstrated using examples of circular and annular subapertures typically used in space telescopes. Obviously such an approach can be also applied to the optimization of apertures including subapertures with polygonal shape which are popular for segmented mirror telescopes, and with elliptical shape occurred in the engineering design of non-axially-symmetrical OSs.

Chapter 3

Influence of residual errors of a beam combination system on the OTF

3.1. Instantaneous field distribution in a common focal plane

Let us deduce the expression for the instantaneous spectral field distribution in a common focal plane of a diffraction-limited, improperly phased and aligned, but properly focused optical sparse array on basis of the Fraunhofer approach to the Kirchhoff diffraction theory.

The integral describing the field in the focal plane *XY* for the Fraunhofer diffraction on an aperture is given by[77]

$$U(p,q,\lambda) = C_A \iint_{A_0} \exp[-ik(pu+qv)]dudv\,, \tag{3.1}$$

where $|C_A| = \frac{1}{\lambda}\sqrt{\frac{E_A}{A_0}}$, E_A is all the energy incident on the aperture with the area of A_0, p and q are the values defined by the direction cosines of the object and the image in the coordinate system associated with the aperture center, the Z axis is directed to the side of the light propagation. In accordance with Ex. (3.1), the field from the nth subaperture can be written as

$$U_n(p,q,\lambda) = C_{A_n} \iint_{A_n} \exp[-ik(pu+qv)]dudv, \tag{3.2}$$

where $|C_{A_n}| = \frac{1}{\lambda}\sqrt{\frac{E_{A_n}}{A_n}}$, E_{A_n} is all the energy incident on the subaperture with the area of A_n. Considering the point source located on the Z axis, the values p and q are equal to:

$$p = \frac{x}{F}, \quad q = \frac{y}{F}. \tag{3.3}$$

Substituting the energy density E_D for $\frac{E_{A_n}}{A_n}$, and α for $\frac{k}{F}$, taking the spectral transmittance coefficient $\tau_n \equiv \tau_n(\lambda)$, the p and q from Ex. (3.3), and the phase ϕ_n of the incident wave into account, Ex. (3.2) becomes

$$U_n(x,y,\lambda) = \frac{\sqrt{E_D \tau_n}}{\lambda F} \iint_{A_n} \exp[-i\alpha(xu+yv) + i\phi_n]dudv. \tag{3.4}$$

Let us now consider a case at which the combiner joints parallel beams. Figure 3.1(a) shows such a case for two subapertures where the IA errors are absent.

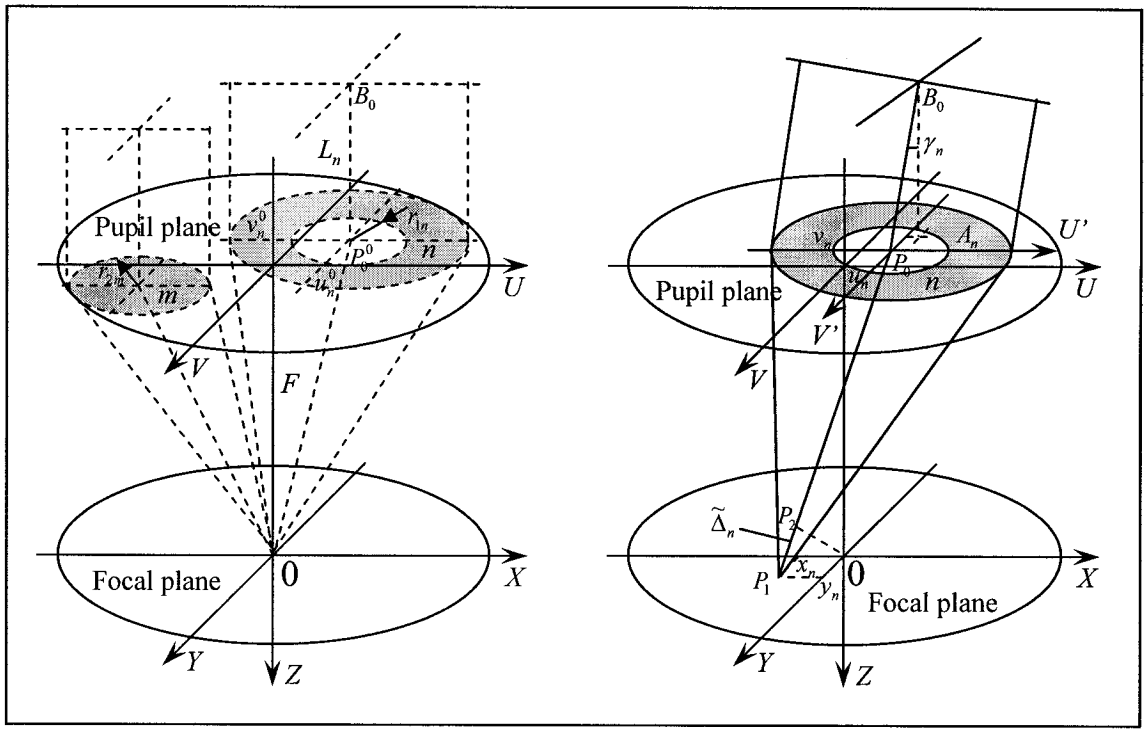

Figure 3.1. Beam combination: ideal ray paths (a); eventual alignment (x_n, y_n) and phasing ($\tilde{\Delta}_n$) errors (b).

The point B_0 is a main ray point around which the random beam tilt takes place. The (u_n^0, v_n^0) are coordinates of the nth subaperture center in the UV-coordinate system in absence of the IA errors. The lines indicate the ideal paths of the equal phase rays.

Here we shall use a simple interdependency of the angle of the beam tilt, changes of the subaperture coordinates, and the IA errors. This interdependency can be described more precisely on basis of the technical characteristics of the combination system, or leaved out of consideration supposing the lengths of the beam combiner levers, $L_n = 0$ (Figure 3.1a).

Now let the angle of the random beam tilt be γ_n. Then coordinates of the nth subaperture center change – they become (u_n, v_n), the IA errors in the XYZ-coordinate system become x_n, y_n. Let the ideal optical path delay and the phasing error of the beam combination be d_n and $\tilde{\Delta}_n(x_n, y_n)$ respectively. The IA errors and the phasing error $\tilde{\Delta}_n \equiv \tilde{\Delta}_n(x_n, y_n)$ for one subaperture are shown in Figure 3.1(b). The lines indicate the eventual paths of the equal phase rays due to the IA errors. Then, introducing the coordinate system $U'V'$ whose origin is coincided with the center of the nth subaperture, Ex. (3.4) is transformed into:

$$U_n(x, y, \lambda) =$$

$$= \frac{\sqrt{E_D \tau_n}}{\lambda F} \iint_{A_n} \exp\left\{-i\alpha\left[(x - x_n)(u' + u_n) + (y - y_n)(v' + v_n)\right] + i\left[\phi_n + k\left(d_n + \tilde{\Delta}_n(x_n, y_n)\right)\right]\right\} du' dv' =$$

$$= \frac{\sqrt{E_D \tau_n}}{\lambda F} \exp\left\{-i\alpha\left[(x - x_n)u_n + (y - y_n)v_n\right] + i\left[\phi_n + k\left(d_n + \tilde{\Delta}_n(x_n, y_n)\right)\right]\right\} \times$$

$$\times \iint_{A_n} \exp\left\{-i\alpha\left[(x - x_n)u' + (y - y_n)v'\right]\right\} du' dv', \qquad (3.5)$$

where, taking the terms of power no greater than unit (in accordance with the Fraunhofer approach), we can get

$$u_n = u_n^0 + \frac{L_n}{F} x_n, \quad v_n = v_n^0 + \frac{L_n}{F} y_n. \qquad (3.6)$$

In polar coordinates:

$$x - x_n = r\cos\varphi, \quad y - y_n = r\sin\varphi, \qquad (3.7)$$

$$u' = \rho\cos\theta, \quad v' = \rho\sin\theta, \qquad (3.8)$$

the integral in Ex. (3.5) is equal to:

$$\iint_{A_n} \exp\{-i\alpha[(x-x_n)u' + (y-y_n)v']\}du'dv' =$$

$$= \int_0^{2\pi}\left\{\int_0^{r_{2n}} \exp[-i\alpha r\rho\cos(\varphi-\theta)]\rho d\rho - \int_0^{r_{1n}} \exp[-i\alpha r\rho\cos(\varphi-\theta)]\rho d\rho\right\}d\theta =$$

$$= \pi r_{2n}^2 \frac{2J_1(\alpha r_{2n} r)}{\alpha r_{2n} r} - \pi r_{1n}^2 \frac{2J_1(\alpha r_{1n} r)}{\alpha r_{1n} r}. \qquad (3.9)$$

Hence, the field from one subaperture at a point (x, y) is equal to:

$$U_n(x,y,\lambda) = \frac{\pi\sqrt{E_D\tau_n}}{\lambda F}\left[r_{2n}^2 \frac{2J_1(\alpha d_{2n}(x,y))}{\alpha d_{2n}(x,y)} - r_{1n}^2 \frac{2J_1(\alpha d_{1n}(x,y))}{\alpha d_{1n}(x,y)}\right]\times$$

$$\times \exp\{-i\alpha b_n(x,y) + i[\phi_n + k(d_n + \tilde{\Delta}_n(x_n,y_n))]\}, \qquad (3.10)$$

where:

$$d_{jn}(x,y) = r_{jn}\sqrt{(x-x_n)^2 + (y-y_n)^2}, \quad j = 1, 2; \qquad (3.11)$$

$$b_n(x,y) = (x-x_n)u_n + (y-y_n)v_n. \qquad (3.12)$$

The summed field from N subapertures takes the form

$$U(x,y,\lambda) = \sum_{n=1}^{N} U_n(x,y,\lambda) =$$

$$= \frac{\pi\sqrt{E_D}}{\lambda F}\sum_{n=1}^{N}\sqrt{\tau_n}\cdot\left[r_{2n}^2 \frac{2J_1(\alpha d_{2n}(x,y))}{\alpha d_{2n}(x,y)} - r_{1n}^2 \frac{2J_1(\alpha d_{1n}(x,y))}{\alpha d_{1n}(x,y)}\right]\times$$

$$\times \exp\{-i\alpha b_n(x,y) + i[\phi_n + k(d_n + \tilde{\Delta}_n(x_n,y_n))]\}. \qquad (3.13)$$

The ideal optical path delay ensures the compensation of the OPDs between the beams, hence we can not take the ϕ_n and d_n into account, but should keep the $\tilde{\Delta}_n(x_n, y_n)$. Thus, the field distribution in a common focal plane of the diffraction-limited, improperly

phased and aligned, but focused optical sparse array consisting of N circular ($r_{1n} = 0$) and annular ($r_{1n} \neq 0$) subapertures becomes

$$U(x,y,\lambda) = \frac{\pi\sqrt{E_D}}{\lambda F}\sum_{n=1}^{N}\sqrt{\tau_n}\cdot\left[r_{2n}^2\frac{2J_1(\alpha d_{2n}(x,y))}{\alpha d_{2n}(x,y)} - r_{1n}^2\frac{2J_1(\alpha d_{1n}(x,y))}{\alpha d_{1n}(x,y)}\right]\times$$

$$\times\exp\left[-i\alpha b_n(x,y) + ik\tilde{\Delta}_n(x_n,y_n)\right]. \tag{3.14}$$

3.2. Instantaneous OTF

Using the fact that an OTF is a normalized Fourier transform of the irradiance distribution, the IOTF of the system can be written as

$$IOTF(f_u,f_v,\lambda) = \frac{\int_{-\infty}^{+\infty}\int|U(x,y,\lambda)|^2\exp[-i2\pi(f_u x + f_v y)]dxdy}{\int_{-\infty}^{+\infty}\int|U(x,y,\lambda)|^2 dxdy}. \tag{3.15}$$

The denominator in Ex. (3.15) is all the energy received by the OS, which is equal to:

$$\int_{-\infty}^{+\infty}\int|U(x,y,\lambda)|^2 dxdy = E_D\pi\sum_{j=1}^{N}\tau_j\left(r_{2j}^2 - r_{1j}^2\right). \tag{3.16}$$

The numerator is the Fourier transform of the irradiance distribution. It can be calculated analytically by direct integration, or applying the convolution theorem, noting that this integral is the Fourier transform of the product of two functions: $U(x,y,\lambda)$ and $U^*(x,y,\lambda)$. It is not difficult to show that for the aperture consisting of identical circular subapertures, the IOTF calculated by direct integration can be expressed in terms of the

generalized hypergeometric function ${}_4F_3(a_1,a_2,a_3,a_4;b_1,b_2,b_3;z)$ which is not so convenient for numeric calculations. On the other hand, the use of the convolution theorem enables to calculate the IOTF according to the light information contained only within the exit pupil, needlessly of a detailed research of the diffraction picture which, sometimes, can be very complicated. Below we show the development of formula for the IOTF, applying the convolution theorem.

Let $\mathfrak{I}\{Z(x,y)\}$ be the Fourier transform of a function $Z(x,y)$. Then, according to the convolution theorem, the Fourier transform of the product of two functions is the convolution of the Fourier transforms of these functions, i.e.:

$$\mathfrak{I}\{Z_1(x,y)\cdot Z_2(x,y)\} = \mathfrak{I}\{Z_1(x,y)\} * \mathfrak{I}\{Z_2(x,y)\}. \tag{3.17}$$

Applying this property to the numerator in Ex. (3.15), it takes the following form:

$$\int_{-\infty}^{+\infty}\int U(x,y,\lambda)\cdot U^*(x,y,\lambda)\cdot\exp[-i2\pi(f_u x + f_v y)]dxdy =$$

$$= \int_{-\infty}^{+\infty}\int\left\{\int_{-\infty}^{+\infty}\int U(x,y,\lambda)\cdot\exp[-i2\pi((f_u-\xi)x+(f_v-\vartheta)y)]dxdy\right\}\times$$

$$\times\left\{\int_{-\infty}^{+\infty}\int U^*(x,y,\lambda)\cdot\exp[-i2\pi(\xi x+\vartheta y)]dxdy\right\}d\xi d\vartheta. \tag{3.18}$$

Analytical calculation of the Fourier transform of the field distribution is shown in Appendix B. This transform is expressed by the following formula:

$$\int_{-\infty}^{+\infty}\int U(x,y,\lambda)\cdot\exp[-i2\pi(\xi x+\vartheta y)]dxdy =$$

$$= \lambda F\sqrt{E_D}\sum_{m=1}^{N}\sqrt{\tau_m}\cdot\exp[-i2\pi(\xi x_m+\vartheta y_m)+ik\tilde{\Delta}_m(x_m,y_m)]\times$$

$$\times[K(\xi,\vartheta,\lambda;u_m,v_m,r_{2m})-K(\xi,\vartheta,\lambda;u_m,v_m,r_{1m})], \tag{3.19}$$

where the function $K(\xi,\vartheta,\lambda;u_m,v_m,r_{jm})$ is defined by Ex. (B9). Using Ex. (3.19), the two inside integrals in Ex. (3.18) can be written in the forms:

$$\int_{-\infty}^{+\infty}\int U(x,y,\lambda)\cdot\exp\left[-i2\pi\left((f_u-\xi)x+(f_v-\vartheta)y\right)\right]dxdy =$$

$$= \lambda F\sqrt{E_D}\sum_{n=1}^{N}\sqrt{\tau_n}\cdot\exp\left\{-i2\pi\left[(f_u-\xi)x_n+(f_v-\vartheta)y_n\right]+ik\tilde{\Delta}_n(x_n,y_n)\right\}\times$$

$$\times\left[K(f_u-\xi,f_v-\vartheta,\lambda;u_n,v_n,r_{2n})-K(f_u-\xi,f_v-\vartheta,\lambda;u_n,v_n,r_{1n})\right], \quad (3.20)$$

and

$$\int_{-\infty}^{+\infty}\int U^*(x,y,\lambda)\cdot\exp\left[-i2\pi(\xi x+\vartheta y)\right]dxdy =$$

$$= \lambda F\sqrt{E_D}\sum_{m=1}^{N}\sqrt{\tau_m}\cdot\exp\left[-i2\pi(\xi x_m+\vartheta y_m)-ik\tilde{\Delta}_m(x_m,y_m)\right]\times$$

$$\times\left[K(\xi,\vartheta,\lambda;-u_m,-v_m,r_{2m})-K(\xi,\vartheta,\lambda;-u_m,-v_m,r_{1m})\right]. \quad (3.21)$$

Now, applying the convolution theorem, the integral (3.18) becomes

$$\int_{-\infty}^{+\infty}\int U(x,y,\lambda)\cdot U^*(x,y,\lambda)\cdot\exp\left[-i2\pi(f_u x+f_v y)\right]dxdy =$$

$$= (\lambda F)^2 E_D\sum_{n=1}^{N}\sqrt{\tau_n}\sum_{m=1}^{N}\sqrt{\tau_m}\iint_{A_n\cap A_m}\exp\left\{-i2\pi\left[(f_u-\xi)x_n+(f_v-\vartheta)y_n\right]+ik\tilde{\Delta}_n(x_n,y_n)\right\}\times$$

$$\times\exp\left[-i2\pi(\xi x_m+\vartheta y_m)-ik\tilde{\Delta}_m(x_m,y_m)\right]d\xi d\vartheta. \quad (3.22)$$

Component parts needed for analytical representation of the Fourier transform of the irradiance distribution are shown in Appendix C. The dynamical phasing error $\tilde{\Delta}_n(x_n,y_n)$ can be represented as the sum of the phasing error $\delta_n(x_n,y_n)$ dependent on x_n and y_n, and the error Δ_n which is the proper piston error of the beam combination system (see Figure 3.1b):

$$\widetilde{\Delta}_n(x_n,y_n)\equiv\widetilde{\Delta}_n=[B_0P_0P_1]-[B_0P_0^0\,0]=[B_0P_0P_1]-[B_0P_0P_2]=\delta_n(x_n,y_n)+\Delta_n. \quad (3.23)$$

The dependent error can be obtained from geometry. In bounds of the Fraunhofer approach:

$$\delta_n(x_n,y_n)\approx-\left(1-\frac{L_n}{F}\right)\frac{u_n^0x_n+v_n^0y_n}{\sqrt{\left(u_n^0\right)^2+\left(v_n^0\right)^2+F^2}}. \quad (3.24)$$

Taking (3.16), (C3), (C8), (C20), (C38), and (C39) into account, and denoting

$$\beta_n=\left(1-\frac{L_n}{F}\right)\frac{k}{\sqrt{\left(u_n^0\right)^2+\left(v_n^0\right)^2+F^2}}, \quad (3.25)$$

and introducing the index function

$$\begin{aligned}
I_{nm}^{gh}(f_u,f_v,\lambda)=\Bigg\{&\frac{\pi r_{gn}}{2b_{nm}}\exp\left(ia_{nm}u_c^{'}\right)\times\\
&\times\Big\{\exp(-i\varphi_{nm})\Big[\mathbf{J}_1(r_{gn}q_{nm},\Theta_{nm}^{gh+})+\mathbf{J}_1(r_{gn}q_{nm},\Theta_{nm}^{gh-})+\\
&+i\left(\mathbf{E}_1(r_{gn}q_{nm},\Theta_{nm}^{gh+})-\mathbf{E}_1(r_{gn}q_{nm},\Theta_{nm}^{gh-})\right)\Big]-\\
&-\exp(i\varphi_{nm})\Big[\mathbf{J}_{-1}(r_{gn}q_{nm},\Theta_{nm}^{gh+})+\mathbf{J}_{-1}(r_{gn}q_{nm},\Theta_{nm}^{gh-})+\\
&+i\left(\mathbf{E}_{-1}(r_{gn}q_{nm},\Theta_{nm}^{gh+})-\mathbf{E}_{-1}(r_{gn}q_{nm},\Theta_{nm}^{gh-})\right)\Big]\Big\}+\\
&+\frac{\pi r_{hm}}{2b_{nm}}\Big\{\exp(i\varphi_{nm})\Big[\mathbf{J}_1(r_{hm}q_{nm},\Theta_{mn}^{hg+})+\mathbf{J}_1(r_{hm}q_{nm},\Theta_{mn}^{hg-})-\\
&-i\left(\mathbf{E}_1(r_{hm}q_{nm},\Theta_{mn}^{hg+})-\mathbf{E}_1(r_{hm}q_{nm},\Theta_{mn}^{hg-})\right)\Big]-\\
&-\exp(-i\varphi_{nm})\Big[\mathbf{J}_{-1}(r_{hm}q_{nm},\Theta_{mn}^{hg+})+\mathbf{J}_{-1}(r_{hm}q_{nm},\Theta_{mn}^{hg-})-\\
&-i\left(\mathbf{E}_{-1}(r_{hm}q_{nm},\Theta_{mn}^{hg+})-\mathbf{E}_{-1}(r_{hm}q_{nm},\Theta_{mn}^{hg-})\right)\Big]\Big\}\Bigg\}, \quad (3.26)
\end{aligned}$$

the IOTF – Ex. (3.15) takes the final form:

$$IOTF(f_u, f_v, \lambda) = \frac{1}{\pi \sum_{j=1}^{N} \tau_j \left(r_{2j}^2 - r_{1j}^2\right)} \times$$

$$\times \sum_{n=1}^{N} \sqrt{\tau_n} \cdot \exp\left[-i\alpha\left(x_n u_f + y_n v_f\right) - i\beta_n\left(u_n^0 x_n + v_n^0 y_n\right) + ik\Delta_n\right] \times$$

$$\times \sum_{m=1}^{N} \sqrt{\tau_m} \cdot \exp\left\{i\alpha\left[\left(x_n - x_m\right)u_m^0 + \left(y_n - y_m\right)v_m^0\right] + i\beta_m\left(u_m^0 x_m + v_m^0 y_m\right) - ik\Delta_m\right\} \times$$

$$\times \left[I_{nm}^{22}(f_u, f_v, \lambda) - I_{nm}^{21}(f_u, f_v, \lambda) - I_{nm}^{12}(f_u, f_v, \lambda) + I_{nm}^{11}(f_u, f_v, \lambda)\right]. \qquad (3.27)$$

The corresponding functions and parameters in Ex. (3.26) are defined in Appendix C.

3.3. Average OTF

The modulus of the function (3.27) gives an Instantaneous MTF (IMTF) which enables to estimate the influence of the IA and OPD errors on the quality of the instantaneous image. Many space-based OESs use the Time Integration Procedure (TIP) for an increase in a SNR. In this connection, the notion "instantaneous quality" is not enough. We need to have a function which will give us the estimate of the image quality at the end of the TIP. The detail description of the image formation process with use of the TIP requires additional parameters, among them statistical properties of the atmosphere, some design characteristics of the OESs (in particular, of the OS and photodetector), and the dynamic characteristics of the bearing satellites, which is out of our consideration. But we can apply an average procedure to the IOTF itself. Note that averaging of the IMTF will not give the desirable result – it is clear from the fact that, for

an aperture consisting of a single subaperture, the IMTF does not depend on the IA errors, which does not correspond to the TIP.

The formula (3.27) is enough to calculate the AOTF, carrying out its statistical averaging over simulated samples of the random values obeying desirable probability distributions within the bounds of the Fraunhofer diffraction. However, for the Gaussian probability distributions, it is possible to average the OTF analytically. We shall show it by the example of developing the necessary integrals for one item in Ex. (3.27) corresponding to $I_{nm}^{22}(f_u, f_v, \lambda)$.

Omitting the normalizing factor, the averaged item can be written in the form:

$$A(f_u, f_v, \lambda; x_n, y_n, x_m, y_m) \cdot B(\lambda, \Delta_n, \Delta_m), \tag{3.28}$$

where:

$$A(f_u, f_v, \lambda; x_n, y_n, x_m, y_m) = \sqrt{\tau_n \tau_m} \cdot \exp\{-i\alpha(x_n u_f + y_n v_f) - i\beta_n(u_n x_n + v_n y_n)\} \times$$

$$\times \exp\{i\alpha[(x_n - x_m)u_m + (y_n - y_m)v_m] + i\beta_m(u_m x_m + v_m y_m)\} \cdot I_{nm}^{22}(f_u, f_v, \lambda), \tag{3.29}$$

$$B(\lambda, \Delta_n, \Delta_m) = \exp[ik(\Delta_n - \Delta_m)]. \tag{3.30}$$

Let the random errors x_n, y_n obey the joint Gaussian probability distribution $p(x_n, y_n)$ with mathematical expectations $\bar{x}_n$, $\bar{y}_n$, and rms deviations σ_{x_n}, σ_{y_n} respectively, and a correlation coefficient $\rho_{x_n y_n}$:

$$p(x_n, y_n) = \frac{1}{2\pi\sigma_{x_n}\sigma_{y_n}\sqrt{1-\rho_{x_n y_n}^2}} \times$$

$$\times \exp\left\{-\frac{1}{2(1-\rho_{x_n y_n}^2)}\left[\frac{(x_n - \bar{x}_n)^2}{\sigma_{x_n}^2} - \frac{2\rho_{x_n y_n}(x_n - \bar{x}_n)(y_n - \bar{y}_n)}{\sigma_{x_n}\sigma_{y_n}} + \frac{(y_n - \bar{y}_n)^2}{\sigma_{y_n}^2}\right]\right\}; \tag{3.31}$$

the errors Δ_n obey the Gaussian distribution $p(\Delta_n)$ with a mathematical expectation $\overline{\Delta}_n$, and a rms deviation σ_{Δ_n}:

$$p(\Delta_n)=\frac{1}{\sqrt{2\pi\sigma_{\Delta_n}^2}}\exp\left\{-\frac{(\Delta_n-\overline{\Delta}_n)^2}{2\sigma_{\Delta_n}^2}\right\}; \tag{3.32}$$

$n=1,...N$. Then the calculated average item is

$$\int_{-\infty}^{+\infty}\int_{-\infty}^{+\infty}\int\int A(f_u,f_v,\lambda;x_n,y_n,x_m,y_m)p(x_n,y_n)dx_n dy_n p(x_m,y_m)dx_m dy_m \times$$

$$\times\int_{-\infty-\infty}^{+\infty+\infty}\int B(\lambda,\Delta_n,\Delta_m)p(\Delta_n)d\Delta_n p(\Delta_m)d\Delta_m\,, \tag{3.33}$$

i.e. it is a product of two independent multiple integrals. The necessary formulas for calculation of the average $A(f_u,f_v,\lambda;x_n,y_n,x_m,y_m)$ and $B(\lambda,\Delta_n,\Delta_m)$ are presented in Appendix D. Now, using Exs. (3.27), (3.33), (D1), (D8), (D26), (D29), and (D30), we get the AOTF in the final form:

$$AOTF(f_u,f_v,\lambda)=\frac{1}{\pi\sum_{j=1}^{N}\tau_j\left(r_{2j}^2-r_{1j}^2\right)}\sum_{n=1}^{N}\sum_{m=1}^{N}Q_{nm}(\lambda)\times$$

$$\times\left\{\left[V_{nm,nm}^{22}(f_u,f_v,\lambda;u,v)+V_{mn,nm}^{22}(f_u,f_v,\lambda;-u,-v)\right]-\right.$$

$$-\left[V_{nm,nm}^{21}(f_u,f_v,\lambda;u,v)+V_{mn,nm}^{21}(f_u,f_v,\lambda;-u,-v)\right]-$$

$$-\left[V_{nm,nm}^{12}(f_u,f_v,\lambda;u,v)+V_{mn,nm}^{12}(f_u,f_v,\lambda;-u,-v)\right]+$$

$$\left.+\left[V_{nm,nm}^{11}(f_u,f_v,\lambda;u,v)+V_{mn,nm}^{11}(f_u,f_v,\lambda;-u,-v)\right]\right\}, \tag{3.34}$$

where the corresponding function and parameters are defined in Appendix D.

Here, with respect to the above developed expressions, it is necessary to notice that:

1) We deduced the formulas within the bounds of the Fraunhofer diffraction, in particular, the source and its image are close to, or on the optical axis, but, for calculation of the average $A(f_u, f_v, \lambda; x_n, y_n, x_m, y_m)$, we used integration in the focal plane over the intervals $(-\infty, +\infty)$. It is acceptable because the contribution of the members which do not meet the Fraunhofer diffraction is negligible for practical values of the statistical parameters of the Gaussian probability distributions for the considered errors.

2) We assumed that the OPDs between any two beams with IA errors $(\bar{x}_n, \bar{y}_n)$ and $(\bar{x}_m, \bar{y}_m)$ are inside the optical coherence length of the radiation. Under such conditions, at imposing the beams from the subapertures, there arises interference effect which determines benefits from the spatial distribution of the subapertures. If the OPDs are more than the coherence length of the received radiation, the result of summation will give the simple sum of the intensities of the separate beams; and, as a result, the cutoff frequency of the optical MTF will be determined by the cutoff frequencies of the separate subapertures without getting the benefits from their spatial distribution. This variant is not interesting, and is not considered in this work.

3.4. Numerical results

The numerical results of computation of the MTFs on basis of the AOTFs (formula 3.34) depending on the IA and OPD errors obeying the Gaussian probability distributions are presented in the following figures for some aperture configurations. The plots (a)

show the aperture configurations; the plots (b) represent MTFs corresponding to plots (a) depending on the IA and OPD error statistical parameters; the plots (c) show the corresponding relative decrease in the ideal MTFs. The argument of the graphic functions is the relative frequency $f' = \sqrt{f_u^2 + f_v^2}\,/\left(2R_A / \lambda F\right)$. The angle of the frequency section of the 2D MTF is shown in the right-top corner of the MTF plot.

The results are calculated with the help of the software developed for the calculation and optimization of design parameters and operational characteristics of the space-based OESs with a distributed aperture. Four routines were used from the IMSL®: ZERFE evaluating the complex scaled complemented error function, DMACH retrieving a real machine constant that defines the computer's double precision arithmetic, DCHFAC computing an upper triangular factorization of a real symmetric nonnegative definite matrix, and DRNMVN generating pseudorandom numbers from a multivariate normal distribution.

Some numerical values:

- $R_A = 1.0$
- $L_n = 1.0$
- $F = 10.0$
- $\lambda = 0.8 \cdot 10^{-6}$
- $\tau_n = 1.0$

for all n. Note that $\gamma_n \approx \dfrac{\sqrt{x_n^2 + y_n^2}}{F}$; hence, for example, for $x_n = y_n = 6.0\lambda$: $\gamma_n \approx 0.14''$.

The following values were used: $\bar{x}_n = \bar{y}_n = 0.0$, $\rho_{x_n y_n} = 0.0$, $\overline{\Delta}_n = 0.0$, $\sigma_{\Delta_n} = 0.0$ for all the subaperture beams (for all n).

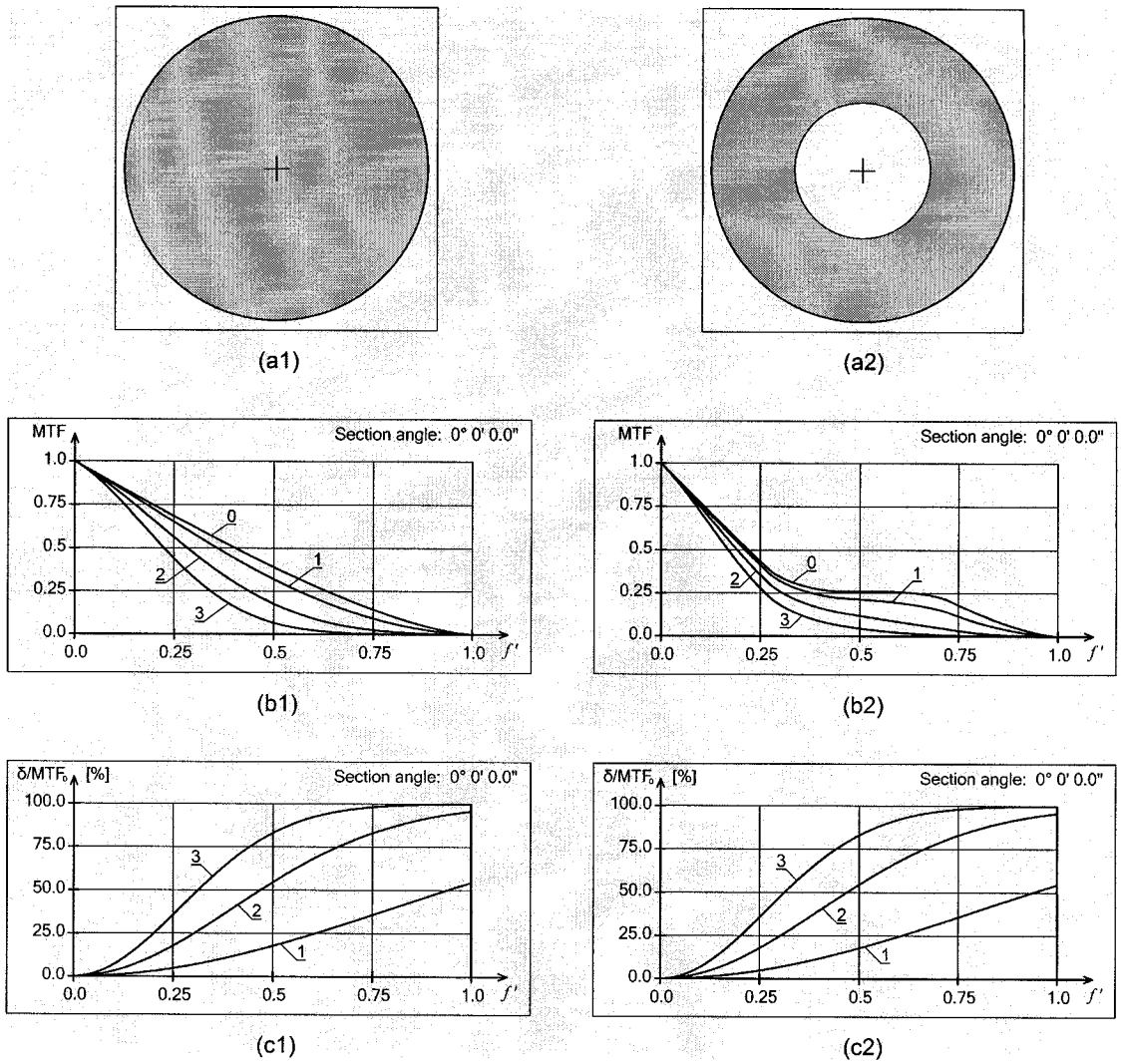

Figure 3.2. The aperture consists of one circular (left), and one annular (right) subaperture with center coordinates (0.0, 0.0), radii $r_2 = 1.0$, and $r_1 = 0.45$ (right). Curves:

0: without IA and OPD errors;

1: $\sigma_{x_1} = \sigma_{y_1} = 1.0\lambda$; **2**: $\sigma_{x_1} = \sigma_{y_1} = 2.0\lambda$; **3**: $\sigma_{x_1} = \sigma_{y_1} = 3.0\lambda$.

This figure shows the practical independence of the relative MTF decrease on the presence of the central screening.

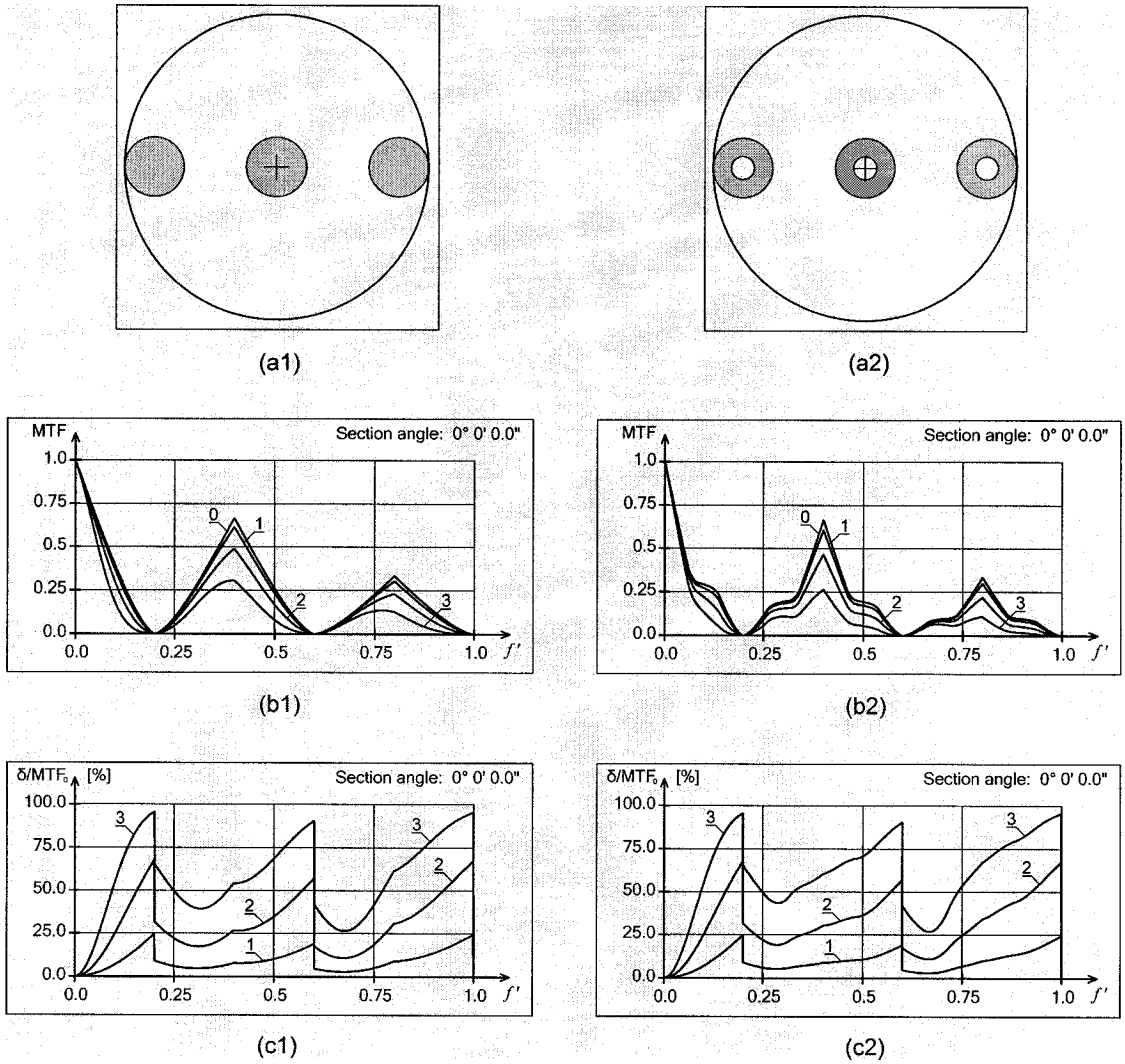

Figure 3.3. The aperture consists of three circular (left), and three annular (right) subapertures with center coordinates (-0.8, 0.0), (0.0, 0.0), (0.8, 0.0), radii $r_{2n} = 0.2$, and $r_{1n} = 0.08$ (right).

Curves:

0: without IA and OPD errors;

1: $\sigma_{x_n} = \sigma_{y_n} = 3.0\lambda$; **2**: $\sigma_{x_n} = \sigma_{y_n} = 6.0\lambda$; **3**: $\sigma_{x_n} = \sigma_{y_n} = 10\lambda$; n = 1, 2, 3.

This figure shows a weak dependence of the relative MTF decrease on the presence of the central screening.

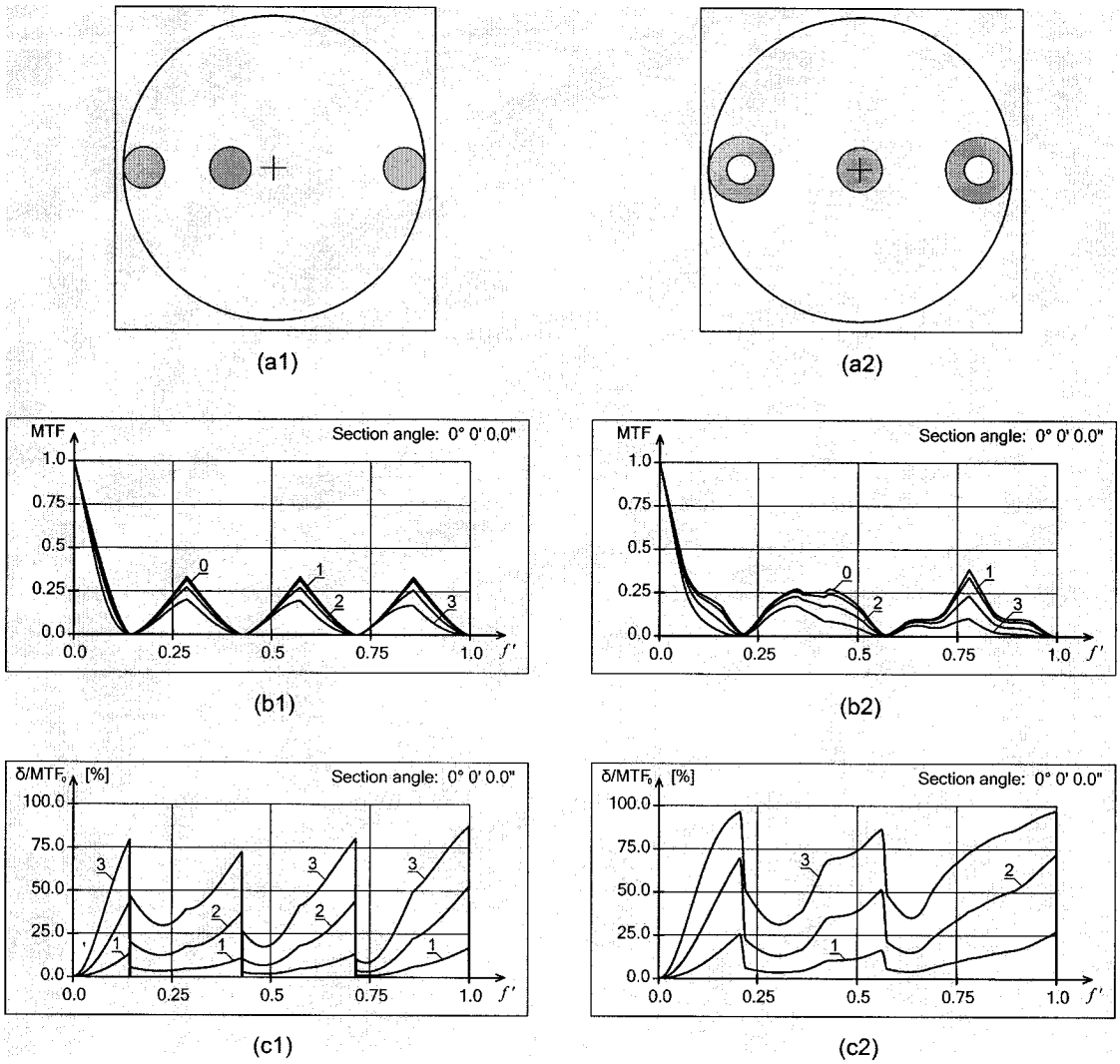

Figure 3.4. The aperture consists of: three circular subapertures (non-redundant array) (left), and mixed subapertures (two annular and one circular) with the following parameters:

left: center coordinates (-0.858, 0.0), (-0.286, 0.0), (0.858, 0.0), radii $r_{2n} = 0.142$;

right: center coordinates (-0.78, 0.0), (0.78, 0.0), radii $r_{2n} = 0.22$ and $r_{1n} = 0.1$, and center coordinates (0.0, 0.0), radius $r_2 = 0.15$.

Curves:

0 : without IA and OPD errors;

1: $\sigma_{x_n} = \sigma_{y_n} = 3.0\lambda$; **2**: $\sigma_{x_n} = \sigma_{y_n} = 6.0\lambda$; **3**: $\sigma_{x_n} = \sigma_{y_n} = 10\lambda$; n = 1, 2, 3.

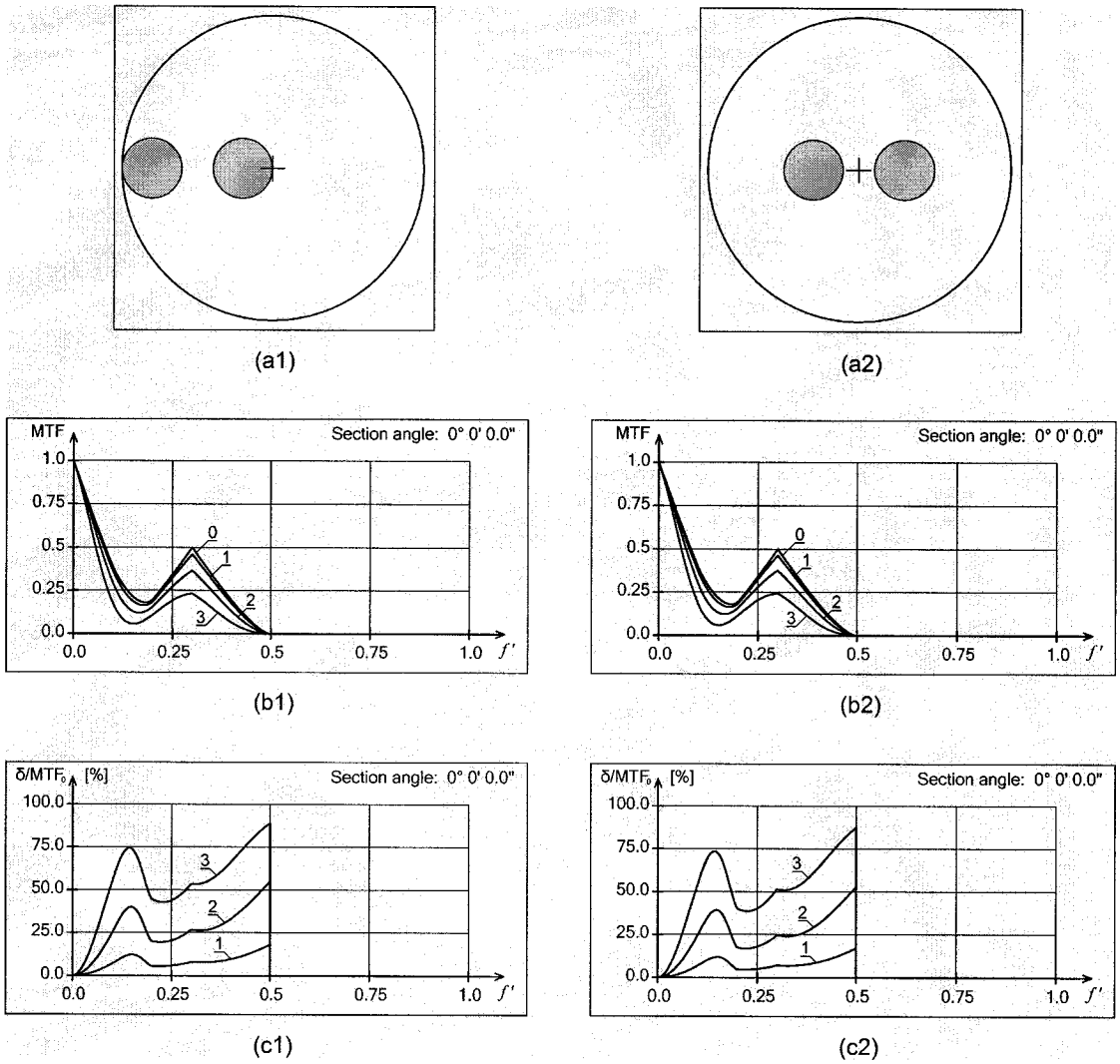

Figure 3.5. The aperture consists of two circular subapertures with radii $r_{2n} = 0.2$, and center coordinates: (-0.8, 0.0) and (-0.2, 0.0) (left), and (-0.3, 0.0) and (0.3, 0.0) (right). Curves:

0 : without IA and OPD errors;

1: $\sigma_{x_n} = \sigma_{y_n} = 3.0\lambda$; **2**: $\sigma_{x_n} = \sigma_{y_n} = 6.0\lambda$; **3**: $\sigma_{x_n} = \sigma_{y_n} = 10\lambda$; n = 1, 2.

Figure 3.5 shows some dependence of the MTF decrease on the position of the subapertures with respect to the aperture center: the farther from the center, the greater the decrease in the MTF.

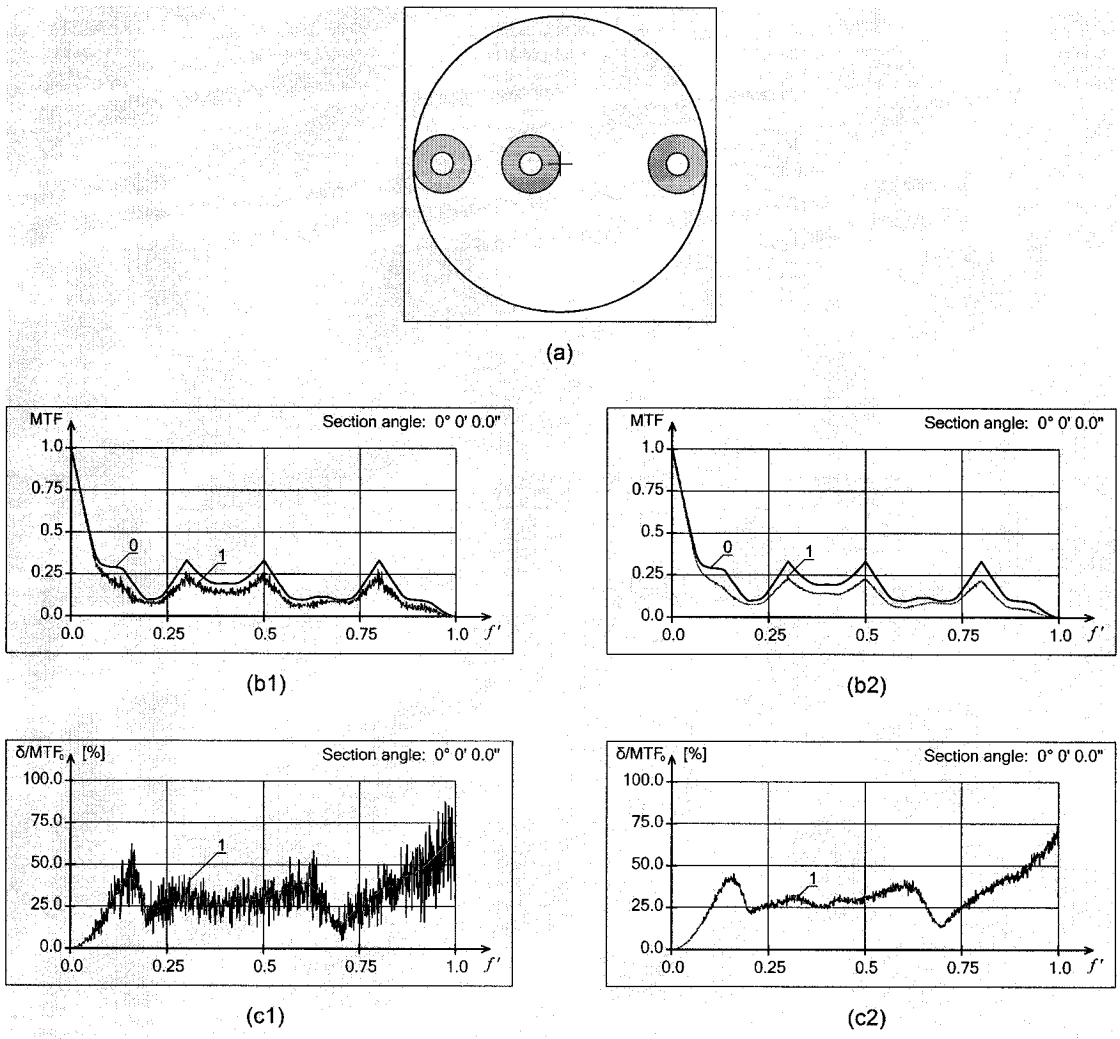

Figure 3.6. The aperture consists of three annular subapertures with center coordinates (-0.8, 0.0), (-0.2, 0.0), (0.8, 0.0), and radii $r_{2n} = 0.2$ and $r_{1n} = 0.08$.

Curves:

0 : without IA and OPD errors;

1: $\sigma_{x_n} = \sigma_{y_n} = 6.0\lambda$; n = 1, 2, 3.

Figure 3.6 shows the comparative results obtained by means of the statistical and analytical averaging. The MTFs (b1 and b2, curves **1**) are calculated in accordance with Ex. (3.27) – IOTF which then were averaged over 10 statistical samples (b1), and 300

ones (b2) with the Gaussian probability distribution. Instead of using the same random value for all the frequencies, the statistical samples were generated sequentially for each shown frequency from lower to upper frequencies. It was done for the better visualization. For comparison, the functions calculated on basis of the analytical averaging (3.34) are drawn inside the curves **1**.

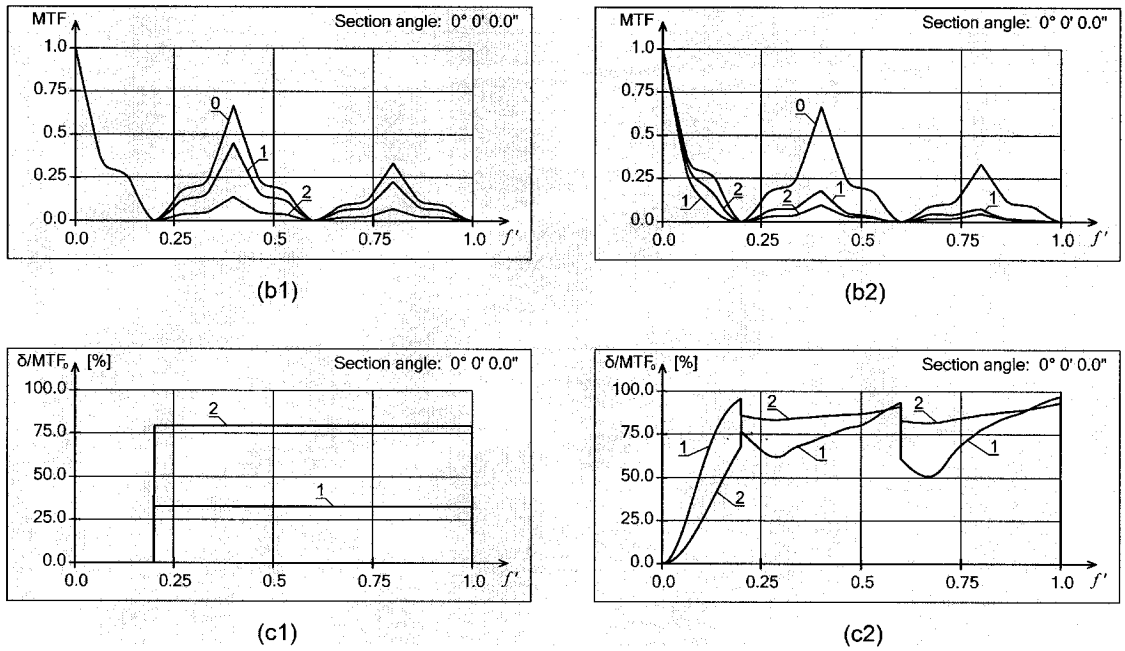

Figure 3.7. The aperture is identical to one in Figure 3.3(a2).

Curves:

0 : without IA and OPD errors;

left: **1**: $\sigma_{\Delta_n} = 0.1\lambda$; **2**: $\sigma_{\Delta_n} = 0.2\lambda$; n = 1, 2, 3;

right: **1**: $\sigma_{x_n} = \sigma_{y_n} = 10.0\lambda$, $\sigma_{\Delta_n} = 0.1\lambda$; **2**: $\sigma_{x_n} = \sigma_{y_n} = 6.0\lambda$, $\sigma_{\Delta_n} = 0.2\lambda$; n = 1, 2, 3.

Figure 3.7 shows the dependence of the MTF on the OPD ($\bar{x}_n = \bar{y}_n = 0.0$, $\rho_{x_n y_n} = 0.0$, $\sigma_{x_n} = \sigma_{y_n} = 0.0$, $\bar{\Delta}_n = 0.0$, $\sigma_{\Delta_n} \neq 0.0$), and on the IA plus OPD ($\bar{x}_n = \bar{y}_n = 0.0$,

$\rho_{x_n y_n} = 0.0$, $\sigma_{x_n} = \sigma_{y_n} \neq 0.0$, $\overline{\Delta}_n = 0.0$, $\sigma_{\Delta_n} \neq 0.0$) error statistical parameters respectively, n = 1, 2. It is interesting to note that, in accordance with Figure 3.7 (right), the IA error has greater influence on the MTF for the frequencies defined by the sizes of one subaperture, while the OPD error has greater influence for the frequencies defined by the value of the subapertures separation.

3.5. Summary

On basis of the Fraunhofer approach to the Kirchhoff diffraction theory, the analytical expression for the IOTF is deduced. It shows the dependence of the IOTF on the residual random IA and OPD errors of a beam combination system for the optical sparse array consisting of N circular and annular subapertures. Application of the average MTF computed on basis of the AOTF calculated with the help of the statistical modeling or the analytical technique, for example, for the Gaussian probability distributions, gives an opportunity to estimate the influence of the IA (or beam tilt) and OPD errors on the resulting image quality, MTF in a common focal plane, and, as a result, on the spatial resolution of the whole OES using the existing conceptions of designing and calculation of the systems with monolithic apertures on the basis of SNR criteria. This estimation can be used to produce the necessary requirements to the accuracy of the beam combination control system, and to define the proportions between the feasible constraints on the IA and OPD errors at the stage of the OES engineering design, taking the technical

characteristics of the beam combination system and permissible deterioration of the image quality into account.

Chapter 4

Optimization of the OES

The purpose of any design of the OES is to create a system whose parameters meet the requirements of the detailed performance specification of a customer. Taking the spatial resolution on the earth surface as the main characteristic of the operation quality of the OES, we shall consider the optimization of design and operating parameters of the OES (the aperture configuration, the effective focal length, and geometrical parameters of the CCD) on basis of a given spatial resolution subject to technical and operating restrictions imposed on some system values.

The resolution of an OES is always limited because of presence of random noise. Therefore, imaging of objects with a prescribed spatial resolution is possible only with some probability determined by the signal and noise levels – SNR.

The optimization procedure on basis of a SNR criterion is more general than only on basis of OS parameters, and it is especially necessary at low levels of the signal light energy and contrast because under such conditions, noise can completely suppress a signal.

Here it is shown one from possible variants of formal descriptions of the OES optimization. We illustrate the application of the step pupil function approximation approach developed in Chapter 2, and conception of the AOTF developed in Chapter 3. They permit to use a gradient optimization method with objective functions formulated in terms of the optical MTF, particularly, using the SNR, and to calculate the influence of the random IA and OPD errors of a beam combination system on the SNR at the optimization of the OES.

The estimation of the potential spatial resolution of the OES requires determining of the relationship between the SNR and the resolution probability taking radiant characteristics of the test object, the distortions of the signal on a path from the object to an estimation point, and noise influence into account. To do it, we need to consider the mathematical models of the applicable SNR criterion of the visual perception, objects, signal distortions, and noise, which take place at the earth surface observation with the space-based OES, understanding that[78] the visual quality of restored images depends on perceptual rather than mathematical considerations varying with the target, the application, and the observer.

4.1. Signal-to-noise ratio

The purpose of use of an OES of observation is forming an image to help the observer, for example, to detect, identify, and classify objects on basis of the perceived useful video information – the signal. Hence, for an estimation of OES quality, it is

necessary to define concepts of the "signal" and "noise", and to use parameters and criteria connected with the perception of images.

The image-exploitation community often uses the National Imagery Interpretability Rating Scale (NIIRS)[79] to quantify the interpretability or usefulness of imagery. It was developed to provide an objective standard for image quality, since the term "image quality" can mean different comprehensions among developers and customers. The NIIRS is expressed in terms of Ground-Sampled Distance (GSD), MTF, SNR, etc. through the Image Quality Equation (IQE)[80] whose function $\mathfrak{I}\{*\}$ determines the relationship between the NIIRS and physical imaging system design and operating parameters:

$$NIIRS = \mathfrak{I}\{GSD, MTF, SNR, etc.\}. \tag{4.1}$$

An analysis shows[81] that the loss in image interpretability, measured as ΔNIIRS, can be modeled as a linear relationship with the noise-equivalent change in reflection. Just the change in reflection of Bar Chart Equivalents of the Object (BCEO) will be used in our consideration; namely, we are going to estimate the system spatial ground resolution on basis of the well-known Johnson's criteria.[82]

4.1.1. Basic notions

Signal and noise

According to the available definitions,[83,84] we shall define the signal in the object plane as the difference between the average value of the energy collected during some time of exposition from the object area and the average value of the energy collected

during the same time from the equal area of the homogeneous background. Then the signal perceived by an observer will be a difference between the values of the image radiance (or equivalent) of the object and the background on a final visualizing device. Noise is a mean-square deviation of the signal.

The Johnson's criteria

As it is well known, Johnson,[82] investigating the systems of image formation, has determined four levels of vision describing the visual perception of images: *detection, orientation, recognition, identification.* Experiments were carried out for several types of military objects. Using the BCEO, he has also determined the number of resolved half-cycles corresponding to the critical size of the objects (usually it is the minimal overall dimension of a projection of the object image on a plane perpendicular to the line of sighting). The widely known Johnson's criteria averaged over the observation object types are shown in Table 4.1.

Table 4.1. Johnson's criteria.

Performance level of vision	Meaning	Number of resolved half-cycles required for 50% probability of the correct decision
Detection	An object is present in the field of view	$2.0^{+1}_{-0.5}$
Orientation	The observer distinguishes the form of object and determines its orientation	$2.8^{+0.8}_{-0.4}$
Recognition	The observer classifies an object (for example, as an automobile, a ship, an airplane, etc.)	$8.0^{+1.6}_{-0.4}$
Identification	The observer determines the type of object (for example, F4 airplane, M48 tank, etc.)	$12.8^{+3.2}_{-2.8}$

It is asserted[85] that the single most important factor determining the level of object discrimination possible with a system is the resolvability of various BCEO of interest. The width of these equivalents is equal to the minimal size of the object, and the length is equal to the size of the object along the line perpendicular to the one of the minimal size. Figure 4.1 illustrates all the Johnson's criteria with a use of such BCEO.

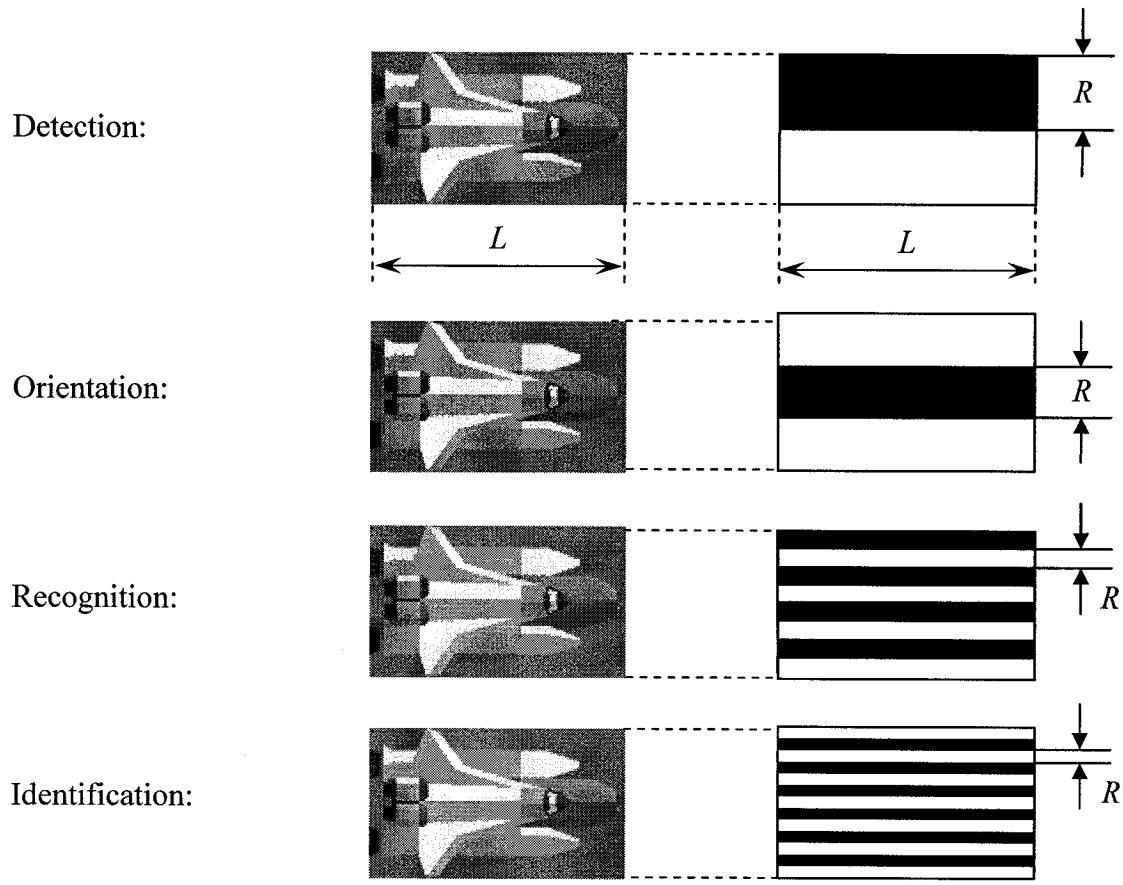

Figure 4.1. Johnson's criteria.

SNR and levels of vision

The visual perception of objects usually occurs on a background of noise of two types: signal-independent additive noise typical for the systems working at a high level of the background, and depending on the signal the multiplicative noise typical for the systems working at a low level of the background.

As it is noted,[86] experiments have shown that, for the additive Gaussian noise, the detection probability is a function of the SNR perceived by an observer. The received

data meet the universal curve establishing the dependence between the detection probability P_D and the perceived SNR SNR_P. This curve represents the integrated law of distribution of the Gaussian probability density:

$$P_D(SNR_P) = \frac{1}{\sqrt{2\pi\sigma_P^2}} \int_{-\infty}^{SNR_P-\mu_P} e^{-\frac{\xi^2}{2\sigma_P^2}} d\xi . \qquad (4.2)$$

The standard deviation σ_P and the value μ_P are estimated as $\sigma_P \approx 1$ and $\mu_P \approx 3.2$. The expression (4.2) determines the fact that the probability of the correct detection of an object equals the probability that the SNR is equal to μ_P, or greater. For multiplicative Poisson noise depending on the signal, it has also been noted that the detection probability expressed in terms of the function of contrast has a form of the normal curve. As to criteria of recognition and identification, it is confirmed their applicability for solving the problems of designing the OESs subject to given characteristics of observation.

Thus, specifying the required value of the visual perception probability, we can always determine the corresponding necessary value of the SNR on the ending information document. And, knowing the structure of the whole imaging complex, it is possible to determine the SNR and NIIRS at the output of any system block.

4.1.2. Basic formulas

The approximate expression for the SNR used for optimization is based on the elementary photometric transforms of the light propagating from the object to the optical focal plane for nadir observation, and on properties of the atmosphere and the TDI CCD.

Test object

Since an OS transforms the illumination distribution in the object space to the illumination distribution in the image space, we are interested in the values of the energy radiance distribution of the observed object and background.

Being based on the Johnson's criteria, the square Test-Objects (TOs) consisting of alternating "light" and "dark" bars are usually used. One such a three bar TO is shown in Figure 4.2. At the observation in visible spectrum, its "light" and "dark" bars are rectangular Lambert areas of size $5R \times R$ with uniform (inside the bar) spectral coefficients of reflection $\rho_1(\lambda)$ and $\rho_2(\lambda)$.

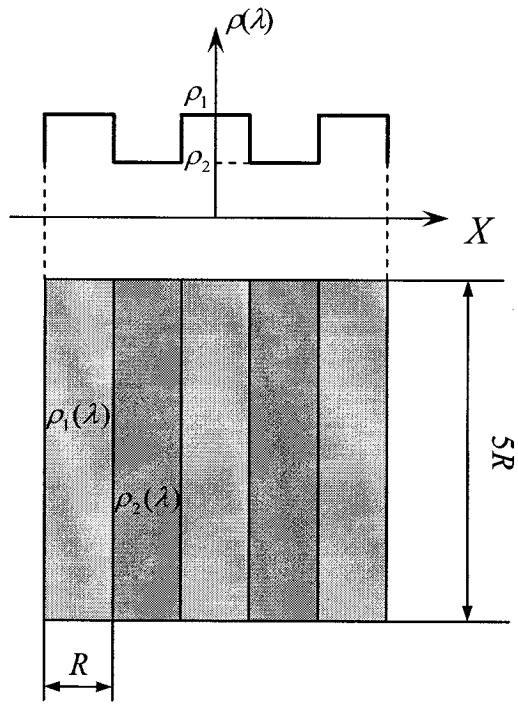

Figure 4.2. Three-bar test object.

The capability of the system to resolve the TO, and consequently to have the resolution not worse than R, is calculated on basis of the difference of signals from the "light" and "dark" bars at a point of the system estimation.

For simplification of calculations, it is convenient to use a hypothetical TO consisting of an infinite number of the alternate "light" and "dark" bars of the width R, laid in the direction of the resolution estimation; and to carry out the calculations on basis of the basic harmonic of the reflection coefficient distribution, the amplitude of which equals

$$\frac{2}{\pi}[\rho_1(\lambda)-\rho_2(\lambda)]. \tag{4.3}$$

Let such an object to lay on a horizontal surface of the earth and be illuminated by the sunlight having the spectral irradiance $I_E(\lambda)$ depending on the solar zenith angle and meteorological conditions. Then the spectral light irradiance distribution in the object plane is

$$L_E(x,\lambda,R)=I_E(\lambda)\left\{\frac{\rho_1(\lambda)+\rho_2(\lambda)}{2}+\frac{2}{\pi}[\rho_1(\lambda)-\rho_2(\lambda)]\cos(\pi\frac{x}{R})\right\}, \tag{4.4}$$

and the spectral radiance distribution is

$$B_E(x,\lambda,R)=\frac{1}{\pi}L_E(x,\lambda,R)=$$

$$=\frac{1}{\pi}I_E(\lambda)\left\{\frac{\rho_1(\lambda)+\rho_2(\lambda)}{2}+\frac{2}{\pi}[\rho_1(\lambda)-\rho_2(\lambda)]\cos(\pi\frac{x}{R})\right\}. \tag{4.5}$$

In this connection, we can consider the values

$$\rho_{ob}(\lambda)=\frac{\rho_1(\lambda)+\rho_2(\lambda)}{2}+\frac{2}{\pi}[\rho_1(\lambda)-\rho_2(\lambda)], \tag{4.5}$$

$$\rho_{bg}(\lambda) = \frac{\rho_1(\lambda) + \rho_2(\lambda)}{2} - \frac{2}{\pi}[\rho_1(\lambda) - \rho_2(\lambda)] \tag{4.6}$$

as the object (target) and background reflection coefficients respectively. Then the object spectral radiance is

$$B_{ob}(\lambda) = \frac{1}{\pi} I_E(\lambda)\rho_{ob}(\lambda); \tag{4.7}$$

and the background spectral radiance is

$$B_{bg}(\lambda) = \frac{1}{\pi} I_E(\lambda)\rho_{bg}(\lambda). \tag{4.8}$$

The solar spectral irradiance $I_E(\lambda)$ is taken in accordance with the ASTM G 173-03,[87] Tables for Reference Solar Spectral Irradiances, for the 1976 U.S. Standard Atmosphere with the absolute air mass of 1.5 (solar zenith angle of 48.19°), Figure 4.3.

As the "light" bar spectral reflectance coefficients $\rho_1(\lambda)$, the coefficient of Olive Green Paint – "Object 1", and the coefficient of Copper Metal 2 – "Object 2" are taken; as the "dark" bar reflectance coefficient $\rho_2(\lambda)$, the reflectance of Brown Sandy Loam is taken – as documented in the ASTER spectral library,[88] Figure 4.4.

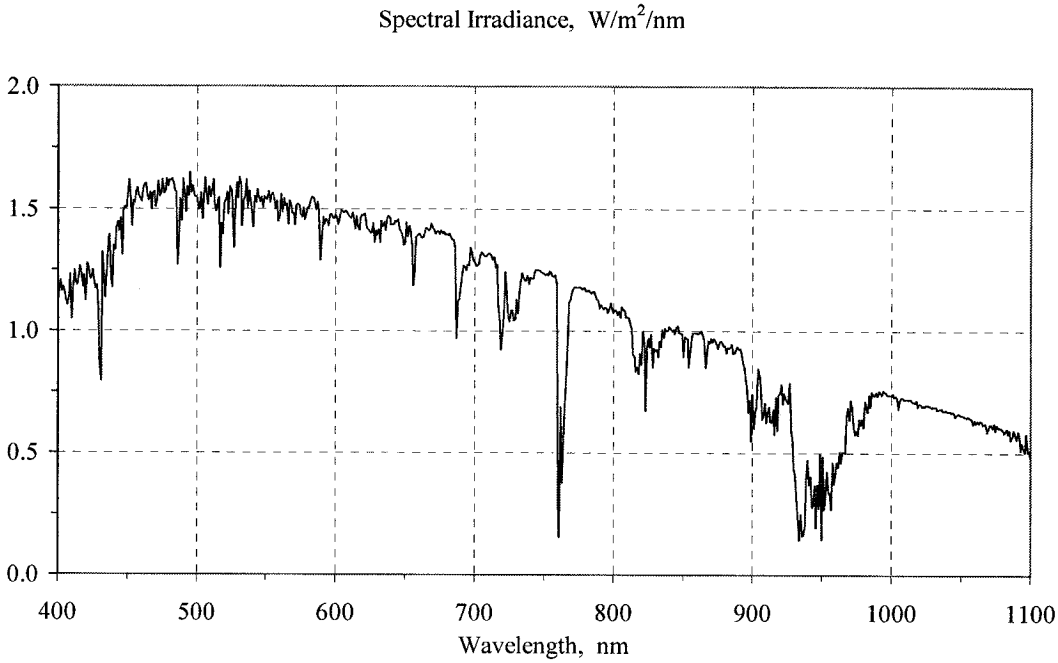

Figure 4.3. Solar spectral irradiance.

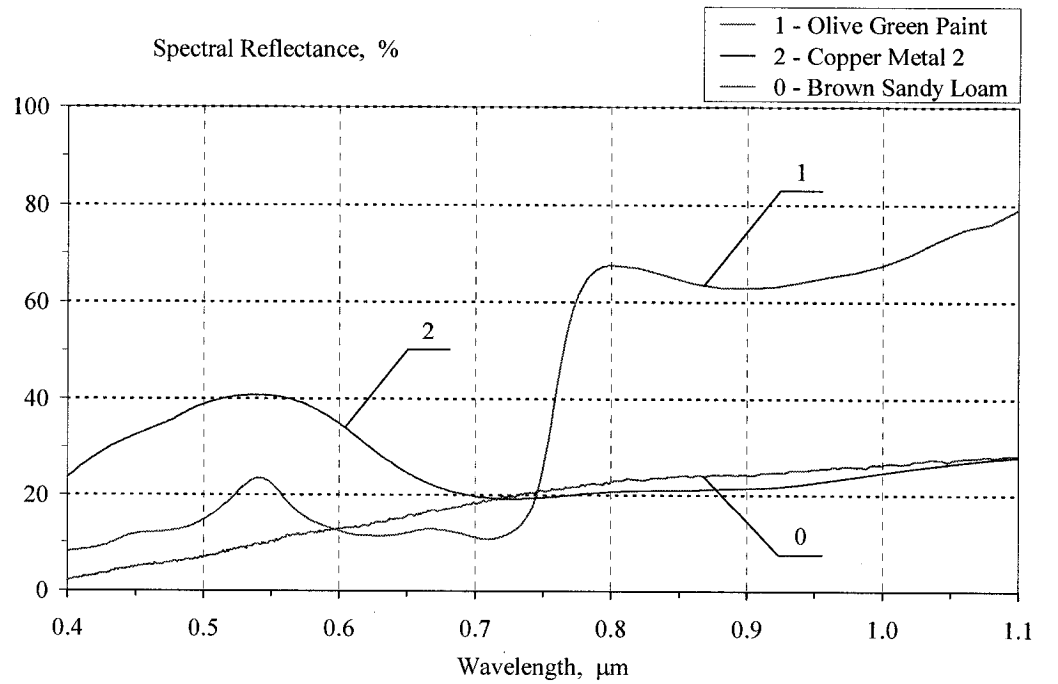

Figure 4.4. Spectral reflectance for the "object" – 1 and 2, and the "background" – 0.

Atmosphere

As well known, Earth's atmosphere influences both the amplitude and phase of the propagating light, and introduces the haze radiation to received signals. The atmospheric noise can be divided into three main parts:

- the noise due to the interference of the propagating optical signal with the atmosphere;
- the phone noise caused by scattering the light from diverse sources such as the Sun, an underlying surface, etc.;
- the atmosphere self-radiation caused, for example, by its non-zero value of temperature.

The first part consists of additive and multiplicative noise that distorts the value and the form of the signal. The second part is represented by additive noise which is summed with the signal, and consists of both the slowly changed over day component and the rapidly changed random one. The third part consists of additive noise; it is important for calculation of IR-systems. For our consideration, the multiplicative and nonlinear amplitude and phase distortions due to the scattering, and the amplitude and phase fluctuation of wave are taking into account by means of the spectral optical transmittance coefficient $\tau_A(\lambda)$, and the spectral MTF Reduction Factor (MRF) $MRF_A(f,\lambda)$ associated with atmospheric turbulence. The additive noise due to the scattering and self-radiation is presented by the spectral haze radiance $B_h(\lambda)$.

The transmittance coefficient depends on a lot of atmosphere scattering parameters. First of all, the scattering occurs on air density fluctuations (molecular scattering), on aerosol particles (aerosol scattering), and on non-uniformities of the atmosphere due to

the air turbulent motion. We can use conventional values[89] describing some particular case of the propagation of radiation, Figure 4.5.

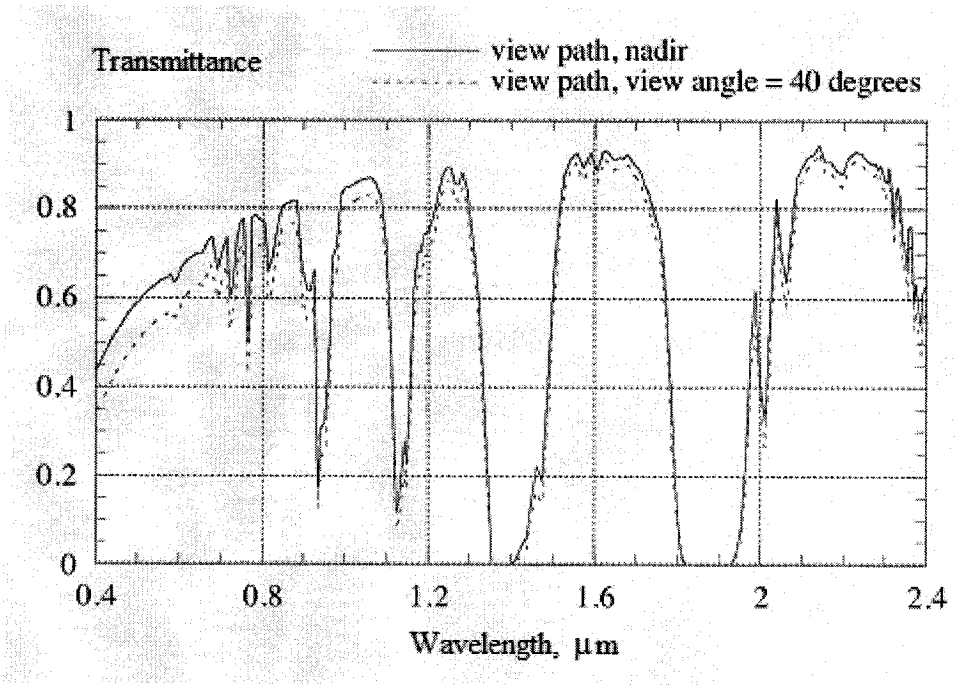

Figure 4.5. Atmosphere's transmittance.

As to values of the spectral haze radiance, the data[90] calculated with the uniform field defined as 50% reflective and viewed from a nadir sensor at 20-km altitude with a 45° sun for an aerosol-free atmosphere (Rayleigh scattering only) were used.

In the ground-based astronomy, one distinguishes the short-time and the long-time exposure. The short-time exposure corresponds to the exposure time τ_e which less than the wavefront coherence time τ_0 defined by[91]

$$\tau_0 = 0.31\frac{r_0}{V_0}, \tag{4.9}$$

while the long-time exposure corresponds to $\tau_e > \tau_0$. Here r_0 is the characteristic length of Kolmogorov turbulence[92] (or the Fried parameter), V_0 is the average velocity of turbulence (the wind velocity averaged over the altitude). The numerical estimations of r_0 depend on the real atmosphere conditions which the system is planed to be used at, and are calculated for the chosen specific model of the atmosphere. For good daily conditions of observation of astronomical objects, looking up, r_0 is about 15 – 25 cm for the wavelength of 0.5 μm. Hence, for example, for V_0 = 20 m/s, and r_0 = 25 cm, we have $\tau_0 \approx 3.88$ ms. But with respect to observations from a satellite, this time is much less, and we have, as a rule, a long-time exposure.

The MRF of the turbulent atmosphere for a long-time exposure is independent of the OS and can be written as[93,94]

$$MRF_A(f,\lambda) = \exp\{-0.5 D_w(r,\lambda)\}, \tag{4.10}$$

where $D_w(r,\lambda)$ is the wave structure function of turbulence; r is a distance between two points in the pupil plane, corresponding to the spatial frequency $f = r/(\lambda F)$. For satellite viewing, looking down from an altitude H, on the basis of a theory for isotropic turbulence developed by Kolmogorov,[92] the wave structure function is given by[95]

$$D_w(r,\lambda) = 2.91 k^2 r^{5/3} \int_0^H C_n^2(x) \left(\frac{x}{H}\right)^{5/3} dx. \tag{4.11}$$

Using a model[96] of the vertical distribution of the refractive index structure function $C_n^2(x)$:

$$C_n^2(x) = 6.7 \cdot 10^{-14} \left(2x^{1/2}\right)^{-2/3} \exp\left(-\frac{x}{h_0}\right), \qquad h_0 = 3200; \tag{4.12}$$

and the relation $f = \frac{H}{F}\frac{1}{2R}$, the wave structure function takes the form:

$$D_w(R,\lambda) = 2.3\cdot 10^{-4} R^{-5/3}\lambda^{-1/3}\gamma\left(\frac{7}{3},\frac{H}{3200}\right), \tag{4.13}$$

where $\gamma(a,b)$ is the incomplete gamma function; all dimensions are in mks units.

Optical system

The OS forms a united image in a common focal plane: the beam combination system joins together the beams from the subapertures. Due to a limited accuracy of the beam combination control system, the combiner introduces some optical errors influencing the quality of the united image. As shown in Chapter 3, the influence of the residual random IA and OPD errors for a diffraction-limited, properly focused but improperly phased and aligned optical sparse array can be accounted through the modulus of the AOTF. Here we use the AOTF, $AOTF_\eta(f,\lambda)$ depending on the parameter η determining the accuracy of the step pupil function approximation (see Chapter 2). The expression for the η -dependent AOTF can be obtained from the following.

Let the random errors x_n, y_n obey the probability distribution (3.31), and the errors Δ_n obey Ex. (3.32). Then, taking the approximated annular subaperture step pupil function, Ex. (2.26), and the parameters of the IA and OPD errors, Exs. (3.23) – (3.25) into account, the Fourier transform of the irradiance distribution in the focal plane, Ex. (C3) averaged over all x_n, y_n, and Δ_n ($\langle . \rangle$ is an averaging operator) takes the form:

$$\left\langle \int_{-\infty}^{+\infty}\int U(x,y,\lambda)\cdot U^{*}(x,y,\lambda)\cdot \exp\left[-i2\pi\left(f_u x + f_v y\right)\right]dxdy \right\rangle =$$

$$= E_D \int_{-\infty}^{+\infty}\int \sum_{n=1}^{N} \sqrt{\tau_n}\cdot \int_{-\infty}^{+\infty}\int \exp\left[i\alpha\cdot\left(x_n(u-u_f)+y_n(v-v_f)\right)-i\beta_n\left(u_n^0 x_n + v_n^0 y_n\right)\right]\times$$

$$\times p(x_n,y_n)dx_n dy_n \cdot \int_{-\infty}^{+\infty}\exp\left[ik\Delta_n\right]p(\Delta_n)d\Delta_n \times$$

$$\times\frac{1}{\pi}\left\{\arctan\left[\eta\cdot\left((u-u_n^0-u_f)^2+(v-v_n^0-v_f)^2-r_{1n}^2\right)\right]-\right.$$

$$\left.-\arctan\left[\eta\cdot\left((u-u_n^0-u_f)^2+(v-v_n^0-v_f)^2-r_{2n}^2\right)\right]\right\}\times$$

$$\times\sum_{m=1}^{N}\sqrt{\tau_m}\cdot\int_{-\infty}^{+\infty}\int\exp\left\{-i\alpha\cdot\left(x_m u + y_m v\right)+i\beta_m\left(u_m^0 x_m + v_m^0 y_m\right)\right\}p(x_m,y_m)dx_m dy_m \times$$

$$\times\int_{-\infty}^{+\infty}\exp\left[-ik\Delta_m\right]p(\Delta_m)d\Delta_m \times$$

$$\times\frac{1}{\pi}\left\{\arctan\left[\eta\cdot\left((u-u_m^0)^2+(v-v_m^0)^2-r_{1m}^2\right)\right]-\right.$$

$$\left.-\arctan\left[\eta\cdot\left((u-u_m^0)^2+(v-v_m^0)^2-r_{2m}^2\right)\right]\right\}dudv\,. \qquad (4.14)$$

It is easy to show that the AOTF which is Ex. (4.14) normalized by the factor $\pi\sum_{j=1}^{N}\tau_j\left(r_{2j}^2-r_{1j}^2\right)$ is

$$AOTF_\eta(f,\lambda)=\frac{1}{\pi\sum_{j=1}^{N}\tau_j\left(r_{2j}^2-r_{1j}^2\right)}\times$$

$$\times\sum_{n=1}^{N}\frac{1}{2\sigma_{x_n}\sigma_{y_n}\sqrt{1-\rho_{x_n y_n}^2}}\frac{\sqrt{\tau_n}}{\sqrt{A_1 A_2}}\exp\left[-\left(S_{x_n}\bar{x}_n^2+S_{y_n}\bar{y}_n^2\right)+S_{x_n y_n}\bar{x}_n\bar{y}_n\right]\times$$

$$\times\frac{1}{\pi}\left\{\arctan\left[\eta\cdot\left((u-u_n^0-u_f)^2+(v-v_n^0-v_f)^2-r_{1n}^2\right)\right]-\right.$$

$$- \arctan\left[\eta \cdot \left((u-u_n^0-u_f)^2+(v-v_n^0-v_f)^2-r_{2n}^2\right)\right]\Big\}\times$$

$$\times\left\{\sum_{\substack{m=1\\ m\neq n}}^{N}\frac{1}{2\sigma_{x_m}\sigma_{y_m}\sqrt{1-\rho_{x_m y_m}^2}}\frac{\sqrt{\tau_m}}{\sqrt{A_3 A_4}}\exp\left[-\left(S_{x_m}\bar{x}_m^2+S_{y_m}\bar{y}_m^2\right)+S_{x_m y_m}\bar{x}_m\bar{y}_m\right]\times\right.$$

$$\times\int_{-\infty}^{+\infty}\int\exp\left[\frac{B_1^2}{4A_1}+\frac{B_2^2}{4A_2}+\frac{B_3^2}{4A_3}+\frac{B_4^2}{4A_4}\right]\times$$

$$\times\frac{1}{\pi}\left\{\arctan\left[\eta\cdot\left((u-u_m^0)^2+(v-v_m^0)^2-r_{1m}^2\right)\right]-\right.$$

$$\left.-\arctan\left[\eta\cdot\left((u-u_m^0)^2+(v-v_m^0)^2-r_{2m}^2\right)\right]\right\}dudv\times$$

$$\times\exp\left[-\frac{k^2}{2}\left(\sigma_{\Delta_n}^2+\sigma_{\Delta_m}^2\right)+ik\left(\bar{\Delta}_n-\bar{\Delta}_m\right)\right]+$$

$$+\sqrt{\tau_n(\lambda)}\int_{-\infty}^{+\infty}\int\exp\left[\frac{B_5^2}{4A_1}+\frac{B_6^2}{4A_2}\right]\times$$

$$\times\frac{1}{\pi}\left\{\arctan\left[\eta\cdot\left((u-u_n^0-u_f)^2+(v-v_n^0-v_f)^2-r_{1n}^2\right)\right]-\right.$$

$$\left.-\arctan\left[\eta\cdot\left((u-u_n^0-u_f)^2+(v-v_n^0-v_f)^2-r_{2n}^2\right)\right]\right\}\times$$

$$\times\frac{1}{\pi}\left\{\arctan\left[\eta\cdot\left((u-u_n^0)^2+(v-v_n^0)^2-r_{1n}^2\right)\right]-\right.$$

$$\left.\left.-\arctan\left[\eta\cdot\left((u-u_n^0)^2+(v-v_n^0)^2-r_{2n}^2\right)\right]\right\}dudv\right\}, \qquad (4.15)$$

where:

$$A_1=S_{x_n},\qquad B_1=2S_{x_n}\bar{x}_n-S_{x_n y_n}\bar{y}_n+i\alpha\left(u-u_f\right)-i\beta_n u_n^0,\qquad C_1=S_{x_n y_n},$$

$$A_2=S_{y_n}-\frac{C_1^2}{4A_1},\qquad B_2=2S_{y_n}\bar{y}_n-S_{x_n y_n}\bar{x}_n+i\alpha\left(v-v_f\right)-i\beta_n v_n^0+\frac{B_1 C_1}{2A_1},$$

$$A_3=S_{x_m},\qquad B_3=2S_{x_m}\bar{x}_m-S_{x_m y_m}\bar{y}_m-i\alpha u+i\beta_m u_m^0,\qquad C_3=S_{x_m y_m},$$

$$A_4 = S_{y_m} - \frac{C_3^2}{4A_3}, \quad B_4 = 2S_{y_m}\bar{y}_m - S_{x_m y_m}\bar{x}_m - i\alpha v + i\beta_m v_m^0 + \frac{B_3 C_3}{2A_3},$$

$$B_5 = 2S_{x_n}\bar{x}_n - S_{x_n y_n}\bar{y}_n - i\alpha u_f, \qquad B_6 = 2S_{y_n}\bar{y}_n - S_{x_n y_n}\bar{x}_n - i\alpha v_f + \frac{B_5 C_1}{2A_1},$$

$$S_{x_n} = \frac{1}{2\sigma_{x_n}^2\left(1-\rho_{x_n y_n}^2\right)}, \quad S_{x_n y_n} = \frac{\rho_{x_n y_n}}{\sigma_{x_n}\sigma_{y_n}\left(1-\rho_{x_n y_n}^2\right)}, \quad S_{y_n} = \frac{1}{2\sigma_{y_n}^2\left(1-\rho_{x_n y_n}^2\right)},$$

$$S_{x_m} = \frac{1}{2\sigma_{x_m}^2\left(1-\rho_{x_m y_m}^2\right)}, \quad S_{x_m y_m} = \frac{\rho_{x_m y_m}}{\sigma_{x_m}\sigma_{y_m}\left(1-\rho_{x_m y_m}^2\right)}, \quad S_{y_m} = \frac{1}{2\sigma_{y_m}^2\left(1-\rho_{x_m y_m}^2\right)}. \quad (4.16)$$

Taking the parameters of the atmosphere and the OS into account, the component values of irradiance from the object, background, and haze in the focal plane can be written as:

$$I_{ob}(f,\lambda) = B_{ob}(\lambda)\cdot\tau_A(\lambda)\cdot MRF_A(f,\lambda)\cdot\frac{\pi\sum_{n=1}^{N}\tau_n\left(r_{2n}^2 - r_{1n}^2\right)}{F^2}\cdot\left|AOTF_\eta(f,\lambda)\right|, \quad (4.17)$$

$$I_{bg}(f,\lambda) = B_{bg}(\lambda)\cdot\tau_A(\lambda)\cdot MRF_A(f,\lambda)\cdot\frac{\pi\sum_{n=1}^{N}\tau_n\left(r_{2n}^2 - r_{1n}^2\right)}{F^2}\cdot\left|AOTF_\eta(f,\lambda)\right|, \quad (4.18)$$

$$I_h(\lambda) = B_h(\lambda)\cdot\frac{\pi\sum_{n=1}^{N}\tau_n\left(r_{2n}^2 - r_{1n}^2\right)}{F^2}. \quad (4.19)$$

Photodetector

Distortions of the signal at photodetecting with the TDI-CCD can be described by means of the basic characteristics of the CCDs which associate with the concept of the spatial resolution: the CCD MTF influencing a signal, and noise.

MTF

The MTF of the TDI-CCD is basically determined by five factors:[97,98]

- *charge integration*
- *discrete charge motion*
- *charge transfer inefficiency*
- *charge diffusion*
- *mismatch of the velocities of the charge transfer and image motion.*

Figure 4.6 shows the layout of the elements in the CCD.

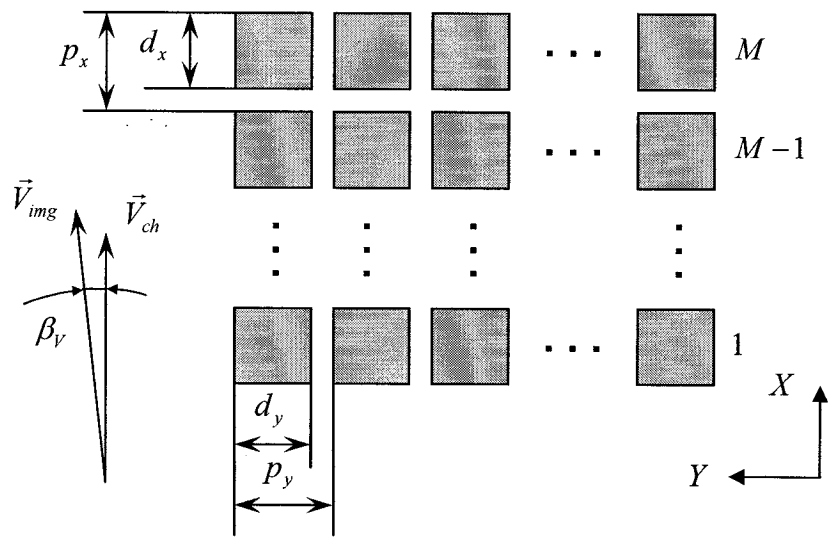

Figure 4.6. Layout of CCD elements.

MTF of the charge integration. Let the Fourier-component of irradiance in a plane of image be:

$$h(x) = a \cdot [1 + b \cdot \cos(2\pi f_u x)]. \tag{4.20}$$

After integration, the charge of one element will be proportional to the integral of (4.20):

$$d = \int_{x_e - \frac{1}{2}d_x}^{x_e + \frac{1}{2}d_x} a \cdot [1 + b \cdot \cos(2\pi f_u x)] dx = a \cdot d_x \left[1 + b \frac{\sin(\pi d_x f_u)}{\pi d_x f_u} \cos(2\pi f_u x_e) \right], \tag{4.21}$$

where x_e is an x-coordinate of the element center. Then the MTF in the x-direction is

$$MTF_{\text{int},x}(f_u) = \frac{\sin(\pi d_x f_u)}{\pi d_x f_u}. \tag{4.22}$$

Similarly, such a MTF in the y-direction will be determined by the value of d_y. Here $d_x \times d_y$ is a sensitivity region of a single element.

$$MTF_{\text{int},y}(f_v) = \frac{\sin(\pi d_y f_v)}{\pi d_y f_v}. \tag{4.23}$$

MTF of the discrete charge motion. This MTF is caused by the difference between the discrete type of the charge motion in the CCD and the constant velocity of the image motion on the photodetector surface. In time between two consecutive charge transfers, the image runs the distance $a = p_x / n_\varphi$, where p_x is a distance between the centers of elements in the x-direction, n_φ is a number of charge transfers per element. This motion causes blurring of image within the area of the size a, i.e.:[97]

$$MTF_{disc,x}(f_u) = \frac{\sin(\pi p_x f_u / n_\varphi)}{\pi p_x f_u / n_\varphi}. \tag{4.24}$$

MTF of the charge transfer inefficiency. At the consecutive transfer of the charge from one element to another, some part of the charge package remains in the first element and is not transferred to the next one. On the other hand, the charge transferred to the

next element mixes with the charge remained from the previous charge package. This effect causes degradation and phase shift of the signal charge packet. Their values are correspondingly equal:[98]

$$G_n(f_u) = \exp\{-M\varepsilon[1-\cos(2\pi p_x f_u)]\}, \tag{4.25}$$

$$\Delta\varphi_n(f_u) = M\varepsilon\sin(2\pi p_x f_u), \tag{4.26}$$

where M is the number of TDI lines, ε is a charge transfer inefficiency. The MTF due to the transfer inefficiency along the charge motion direction (x-direction) is[97]

$$MTF_{\varepsilon,x}(f_u) = \frac{1}{M(a^2+b^2)}(r^2+l^2)^{0.5}, \tag{4.27}$$

where:

$$a = \varepsilon[1-\cos(2\pi p_x f_u)], \tag{4.28}$$

$$b = \varepsilon\sin(2\pi p_x f_u), \tag{4.29}$$

$$r = a - \exp(-Ma)[a\cos(Mb) - b\sin(Mb)], \tag{4.30}$$

$$l = b - \exp(-Ma)[a\sin(Mb) + b\cos(Mb)]. \tag{4.31}$$

MTF of the charge diffusion. Supposing that carriers generated in result of a light action do not recombine inside the depletion region (the electric field pulls them out), and taking into account the carriers created outside the depletion region, and their wavelength and frequency dependence, the MTF of the charge diffusion is[98]

$$MTF_{diff}(f,\lambda) = \frac{1-\dfrac{\exp[-\alpha(\lambda)\cdot d_d]}{1+\alpha(\lambda)\cdot l}}{1-\dfrac{\exp[-\alpha(\lambda)\cdot d_d]}{1+\alpha(\lambda)\cdot L_d}}, \tag{4.32}$$

where:

$$\frac{1}{l^2} = \frac{1}{L_d^{\,2}} + (2\pi f)^2, \tag{4.33}$$

$\alpha(\lambda)$ is a spectral absorption coefficient of the CCD material

d_d is a junction depth

L_d is a diffusion length.

MTF of the velocities mismatch. Let the angle between the vectors of the image motion velocity $\vec{V}_{img}$ in the focal plane and the average velocity $\vec{V}_{ch}$ of the charge packets be equal to β_V (see Figure 4.6). Then, after M elements of accumulation, the charge packets will be displaced by the value a in the x-direction, and by the value b in the y-direction:

$$a = Mp_x\left(V_{img}\cos\beta_V - V_{ch}\right)/V_{ch}, \tag{4.34}$$

$$b = Mp_x V_{img}\sin\beta_V / V_{ch} \tag{4.35}$$

from the place where they should be at the ideal synchronization. This effect causing the degradation of the image is taken into account by the MTF of the speeds mismatch which, in the x-[97] and y-directions, equals respectively:

$$MTF_{\Delta\vec{V},x}(f_u) = \frac{\sin\left[\pi p_x M\left(\alpha_V\cos\beta_V - 1\right)f_u\right]}{\pi p_x M\left(\alpha_V\cos\beta_V - 1\right)f_u}, \tag{4.36}$$

$$MTF_{\Delta\vec{V},y}(f_v) = \frac{\sin\left[\pi p_x M\alpha_V\sin\beta_V f_v\right]}{\pi p_x M\alpha_V\sin\beta_V f_v}, \tag{4.37}$$

here $\alpha_V = V_{img}/V_{ch}$ is the parameter of synchronization of the velocities V_{img} and V_{ch}.

The image velocity modulus in the focal plane can be determined (for a circular orbit, and not taking Earth's rotation and the gravitational field perturbations into account) by

$$V_{img} = \frac{R_E \sqrt{G \cdot M_E}}{H \cdot (R_E + H)^{3/2}} F, \tag{4.38}$$

where R_E is Earth's radius, M_E is Earth's mass, G is the universal gravitational constant.

Total MTF. Let us define the total CCD MTF in the arbitrary θ_R-direction of the spatial resolution as

$$MTF_{CCD}(f, \lambda, \theta_R) = \sqrt{[MTF_{CCD,x}(f_u, \lambda) \cdot \cos\theta_R]^2 + [MTF_{CCD,y}(f_v, \lambda) \cdot \sin\theta_R]^2}, \tag{4.39}$$

where θ_R is the angle between the CCD x-direction (direction of the TDI) and the direction of resolution, the corresponding components $MTF_{CCD,x}(f_u, \lambda)$ and $MTF_{CCD,y}(f_v, \lambda)$ (without horizontal registers) of the CCD MTF in the x- and y-directions are

$$MTF_{CCD,x}(f_u, \lambda) =$$

$$= MTF_{\text{int},x}(f_u) \cdot MTF_{disc,x}(f_u) \cdot MTF_{\varepsilon,x}(f_u) \cdot MTF_{diff,x}(f_u, \lambda) \cdot MTF_{\Delta\vec{V},x}(f_u), \tag{4.40}$$

$$MTF_{CCD,y}(f_v, \lambda) = MTF_{\text{int},y}(f_v) \cdot MTF_{diff,y}(f_v, \lambda) \cdot MTF_{\Delta\vec{V},y}(f_v). \tag{4.41}$$

Signal

For the CCD, it is convenient to express the signal and noise values in the number of electrons corresponding to the irradiance on the photodetector surface. Not difficult to see that the average amounts of electrons from the image of the object, background, and atmospheric haze can be respectively written as (not taking a saturation charge value N_{sat} of the CCD TDI lines into account):

$$N_{ob}^{c}(f,\theta_R)=\frac{1}{hc}M\cdot T_{el}\cdot d_x\cdot d_y\int I_{ob}(f,\lambda)\cdot S_{ph}(\lambda)\cdot MTF_{CCD}(f,\lambda,\theta_R)\cdot\lambda\cdot d\lambda, \quad (4.42)$$

$$N_{bg}^{c}(f,\theta_R)=\frac{1}{hc}M\cdot T_{el}\cdot d_x\cdot d_y\int I_{bg}(f,\lambda)\cdot S_{ph}(\lambda)\cdot MTF_{CCD}(f,\lambda,\theta_R)\cdot\lambda\cdot d\lambda, \quad (4.43)$$

$$N_{h}^{c}=\frac{1}{hc}M\cdot T_{el}\cdot d_x\cdot d_y\int I_{h}(\lambda)\cdot S_{ph}(\lambda)\cdot\lambda\cdot d\lambda, \quad (4.44)$$

where

h is the Planck's constant

c is the light velocity

$T_{el}=\frac{d_x}{V_{img}}$ is the time of integration by one element

$S_{ph}(\lambda)$ is the spectral quantum efficiency of the photodetector.

Taking the saturation charge[99] into account, the corresponding numbers of electrons from the atmospheric haze, the image of the object and background are

$$N_h=\min\{N_h^c,\max\{0,N_{sat}-M\cdot T_{el}\cdot N_{dc}\}\}, \quad (4.45)$$

$$N_{ob}(f,\theta_R)=\min\{N_{ob}^{c}(f,\theta_R),\max\{0,N_{sat}-(N_h+M\cdot T_{el}\cdot N_{dc})\}\}, \quad (4.46)$$

$$N_{bg}(f,\theta_R)=\min\{N_{bg}^{c}(f,\theta_R),\max\{0,N_{sat}-(N_h+M\cdot T_{el}\cdot N_{dc})\}\}. \quad (4.47)$$

Hence, the total value of the signal expressed in electrons is

$$S_{tot}(f,\theta_R)=\left|N_{ob}(f,\theta_R)-N_{bg}(f,\theta_R)\right|. \quad (4.48)$$

Noise

At low levels of the object illumination, solid-state photodetectors are estimated by the value of the Noise Equivalent Signal (NES) which is equal to the density of the input energy providing the SNR equal to unit on an output of the photodetector. The basic

sources of the CCD noise applicable for our accounting are[97,98] radiation shot noise, and noise depending on a technical design and manufacturing processes (surface and bulk trapping noise, leakage current, non-uniformity of sensitivity, shift register, noise of the output amplifier, etc.). Expressing the total noise in terms of[100] photon shot noise, dark current shot noise of one pixel N_{dc}, and readout noise N_{ro}; and taking the Poisson distribution of the emission process of photoelectrons (photon noise) and dark current noise, the Gaussian distribution of the readout noise, and statistical independence of the noises into account, the total noise at the output of the TDI CCD (without horizontal registers) is

$$N_{tot}(\theta_R) = \sqrt{N_{ob}(0,\theta_R) + N_{bg}(0,\theta_R) + 2\left(N_h + M \cdot T_{el} \cdot N_{dc} + N_{ro}^2\right)}. \tag{4.49}$$

SNR

Then the SNR at the output of the photodetector is

$$SNR(R,\theta_R) = \frac{S_{tot}(f,\theta_R)}{N_{tot}(\theta_R)}. \tag{4.50}$$

Sample

The Fairchild Imaging CCD525 TDI line scan sensor with $M = 96$ lines of TDI was chosen as a photodetector because of its acceptable characteristics mentioned in the Data Sheet,[101] Table 4.2, and the spectral quantum efficiency kindly sent me by a manager of the Fairchild Imaging company, Figure 4.7.

Table 4.2. CCD's parameters.

Pixel size, $p_x \times p_y$	13μm ×13μm
Number of TDI lines, M	96, 64, 48, 32, 24
Vertical clock frequency, C_f	42 KHz
Number of vertical clocks, n_φ	3
Vertical charge transfer efficiency, $1-\varepsilon$	0.99995
Vertical saturation charge, N_{sat}	200 Ke-
Dark current, N_{dc}	10500 e-/pix/sec
Readout noise, N_{ro}	70 e-

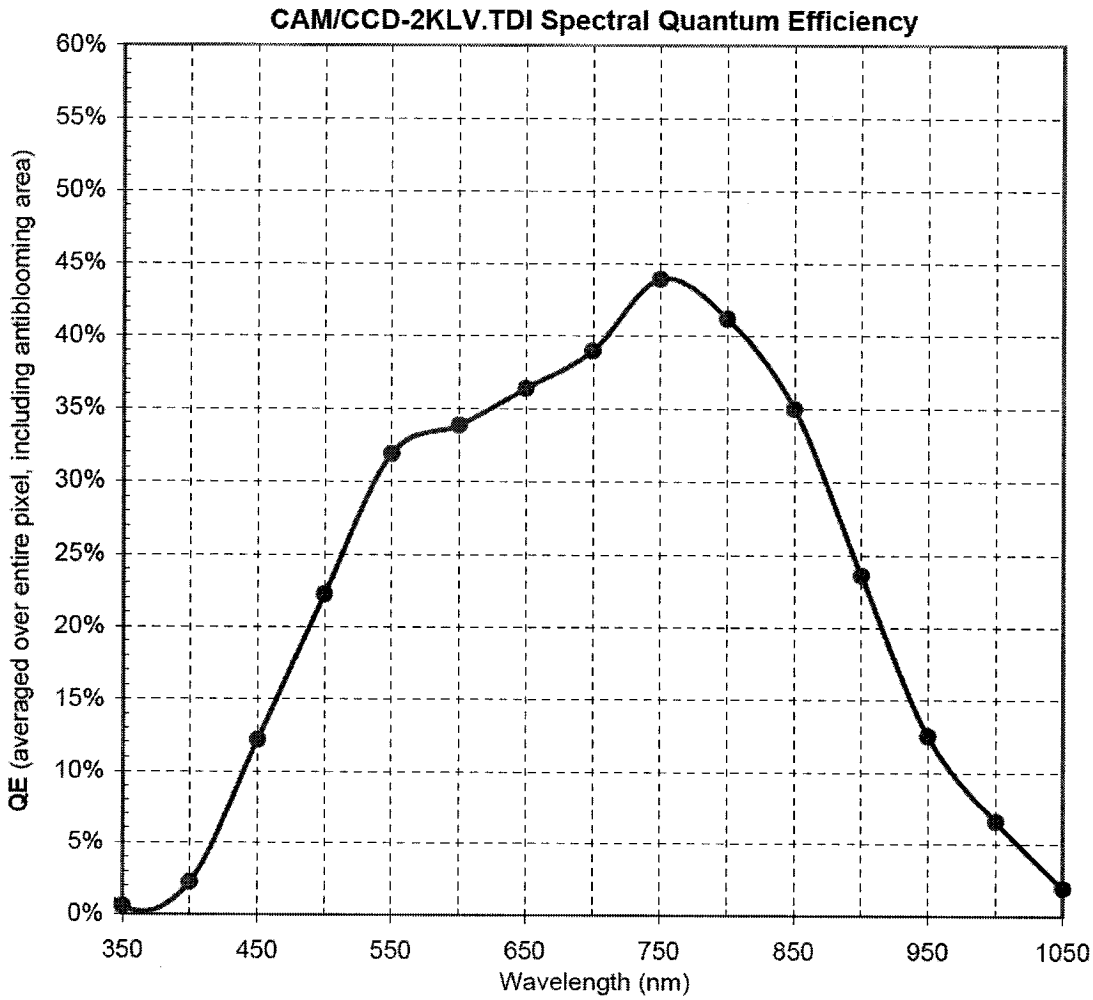

Figure 4.7. CCD's spectral quantum efficiency.

Point of the SNR evaluation

In design of the OES, the evaluation of the SNR or the spatial resolution of the system, or the system estimation is calculated on basis of quality of the image on a final visualizing device. However for our research, there is no necessity to carry out further transformations of the signal and noise; and we shall define another point of the system estimation. Let us define this point at the output of the CCD sensor. Such an approach seems convenient because, before this point, the various systems of the considered type have approximately the identical schematic device structures, and after this point, the systems can differ very considerably. Therefore, at the considered stage, there is no other opportunity to describe the transformation of the signal and noise values at the CCD output to the value of the perceived SNR except as

$$SNR_P = \mathfrak{I}\{SNR(R,\theta_R)\}, \tag{4.51}$$

where the transforming function $\mathfrak{I}\{.\}$ is determined by specific features of the actual space-based observation system, the receiver of the video information from the OES, the signal processing, methods of presenting the image to the observer, etc. As follows from the above-said, knowing the SNR at the output of the CCD and the structure of the whole imaging complex, it is possible to calculate the probability of the visual perception (and the NIIRS) of information from any ending document or device. Thus, we can evaluate the SNR at the output of the CCD sensor.

4.2. Problems of optimization

Let us define the objective function in the following general form:

$$J(R,\Omega_R)=\int_{\Omega_R}\Im\{SNR(R,\theta_R)\}d\theta_R\,, \tag{4.52}$$

where R is the prescribed value of the earth surface spatial resolution, Ω_R is some domain of the resolution directions θ_R of interest on the earth surface with respect to the x-direction of the CCD (Figure 4.8), $\Im\{SNR(R,\theta_R)\}$ is some transform of the SNR.

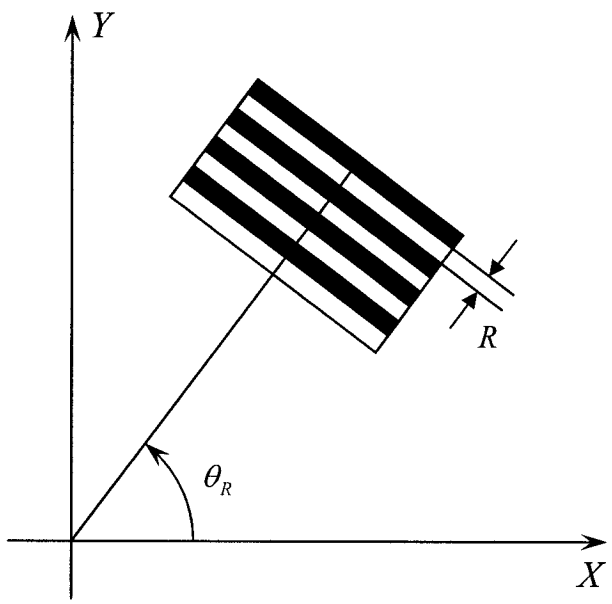

Figure 4.8. θ_R-direction of resolution.

If we are interested in the information on a set S_R of the spatial resolutions, the objective function can be written as

$$J(S_R,\Omega_R)=\int_{S_R}\int_{\Omega_R}\Im\{SNR(R,\theta_R)\}d\theta_R dR\,. \tag{4.53}$$

The considered problem of the parametric optimization of the space-based OES with a distributed aperture is to find magnitudes of varied parameters of the OS and the CCD at the prescribed characteristics of:

- light irradiance on the earth surface
- observation objects and background
- atmosphere
- orbit and dynamics of the satellites
- aperture
- beam combiner
- photodetector
- transformation of the electronic SNR to the perceived one
- probability of detection / recognition / identification.

Since the main emphasis in the given research is done on the systems with distributed apertures, the main varied parameters are ones determining:

- aperture configuration
- effective focal length
- geometrical sizes of a CCD pixel
- number of CCD TDI lines.

Depending on the criterion of optimization, optimized parameters, and constraints, we shall consider three optimization problems taking place in an engineering design of the space-based OESs.

4.2.1. Problem 1 – Optimization of the OS: the aperture configuration and the effective focal length

For an aperture consisting of N annular subapertures, the problem is to find the values of the subaperture center coordinates (u_n^0, v_n^0), inner and outer subaperture radii r_{1n} and r_{2n}, and the effective focal length F of the OS to provide the minimum of the function (4.52) subject to the following:

$$g_n \equiv R_A - \left(\sqrt{(u_n^0)^2 + (v_n^0)^2} + r_{2n} \right) \geq 0, \qquad n = 1, \ldots, N, \tag{4.54}$$

$$g_{nm} \equiv (u_n^0 - u_m^0)^2 + (v_n^0 - v_m^0)^2 - (r_{2n} + r_{2m})^2 \geq 0, \quad n = 1, \ldots, N\text{–}1, m = n\text{+}1, \ldots, N; \tag{4.55}$$

$$-R_A \leq u_n^0 \leq R_A, \qquad n = 1, \ldots, N, \tag{4.56}$$

$$-R_A \leq v_n^0 \leq R_A, \qquad n = 1, \ldots, N, \tag{4.57}$$

$$R_{11} \leq r_{1n} \leq R_{12}, \qquad n = 1, \ldots, N, \tag{4.58}$$

$$R_{21} \leq r_{2n} \leq R_{22}, \qquad n = 1, \ldots, N; \tag{4.59}$$

$$F_1 \leq F \leq F_2. \tag{4.60}$$

The bounds F_1 and F_2 are the minimal and maximal possible focal length values:

$$F_1 = H \cdot \max\{p_x, p_y\} / (K_{Nq} \cdot R), \tag{4.61}$$

$$F_2 = C_f \frac{p_x}{\cos \beta_V} \frac{H \cdot (R_E + H)^{3/2}}{R_E \sqrt{G \cdot M_E}}. \tag{4.62}$$

The value of F_1 is determined by the fact that the operating spatial frequency

$$f_R = H / (F \cdot 2R) \tag{4.63}$$

in the focal plane must not be greater than the minimal spatial Nyquist frequency

$$f_{Nq} = \min\{1/(2p_x), 1/(2p_y)\} \tag{4.64}$$

with the desirable coefficient K_{Nq} specifying the relationship between f_R and f_{Nq}:

$$K_{Nq} = f_R / f_{Nq}. \tag{4.65}$$

The constant C_f is the maximal vertical (along the x-axis) clock frequency of the CCD (see Table 4.2). The value of F_2 is defined from the obvious inequality:

$$C_f \geq \frac{V_{img} \cos \beta_V}{p_x}, \tag{4.66}$$

where V_{img} is determined by Ex. (4.38).

4.2.2. Problem 2 – Optimization of the CCD: the pixel sizes and the number of TDI lines

Let us suppose that we have the prescribed aperture configuration and value of the effective focal length, and we want to calculate the optimal sizes of a CCD pixel and the number of TDI lines. In such a formulation, the problem is to find the values of p_x, p_y, d_x, d_y, and M to provide the minimum of the function (4.52) subject to the following:

$$0 < \pi p_x M(\alpha_V \cos \beta_V - 1) f_u < \pi, \tag{4.67}$$

$$0 < \pi p_x M \alpha_V \sin \beta_V f_v < \pi; \tag{4.68}$$

$$H \cdot \max\{p_x, p_y\} / (K_{Nq} \cdot R) \leq F, \tag{4.69}$$

$$C_f \frac{p_x}{\cos \beta_V} \frac{H \cdot (R_E + H)^{3/2}}{R_E \sqrt{G \cdot M_E}} \geq F; \tag{4.70}$$

$$p_{x1} \leq p_x \leq p_{x2}, \tag{4.71}$$

$$p_{y1} \leq p_y \leq p_{y2}, \tag{4.72}$$

$$d_{x1} \le d_x \le d_{x2}, \tag{4.73}$$

$$d_{y1} \le d_y \le d_{y2}, \tag{4.74}$$

$$M_1 \le M \le M_2. \tag{4.75}$$

Here Exs. (4.67) and (4.68) determine the fact that the arguments of the sinc-functions (4.36) and (4.37) must be inside $(0,\pi)$-interval. Exs. (4.69) and (4.70) are determined by the formulas (4.61) and (4.62) correspondingly. The parameters p_{x1}, p_{x2}, p_{y1}, p_{y2}, d_{x1}, d_{x2}, d_{y1}, d_{y2} are corresponding bounds.

4.2.3. Problem 3 – Joint optimization of the OS and the CCD

Now we shall formulate a more general optimization problem jointing Problem 1 and 2: to find the values of the subaperture center coordinates (u_n^0, v_n^0), inner and outer subaperture radii r_{1n} and r_{2n}, the effective focal length F of the OS, the geometrical sizes p_x, p_y, d_x, d_y of a CCD pixel, and the number M of TDI lines to provide the minimum of the function (4.52) subject to the constrain functions and domains of parameters defined in Problems 1 and 2.

4.3. Numerical results

The optimization problems were solved with the help of the IMSL® DNCONG routine solving a general nonlinear programming problem using the successive quadratic programming algorithm and a user-supplied gradient. The results are shown in the figures and tables below.

It is known that today DigitalGlobe's (Longmont, CO) QuickBird-2[102] is a spacecraft able to offer the highest resolution imagery available commercially with 0.61 meter at nadir, H = 450 km. It is also known that DigitalGlobe plans to launch WorldView-1[103], a successor of QuickBird-2, in 2006. This satellite will provide the commercial imagery with 50-centimeter panchromatic resolution, H = 800 km. For these reasons, we would like to use the magnitude of the spatial resolution equal to 0.5 m for calculation. In accordance with Table 4.1, this resolution corresponds to the probabilities of a correct decision with respect to the objects having the minimal size shown in Table 4.3.

Table 4.3. Minimal object sizes corresponding to the probabilities of the correct decision for R = 0.5 m (from the Johnson's criteria, Table 4.1).

Performance level of vision	Minimal size, m
Detection	1.0
Orientation	1.4
Recognition	4.0
Identification	6.4

Some parameters for the calculation are as follow:

1) object related:

- $R = 0.5$ m

2) OS related:

- $R_A = 1.0$ m
- $R_{11} = 0.055$ m, $R_{12} = 0.075$ m
- $R_{21} = 0.1$ m, $R_{22} = 0.13$ m
- $\tau_n(\lambda) \equiv 1.0$
- $\eta = 500$
- $L_n = 1.0$ m

3) satellite – CCD related:

- $\alpha_V = 1.01$
- $\beta_V = 0.2°$

4) CCD related:

- $M = 96$
- $K_{Nq} = 0.75$

We used the objective function in the form of (4.52), changing the integration by the summation:

$$J(R,\Omega_R) = \frac{1}{N_R - 1}\sum_{j=1}^{N_R}\left[SNR_{Th} - SNR\left(R,(j-1)\cdot\frac{180°}{N_R}\right)\right]^2 \tag{4.76}$$

for

$$\begin{cases} N_R = 18, \\ \Omega_R = \left\{ \theta_R : \ \theta_R = (j-1) \cdot \dfrac{180°}{N_R}, \ \ j = 1,..., N_R \right\}; \end{cases} \tag{4.77}$$

and

$$J(R, \Omega_R) = [SNR_{Th} - SNR(R, \theta_R)]^2 \tag{4.78}$$

for

$$\begin{cases} N_R = 1, \\ \Omega_R = \{\theta_R : \ \theta_R = 0°\} \end{cases} \tag{4.79}$$

and

$$\begin{cases} N_R = 1, \\ \Omega_R = \{\theta_R : \ \theta_R = 90°\}. \end{cases} \tag{4.80}$$

The threshold values SNR_{Th} of the SNR were defined by reasons of the desirable inequality:

$$SNR_{Th} > \max_{\theta_R \in \Omega_R} \{SNR(R, \theta_R)\}, \tag{4.81}$$

and were in the range of 5.0 – 13.0. The objective functions have a form of variance of the SNR around the threshold at a given value of the ground resolution within some domain of the resolution directions of interest.

We used two arbitrarily taken initial aperture configurations shown in Figure 4.9: with two (a) and three (b) annular subapertures.

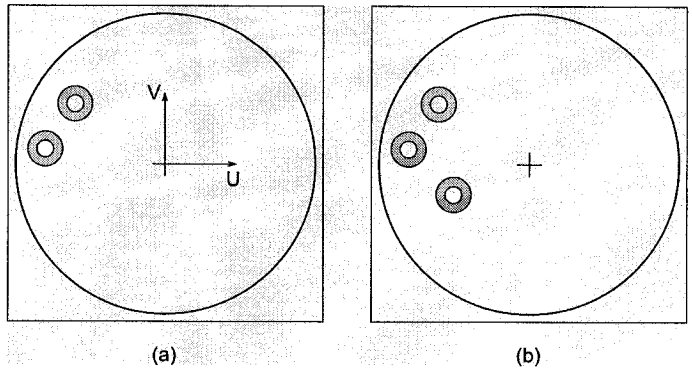

Figure 4.9. Initial aperture configurations.

The spectral range 0.4 – 1.05 μm was used for each object. Besides, the spectral subrange 0.75 – 1.05 μm for Object 1, and the spectral subrange 0.40 – 0.70 μm for Object 2 were used.

For the figures of optimal configurations, the parts denoted by (a) and (c) present the configurations for zero values of the IA (almost zero: $\sigma_{x_n} = \sigma_{y_n} = 0.001 \cdot 0.8$ μm), and zero values of the OPD errors; the parts denoted by (b) and (d) – the configurations for the IA errors $\bar{x}_n = \bar{y}_n = 0.0$, $\rho_{x_n y_n} = 0.0$, and the angle deviations of the beam tilts of 0.07" in the x- and y-directions which correspond to $\sigma_{x_n} = \sigma_{y_n} = 6 \cdot 0.8$ μm for F = 13.867 m; and the OPD errors $\bar{\Delta}_n = 0.0$, and $\sigma_{\Delta_n} = 0.1 \cdot 0.8$ μm for all n. The tables followed by the figures show the optimal parameters corresponding to the figures.

The following units for the parameters were used in all the tables below:

- spectral range – [μm]
- aperture parameters, u_n, v_n, r_{1n}, r_{2n}, s_{12}, s_{13}, s_{23} – [m]
- effective focal length, F – [m]

- CCD pixel sizes, p_x, p_y – [μm]
- altitude, H – [km].

4.3.1. Results for problem 1

Two annular subapertures

The aperture consists of two annular subapertures, Figure 4.9(a). The objective function is defined by Ex. (4.78). The altitude of observation H = 400 km. The optimal configurations are shown in Figures 4.10 – 4.13: (a) and (b) – for Ω_R (4.79), and (c) and (d) – for Ω_R (4.80). In the tables: s_{12} is the distance between the subaperture centers, the column "Probability" is the probability of the correct decision calculated in accordance with the formula (4.2).

1. Object 1.

A. The spectral range is 0.40 – 1.05 μm.

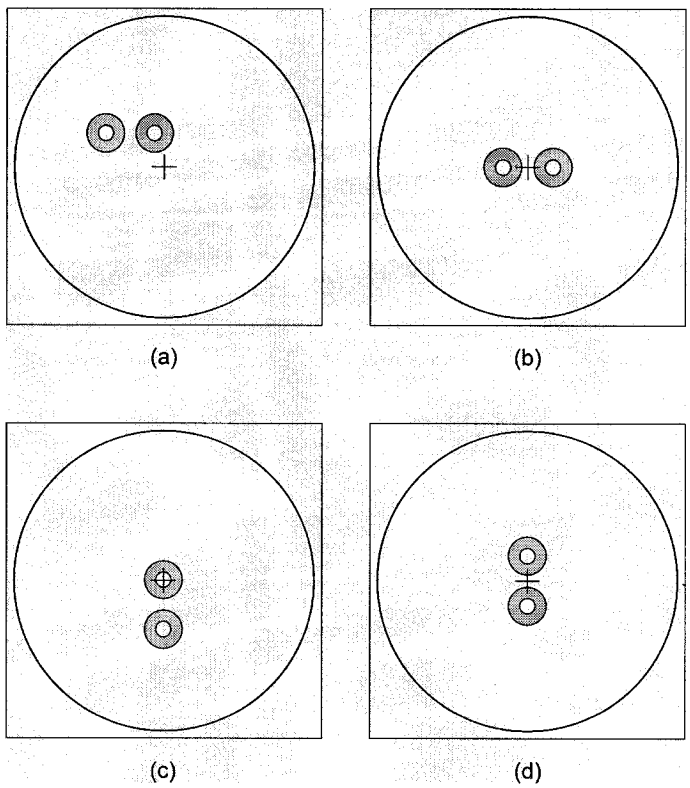

Figure 4.10. Optimal aperture configurations for Object 1, spectral range: 0.40 – 1.05 μm.

B. The spectral range is 0.75 – 1.05 μm.

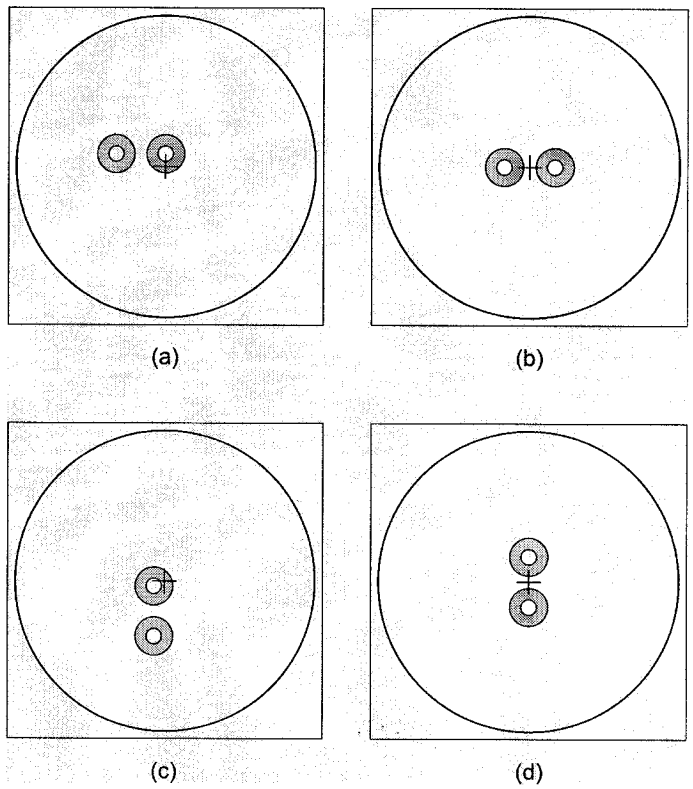

Figure 4.11. Optimal aperture configurations for Object 1, spectral range: 0.75 – 1.05 μm.

Table 4.4. Optimal parameters for Figure 4.10: Object 1, spectral range: 0.40 – 1.05 μm.

Figure 4.10	u_n	v_n	r_{1n}	r_{2n}	F	s_{12}	SNR	Probability
(a)	-0.392	0.221	0.055	0.130	13.867	0.328	7.26	1.0000
	-0.065	0.221	0.055	0.130				
(b)	-0.166	0.000	0.055	0.130	13.867	0.333	4.62	0.9223
	0.166	0.000	0.055	0.130				
(c)	-0.001	0.005	0.055	0.130	13.867	0.328	9.11	1.0000
	-0.001	-0.323	0.055	0.130				
(d)	0.000	0.166	0.055	0.130	13.867	0.333	5.79	0.9952
	0.000	-0.166	0.055	0.130				

Table 4.5. Optimal parameters for Figure 4.11: Object 1, spectral range: 0.75 – 1.05 μm.

Figure 4.11	u_n	v_n	r_{1n}	r_{2n}	F	s_{12}	SNR	Probability
(a)	-0.330	0.084	0.055	0.130	13.867	0.331	8.52	1.0000
	0.001	0.084	0.055	0.130				
(b)	-0.167	0.000	0.055	0.130	13.867	0.333	5.49	0.9888
	0.166	0.000	0.055	0.130				
(c)	-0.069	-0.033	0.055	0.130	13.867	0.331	10.68	1.0000
	-0.069	-0.364	0.055	0.130				
(d)	0.000	0.166	0.055	0.130	13.867	0.333	6.88	0.9999
	0.000	-0.167	0.055	0.130				

2. Object 2.

A. The spectral range is 0.40 – 1.05 μm.

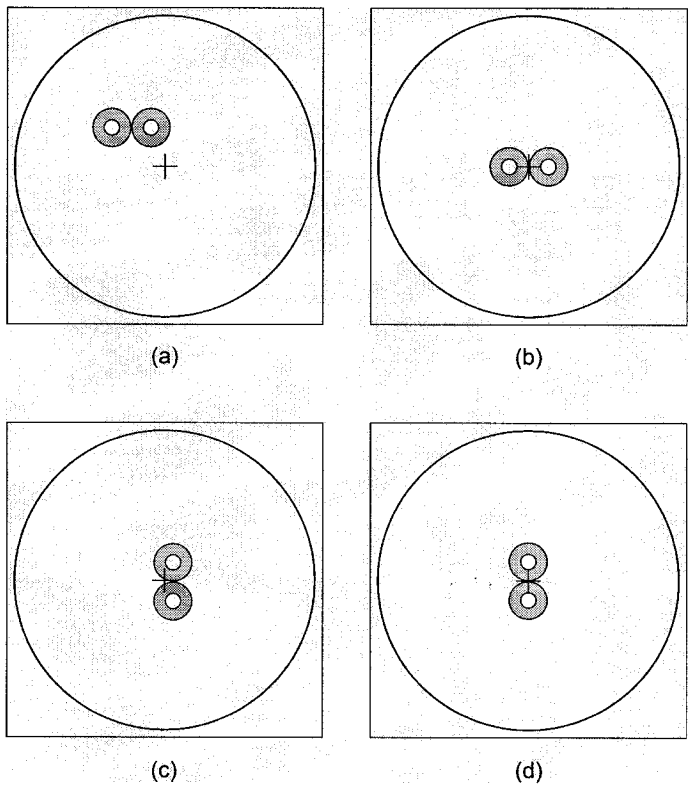

Figure 4.12. Optimal aperture configurations for Object 2, spectral range: 0.40 – 1.05 μm.

B. The spectral range is 0.40 – 0.70 μm.

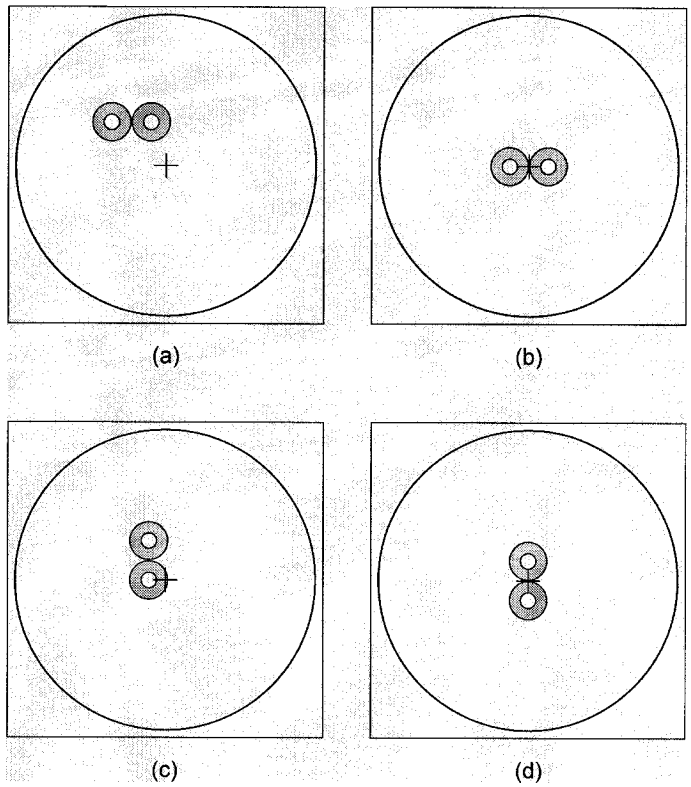

Figure 4.13. Optimal aperture configurations for Object 2, spectral range: 0.40 – 0.70 μm.

Table 4.6. Optimal parameters for Figure 4.12: Object 2, spectral range: 0.40 – 1.05 μm.

Figure 4.12	u_n	v_n	r_{1n}	r_{2n}	F	s_{12}	SNR	Probability
(a)	-0.354	0.255	0.055	0.130	13.867	0.260	7.04	0.9999
	-0.094	0.255	0.055	0.130				
(b)	-0.130	0.000	0.055	0.130	13.867	0.260	3.18	0.4934
	0.130	0.000	0.055	0.130				
(c)	0.057	0.121	0.055	0.130	13.867	0.260	8.83	1.0000
	0.057	-0.139	0.055	0.130				
(d)	0.000	0.130	0.055	0.130	13.867	0.260	3.99	0.7865
	0.000	-0.130	0.055	0.130				

Table 4.7. Optimal parameters for Figure 4.13: Object 2, spectral range: 0.40 – 0.70 μm.

Figure 4.13	u_n	v_n	r_{1n}	r_{2n}	F	s_{12}	SNR	Probability
(a)	-0.360	0.289	0.055	0.130	13.867	0.260	9.33	1.0000
	-0.100	0.289	0.055	0.130				
(b)	-0.130	0.000	0.055	0.130	13.867	0.260	4.28	0.8594
	0.130	0.000	0.055	0.130				
(c)	-0.110	0.260	0.055	0.130	13.867	0.260	11.70	1.0000
	-0.110	0.000	0.055	0.130				
(d)	0.000	0.130	0.055	0.130	13.867	0.260	5.36	0.9847
	0.000	-0.130	0.055	0.130				

These results show that the optimal aperture configuration depends on the observed object. The value of the SNR in the y-direction is greater than in the x-direction, i.e. the MTF of the CCD has different values in x- and y-directions. Some dependence of the distance s_{12} between the subaperture centers on the values of the IA and OPD errors – the greater errors, the greater distance – can be explained by more influence of the errors in a shorter wavelength spectrum. Besides, the subaperture configurations with non-zero IA and OPD errors tend to the aperture center – in accordance with Figure 3.5 showing a greater optical MTF decrease as subaperures are located far away from the aperture center. It is also seen that the SNR can be increased by corresponding spectral filtration of the incoming radiation.

The calculated optimal focal length of 13.867 m equals the minimal possible value F_1 specified by Ex. (4.61).

Three annular subapertures

The aperture consists of three annular subapertures, Figure 4.9(b). The objective function is defined by Ex. (4.76); and N_R and Ω_R – by Ex. (4.77). The results are calculated for two altitudes: 400 and 600 km. The values $SNR_{\min} = \min\limits_{\theta_R \in \Omega_R} \{SNR(R, \theta_R)\}$ and $SNR_{\max} = \max\limits_{\theta_R \in \Omega_R} \{SNR(R, \theta_R)\}$ are the minimal and maximal values of the SNR over the domain Ω_R of the resolution directions θ_R. The corresponding minimal and maximal probabilities $P_{\min} = P_D(SNR_{\min})$ and $P_{\max} = P_D(SNR_{\max})$ of the correct decision are the functions of the SNR, which calculated in accordance with the formula (4.2). The

parameters s_{12}, s_{13}, s_{23} are the distances between the centers of the corresponding subapertures: 1 – 2, 1 – 3, and 2 – 3.

I. The altitude H = 400 km.

1. Object 1.

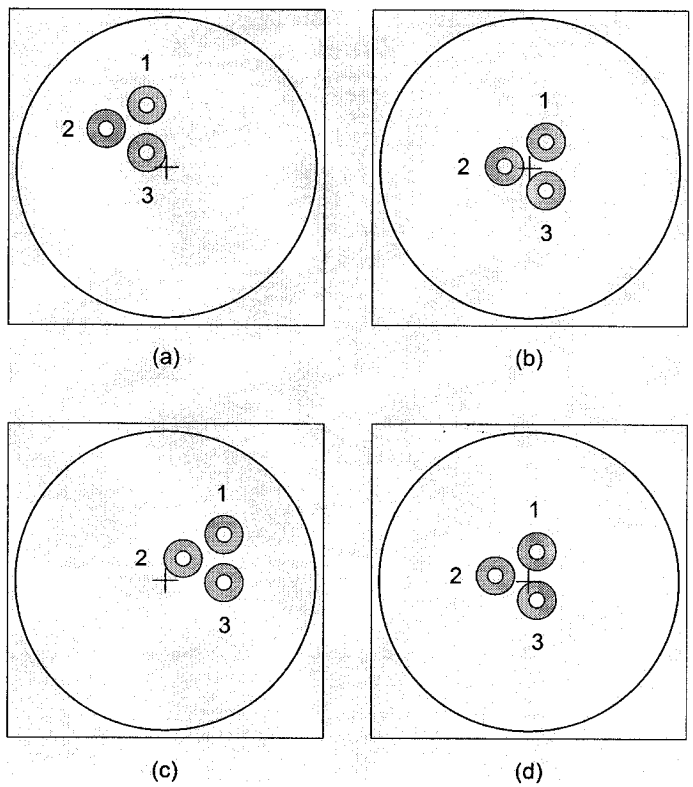

Figure 4.14. Optimal aperture configurations for H = 400 km, Object 1, spectral range: (a) (b) 0.40 – 1.05 μm, (c) (d) 0.75 – 1.05 μm.

Table 4.8. Optimal parameters for Figure 4.14: $H = 400$ km, Object 1.

Spectral range	Figure 4.14	n	u_n	v_n	r_{1n}	r_{2n}	F
0.40 – 1.05	(a)	1	-0.133	0.413	0.055	0.130	13.867
		2	-0.401	0.254	0.055	0.130	
		3	-0.132	0.096	0.055	0.130	
	(b)	1	0.108	0.175	0.055	0.130	13.867
		2	-0.165	0.013	0.055	0.130	
		3	0.108	-0.149	0.055	0.130	
0.75 – 1.05	(c)	1	0.388	0.307	0.055	0.130	13.867
		2	0.117	0.147	0.055	0.130	
		3	0.389	-0.014	0.055	0.130	
	(d)	1	0.055	0.201	0.055	0.130	13.867
		2	-0.217	0.039	0.055	0.130	
		3	0.055	-0.123	0.055	0.130	

Table 4.9. Optimal characteristics for $H = 400$ km, object – Object 1.

Spectral range	Figure 4.14	s_{12}	s_{13}	s_{23}	$SNR_{\min}$	$SNR_{\max}$	$P_{\min}$	$P_{\max}$
0.40 – 1.05	(a)	0.312	0.317	0.312	3.30	8.04	0.5417	1.0000
	(b)	0.317	0.323	0.317	2.00	5.32	0.1144	0.9828
0.75 – 1.05	(c)	0.315	0.321	0.315	3.23	9.81	0.5139	1.0000
	(d)	0.317	0.324	0.317	2.07	6.34	0.1285	0.9992

2. Object 2.

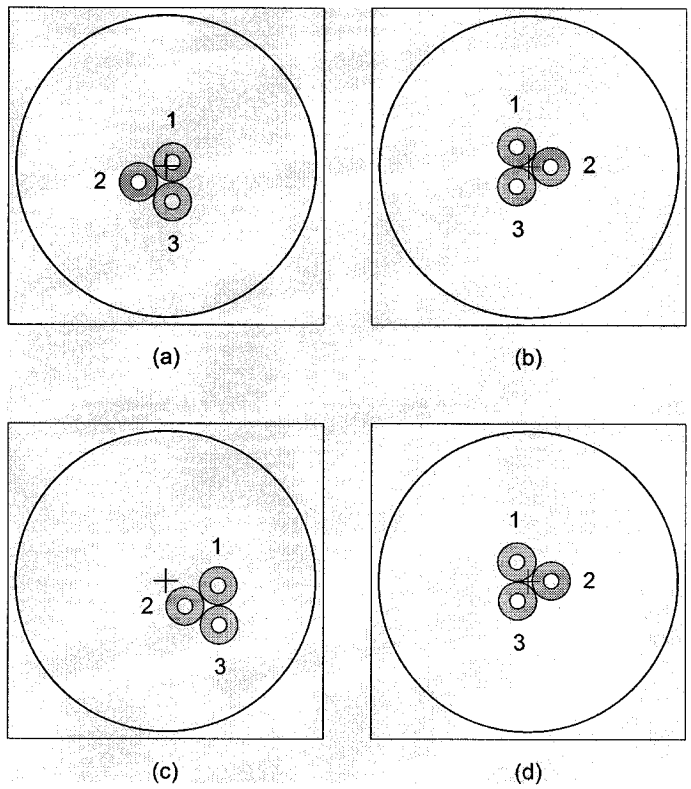

Figure 4.15. Optimal aperture configurations for H = 400 km, Object 2, spectral range: (a) (b) 0.40 – 1.05 μm, (c) (d) 0.40 – 0.70 μm.

Table 4.10. Optimal parameters for Figure 4.15: $H = 400$ km, Object 2.

Spectral range	Figure 4.15	n	u_n	v_n	r_{1n}	r_{2n}	F
0.40 – 1.05	(a)	1	0.040	0.025	0.055	0.130	13.867
		2	-0.185	-0.105	0.055	0.130	
		3	0.040	-0.235	0.055	0.130	
	(b)	1	-0.079	0.131	0.055	0.130	13.867
		2	0.146	0.001	0.055	0.130	
		3	-0.080	-0.129	0.055	0.130	
0.40 – 0.70	(c)	1	0.350	-0.033	0.055	0.130	13.867
		2	0.128	-0.169	0.055	0.130	
		3	0.357	-0.293	0.055	0.130	
	(d)	1	-0.073	0.130	0.055	0.130	13.867
		2	0.155	0.004	0.055	0.130	
		3	-0.068	-0.130	0.055	0.130	

Table 4.11. Optimal characteristics for $H = 400$ km, Object 2.

Spectral range	Figure 4.15	s_{12}	s_{13}	s_{23}	SNR_{min}	SNR_{max}	P_{min}	P_{max}
0.40 – 1.05	(a)	0.260	0.260	0.260	5.57	8.67	0.9911	1.0000
	(b)	0.260	0.260	0.260	2.65	4.04	0.2907	0.7989
0.40 – 0.70	(c)	0.260	0.260	0.260	7.63	11.65	1.0000	1.0000
	(d)	0.260	0.260	0.260	3.68	5.50	0.6837	0.9892

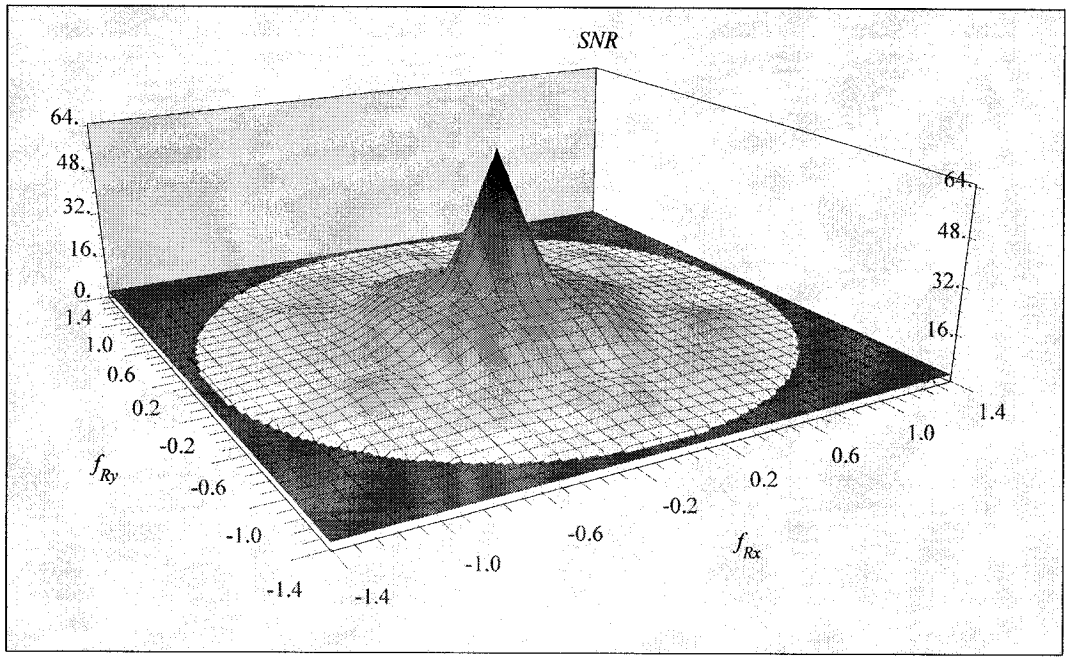

Figure 4.16. SNR versus f_{Rx} and f_{Ry} for the configuration of Figure 4.14(b): H = 400 km, Object 1, spectral range: 0.40 – 1.05 μm.

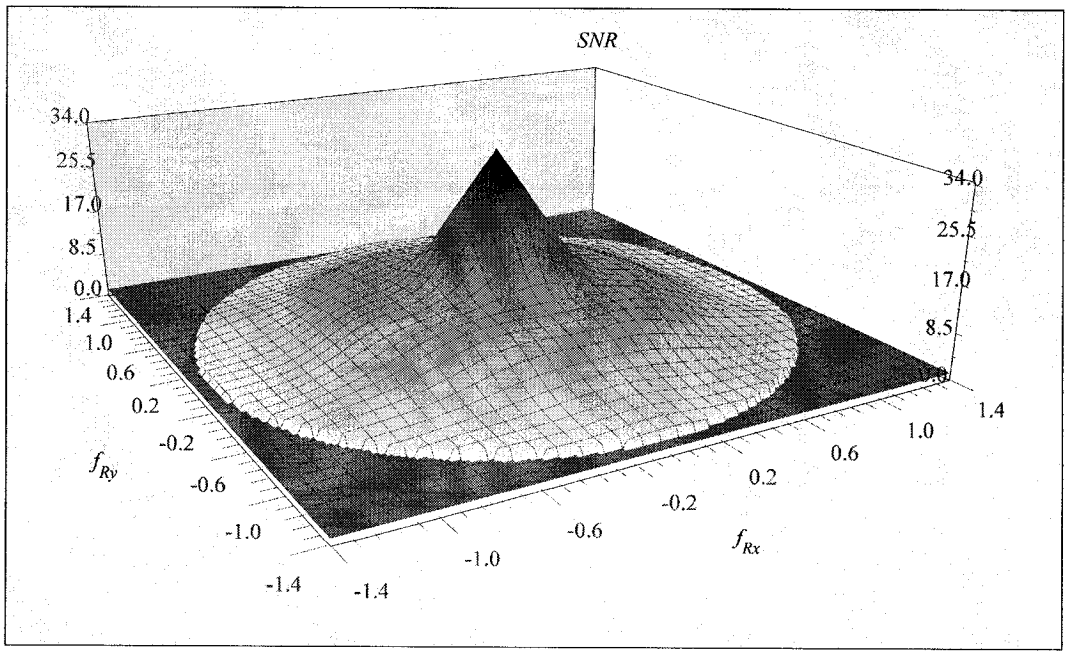

Figure 4.17. SNR versus f_{Rx} and f_{Ry} for the configuration of Figure 4.15(b): H = 400 km, Object 2, spectral range: 0.40 – 1.05 μm.

Figures (4.16) and (4.17) illustrate the 2-D behavior of the SNR-function versus the spatial frequencies $f_{Rx} = \cos\theta_R /(2R)$ and $f_{Ry} = \sin\theta_R /(2R)$ on the earth surface in the range bounded by the spatial Nyquist frequency. These graphics and their sections can be used for the preliminary estimations of the corresponding system spatial ground resolution.

It is also interesting to look at the 3-D graphics of the objective function (4.76). Figures 4.19 and 4.21 present such graphics calculated for three-subaperture configurations with the angle deviations of the beam tilts of 0.07" and $\sigma_{\Delta_n} = 0.1 \cdot 0.8$ μm for all the subapertures, H = 400 km, Object 1, spectral range: 0.40 – 1.05 μm. Figure 4.19 shows the dependence the objective function (4.76) on the effective focal length F and the distances d_c between the subaperture centers coincided with the vertices of the equilateral triangle at its rotation angle φ_A = 30.0°. Figure 4.18 shows graphically the variables d_c and φ_A.

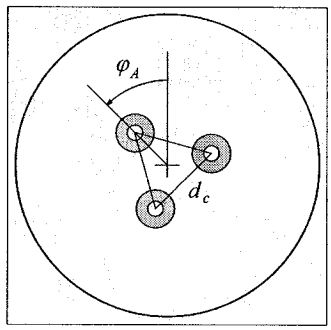

Figure 4.18. Variables for the 3-D graphics.

The inner and outer radii of the subapertures are correspondingly r_{1n} = 0.055 m and r_{2n} = 0.130 m. The subapertures "move" simultaneously from the closest possible distances d_c = 0.260 m between their centers to the distances d_c = 0.520 m along their rays

originating from the triangle center. The function has the single minimum corresponding to the minimal shown F = 13.0 m and d_c = 0.320 m.

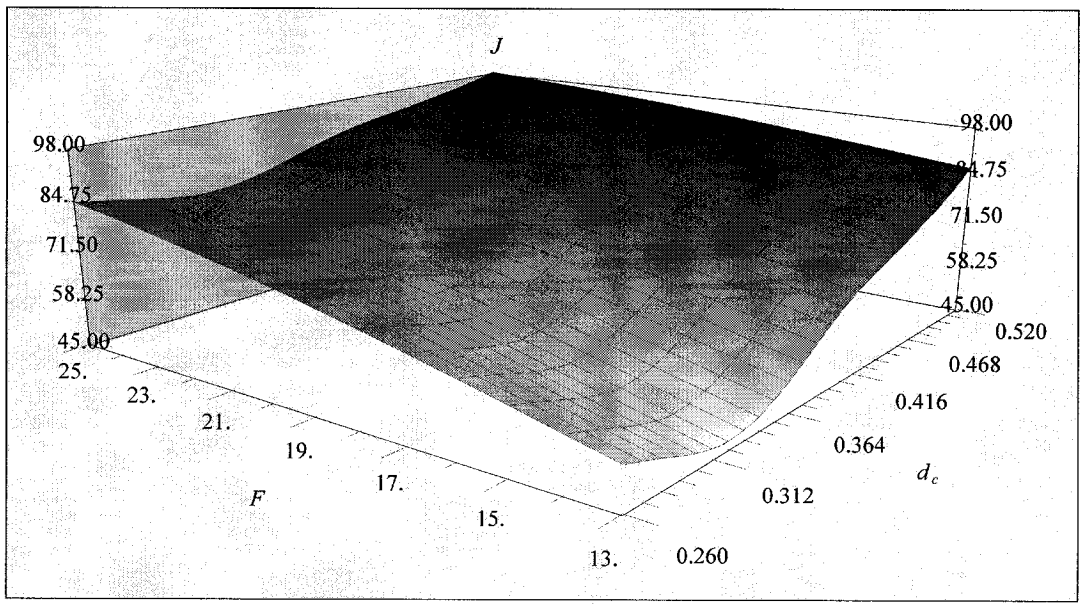

Figure 4.19. Dependence of the objective function (4.76) on F and d_c for H = 400 km, Object 1, spectral range: 0.40 – 1.05 μm, SNR_{Th} = 10.

The F- and d_c-sections of the objective function surface are shown in Figure 4.20: (a) F = 13.867 m, and (b) d_c = 0.320 m.

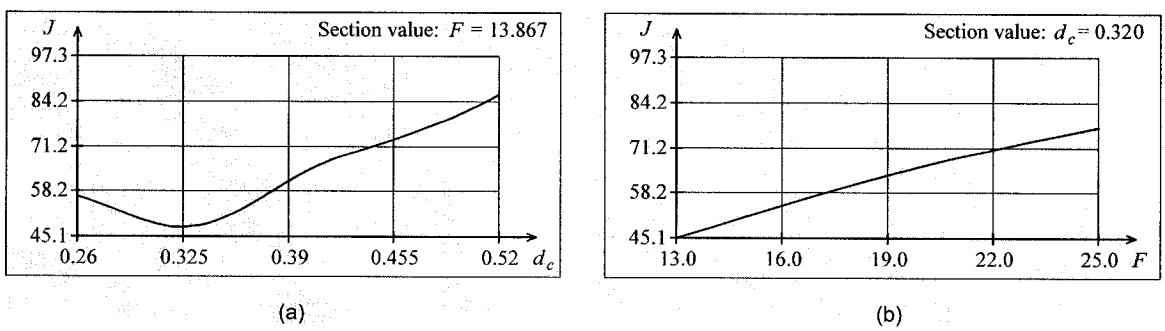

Figure 4.20. Section curves of the surface in Figure 4.19.

Figure 4.21 shows the dependence of the objective function (4.76) on the rotation angle φ_A varying from 0° to 120°, and the distances d_c between the subapertures like in Figure 4.19, at F = 13.867 m. The function has two equal minimum corresponding to φ_A = 30.0° and 90.0°, and d_c = 0.320 m.

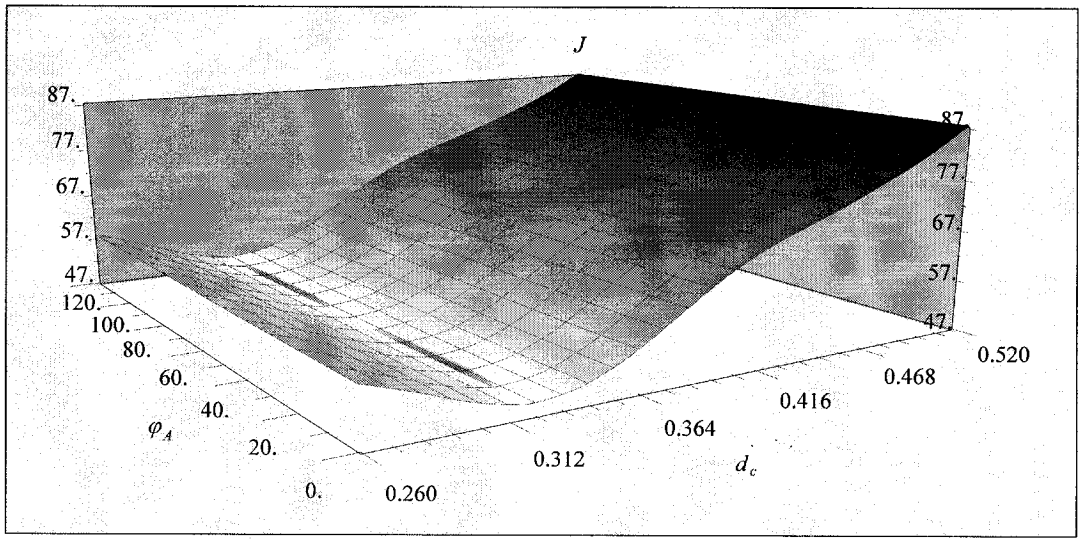

Figure 4.21. Dependence of the objective function (4.76) on φ_A and d_c for H = 400 km, Object 1, spectral range: 0.40 – 1.05 μm, SNR_{Th} = 10.

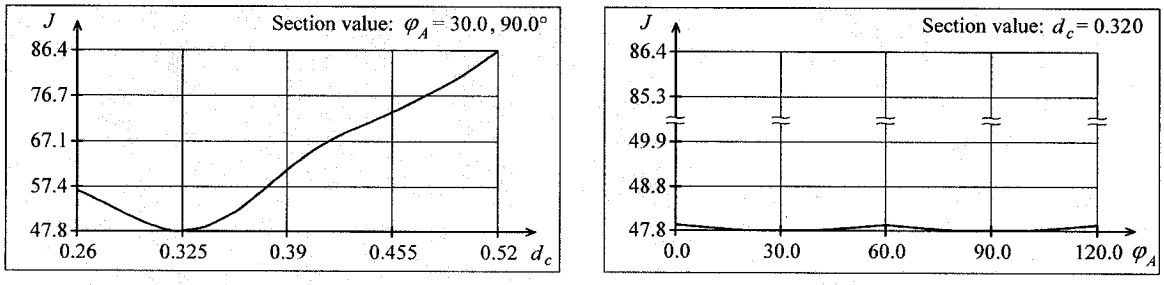

Figure 4.22. Section curves of the surface in Figure 4.21.

The φ_A- and d_c-sections of the objective function surface are shown in Figure 4.22: (a) φ_A = 30.0° and 90.0°, and (b) d_c = 0.320 m. The sections for φ_A = 30.0° and 90.0° are the same.

Returning to the optimal configurations, Figures 4.14 and 4.15, we see that the configurations in Figures 4.14, and 4.15 (a) and (c) correspond to φ_A = 90.0°, while the configurations in Figures 4.15 (b) and (d) – to φ_A = 30.0°. The existence of these preferable angles can be explained by a difference between the CCD MTF along the *x*- and *y*-axis. Naturally to expect that, if the CCD MTF did not depend on the direction, there would be not preferable φ_A, i.e. the optimal configuration would be determined by the subaperture distances only.

II. The altitude H = 600 km.

1. Object 1.

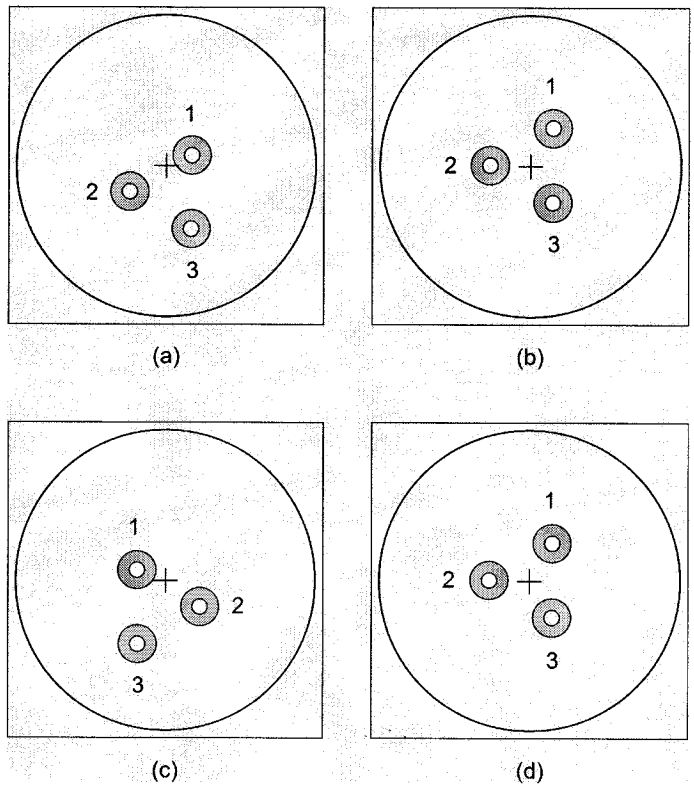

Figure 4.23. Optimal aperture configurations for H = 600 km, Object 1, spectral range: (a) (b) 0.40 – 1.05 μm, (c) (d) 0.75 – 1.05 μm.

Table 4.12. Optimal parameters for Figure 4.23: $H = 600$ km, Object 1.

Spectral range	Figure 4.23	n	u_n	v_n	r_{1n}	r_{2n}	F
0.40 – 1.05	(a)	1	0.169	0.069	0.055	0.130	20.8
		2	-0.243	-0.170	0.055	0.130	
		3	0.163	-0.416	0.055	0.130	
	(b)	1	0.149	0.252	0.055	0.130	20.8
		2	-0.267	0.007	0.055	0.130	
		3	0.147	-0.239	0.055	0.130	
0.75 – 1.05	(c)	1	-0.189	0.071	0.055	0.130	20.8
		2	0.226	-0.172	0.055	0.130	
		3	-0.186	-0.420	0.055	0.130	
	(d)	1	0.150	0.252	0.055	0.130	20.8
		2	-0.267	0.007	0.055	0.130	
		3	0.147	-0.241	0.055	0.130	

Table 4.13. Optimal characteristics for $H = 600$ km, Object 1.

Spectral range	Figure 4.23	s_{12}	s_{13}	s_{23}	$SNR_{\min}$	$SNR_{\max}$	$P_{\min}$	$P_{\max}$
0.40 – 1.05	(a)	0.476	0.485	0.475	0.02	4.69	0.0007	0.9321
	(b)	0.482	0.491	0.482	0.01	3.04	0.0007	0.4376
0.75 – 1.05	(c)	0.481	0.491	0.480	0.03	5.80	0.0008	0.9954
	(d)	0.483	0.493	0.482	0.02	3.72	0.0007	0.6988

2. Object 2.

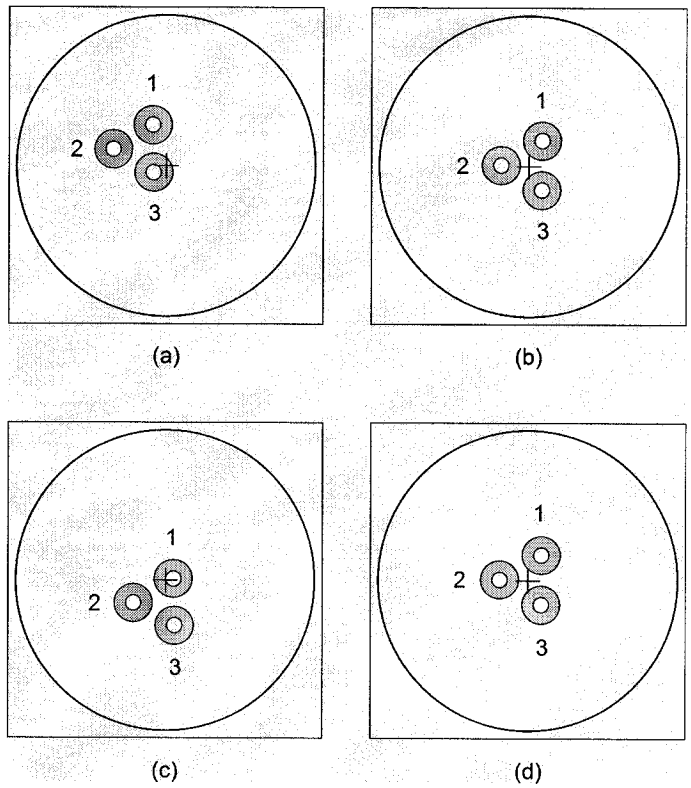

Figure 4.24. Optimal aperture configurations for H = 600 km, Object 2, spectral range: (a) (b) 0.40 – 1.05 μm, (c) (d) 0.40 – 0.70 μm.

Table 4.14. Optimal parameters for Figure 4.24: $H = 600$ km, Object 2.

Spectral range	Figure 4.24	N	u_n	v_n	r_{1n}	r_{2n}	F
0.40 – 1.05	(a)	1	-0.088	0.269	0.055	0.130	20.8
		2	-0.351	0.109	0.055	0.130	
		3	-0.084	-0.044	0.055	0.130	
	(b)	1	0.088	0.170	0.055	0.130	20.8
		2	-0.184	0.008	0.055	0.130	
		3	0.085	-0.157	0.055	0.130	
0.40 – 0.70	(c)	1	0.052	0.011	0.055	0.130	20.8
		2	-0.213	-0.150	0.055	0.130	
		3	0.059	-0.300	0.055	0.130	
	(d)	1	0.089	0.171	0.055	0.130	20.8
		2	-0.188	0.007	0.055	0.130	
		3	0.086	-0.160	0.055	0.130	

Table 4.15. Optimal characteristics for $H = 600$ km, Object 2.

Spectral range	Figure 4.24	s_{12}	s_{13}	s_{23}	$SNR_{\min}$	$SNR_{\max}$	$P_{\min}$	$P_{\max}$
0.40 – 1.05	(a)	0.307	0.313	0.308	1.57	3.92	0.0519	0.7644
	(b)	0.317	0.327	0.316	0.56	1.55	0.0042	0.0497
0.40 – 0.70	(c)	0.310	0.311	0.310	2.00	4.89	0.1160	0.9549
	(d)	0.321	0.331	0.321	0.72	2.04	0.0065	0.1223

Figures (4.25) and (4.26), like Figures (4.16) and (4.17), illustrate the 2-D behavior of the SNR-function versus the spatial frequencies f_{Rx} and f_{Ry}, and can be also used for the preliminary estimations of the corresponding system spatial ground resolution.

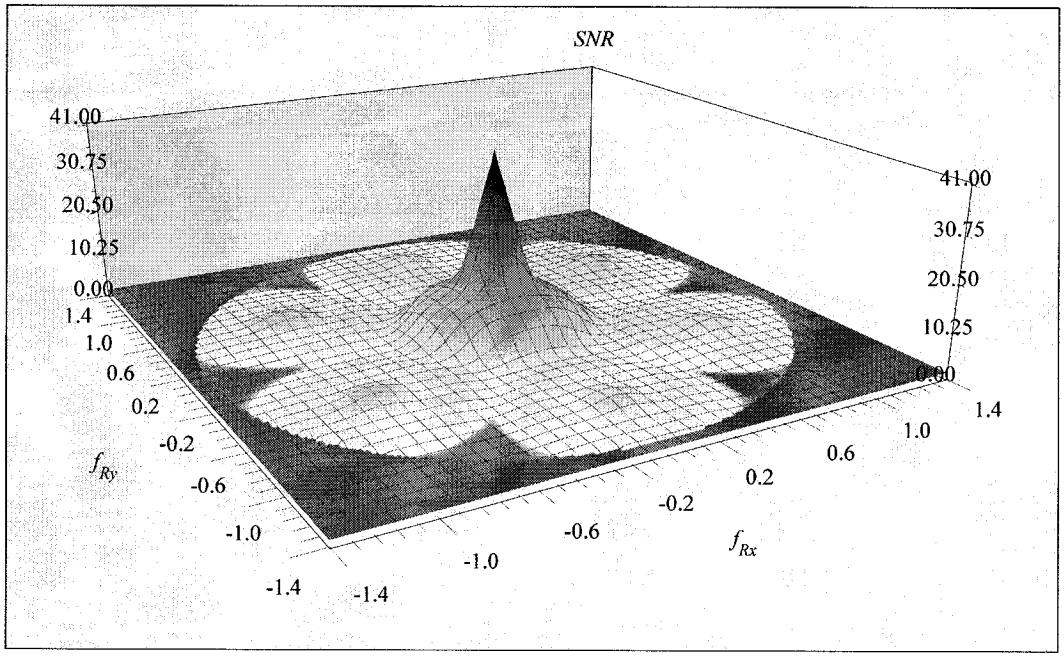

Figure 4.25. SNR versus f_{Rx} and f_{Ry} for the configuration of Figure 4.23(b): H = 600 km, Object 1, spectral range: 0.40 – 1.05 μm.

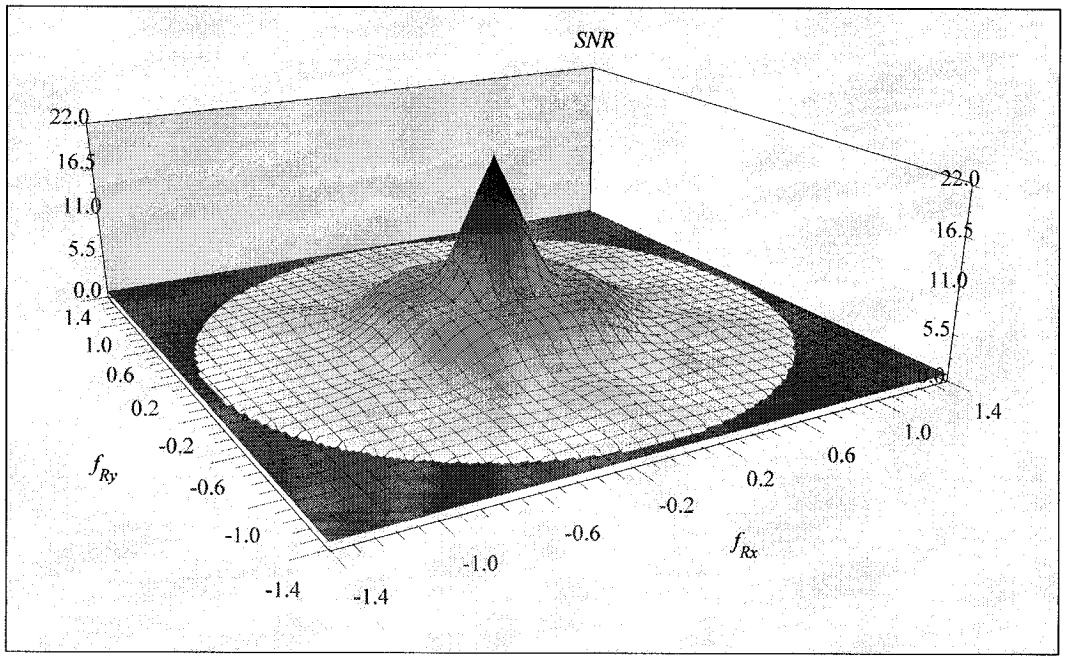

Figure 4.26. SNR versus f_{Rx} and f_{Ry} for the configuration of Figure 4.24(b): H = 600 km, Object 2, spectral range: 0.40 – 1.05 μm.

The maximal distances are between the first and third subapertures. As for two-subaperture configurations, we see small dependence of the subaperture distances on the IA and OPD errors. It is also obvious that the subapertures with the non-zero errors tend to the aperture center, which can be comprehended from Figure 3.5: the closer to the aperture center, the smaller the MTF decrease.

The calculated F = 13.867 m for H = 400 km, and F = 20.8 m for H = 600 km are equal to the minimal possible values F_1 specified by Ex. (4.61).

4.3.2. Results for problem 2

We have used the calculated optimal aperture configurations presented in Figures 4.14(b), 4.15(b), 4.23(b), and 4.24(b) with non-zero IA and OPD errors, and the corresponding values of the calculated optimal effective focal length. The spectral range is 0.40 – 1.05 μm. Besides, in addition to the constraints (4.67) – (4.70), the following equalities were used:

$$d_x = p_x \tag{4.82}$$

and

$$d_y = p_y . \tag{4.83}$$

The taken values of the bounds:

- $p_{x1} = p_{y1} = 1$ μm
- $p_{x2} = p_{y2} = 200$ μm
- $M_1 = 1$
- $M_2 = 2048$.

Table 4.16 shows characteristics of the OES with respect to the standard parameters of the CCD manufactured sample, and the calculated ones for Objects 1 and 2. The parameters p_x, p_y, and M in the first line for each object equal to ones of the manufactured sample, while the second lines contains the calculated optimal values. We see that the sizes of a pixel have not been changed, while the standard number of TDI lines, $M = 96$ is not an optimal magnitude with respect to the objective function (4.76) and for the given magnitudes of the considered OES parameters. The optimal value is 200 for the aperture configurations whose subapertures are not touched with each other.

Table 4.16. Characteristics of the OES with respect to the standard and calculated parameters of the CCD for Objects 1 and 2, SNR_{Th} = 13.0.

H F	Object	p_x	p_y	M	$J(R,\Omega_R)$	$SNR_{\min}$	$SNR_{\max}$	$P_{\min}$	$P_{\max}$
400 13.867	1	13.0	13.0	96	99.81	2.00	5.32	0.1144	0.9828
		13.0	13.0	200	88.30	1.36	6.87	0.0326	0.9999
	2	13.0	13.0	96	94.42	2.65	4.04	0.2907	0.7989
		13.0	13.0	181	83.69	1.87	5.37	0.0915	0.9849
600 20.8	1	13.0	13.0	96	148.95	0.01	3.04	0.0007	0.4376
		13.0	13.0	200	142.20	0.004	3.92	0.0007	0.7633
	2	13.0	13.0	96	153.69	0.56	1.55	0.0042	0.0497
		13.0	13.0	200	148.39	0.41	2.21	0.0026	0.1617

It is interesting to look at the 3-D graphics of the objective function versus the pixel sizes and the effective focal length, and versus the number of TDI lines and the effective focal length. Figures 4.27 and 4.28 show such dependences for the optimal aperture configuration presented in Figure 4.14(a) with zero-value IA and OPD errors, H = 400 km, and the spectral range of 0.40 – 1.05 μm for Object 1. The applicable domains of the objective function (non-flat surface for Figure 4.27, and $F \geq 10.4$ m for Figure 4.28) are determined by Ex. (4.61) at $K_{Nq} = 1$ and R = 0.5 m. Figure 4.27 uses M = 200. We see a practical straight dependence of the optimal focal length versus the pixel sizes for an optimal solution. Figure 4.28 uses $p_x = p_y = d_x = d_y$ = 13 μm. Such pictures stimulate a joint optimization of the OS and CCD parameters.

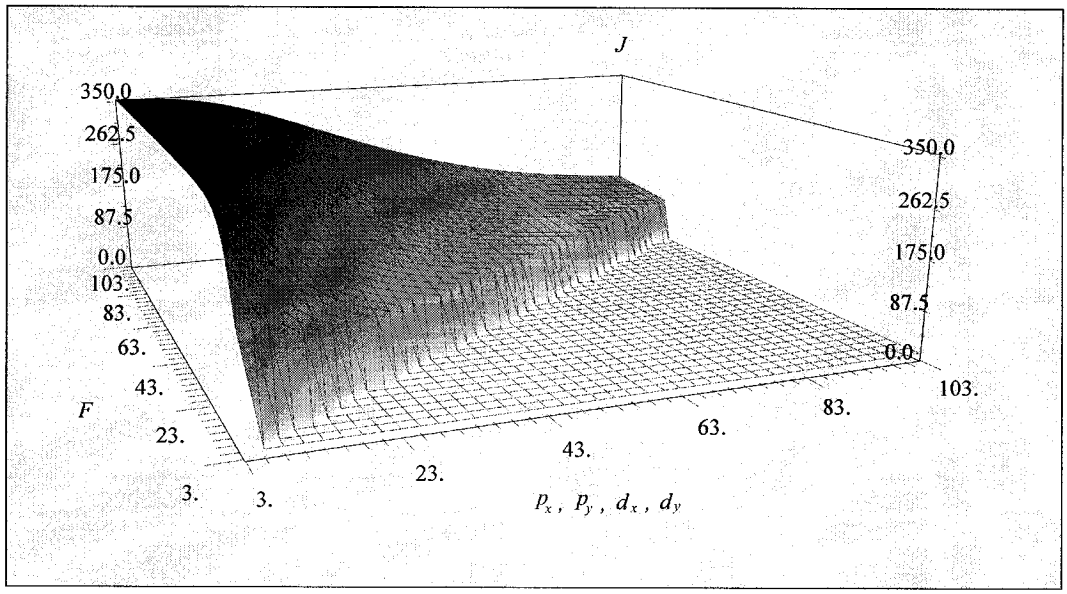

Figure 4.27. Dependence of the objective function (4.76) on the CCD pixel sizes and F for H = 400 km, Object 1, spectral range: 0.40 – 1.05 μm, SNR_{Th} = 18.

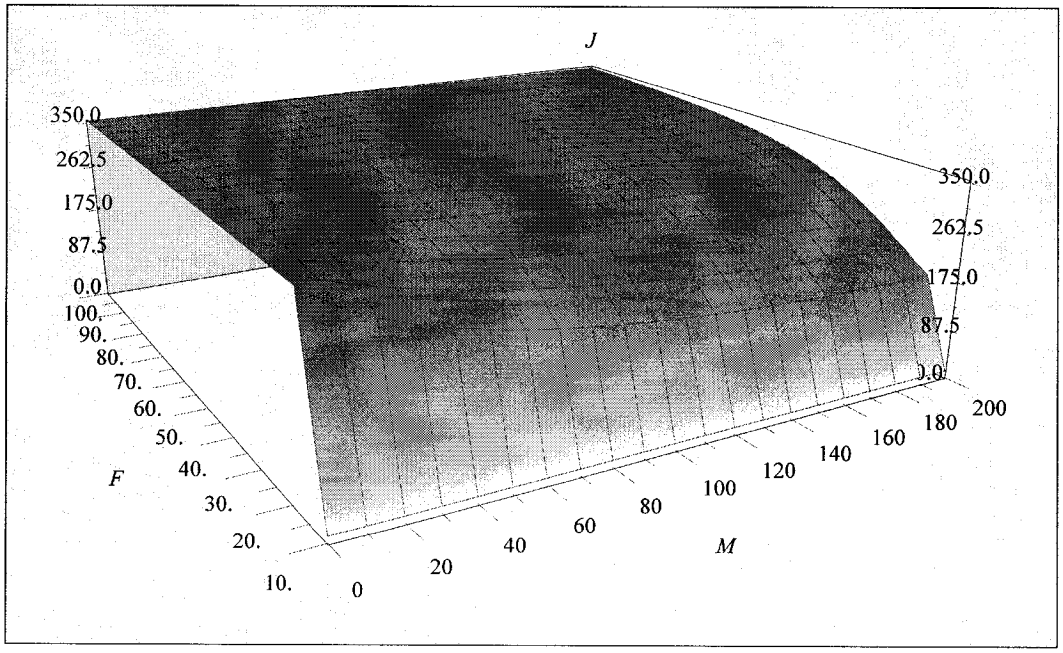

Figure 4.28. Dependence of the objective function (4.76) on M and F for H = 400 km, Object 1, spectral range: 0.40 – 1.05 μm, SNR_{Th} = 18.

4.3.3. Results for problem 3

The results of the joint OS and CCD optimization give the optimal aperture configurations with the subapertures whose relative positions are similar to ones shown in Section 4.3.1. The difference is only in the values of the distances between the subaperture centers. As a result, we do not show the optimal configurations but provide the necessary corresponding numeric information in the tables below.

Here we compare the distances between the subaperture centers, the effective focal length, the pixel sizes, the number of TDI lines, and the minimal and maximal SNR depending on some variable parameters located in the first column of each table. All the numerical values are the same as taken in Sections 4.3.1 and 4.3.2 for H = 400 km, Object 1, the spectral range of 0.75 – 1.05 μm, and the non-zero IA and OPD errors if nothing is said else. In addition, the maximum possible effective focal length was restricted by 5.0 m. All the results show the maximum possible magnitude of the focal length.

Table 4.17 shows independence of the optimal CCD parameters on the observed objects, and already known dependence of the subaperture distances on the object spectral reflectance (see Sections 4.3.1 and 4.3.2).

Table 4.17. Optimal parameters versus the object spectral reflectance, H = 600 km, spectral range: 0.40 – 1.05 μm.

Object	s_{12}	s_{13}	s_{23}	F	p_x	p_y	M	$SNR_{\min}$	$SNR_{\max}$
1	0.476	0.499	0.476	5.00	3.1	3.1	200	0.0004	2.79
2	0.309	0.346	0.307	5.00	3.1	3.1	200	0.33	2.16

Table 4.18 shows the linear inverse dependence of the pixel size on the altitude, i.e. 600 / 400 ≡ 4.6875 / 3.125, the independence of the number of TDI lines, and already known dependence of the subaperture distances on the altitude (see Section 4.3.2).

Table 4.18. Optimal parameters versus the altitude.

H	s_{12}	s_{13}	s_{23}	F	p_x	p_y	M	$SNR_{\min}$	$SNR_{\max}$
400	0.312	0.332	0.311	5.00	4.6875	4.6875	200	1.09	6.45
600	0.477	0.503	0.477	5.00	3.125	3.125	200	0.002	3.49

Table 4.19 shows the dependence of the subaperture distances on β_V : a decrease in the differences as β_V increases. The greater β_V , the smaller the CCD MTF in the y-direction. Since this MTF is greater than in the x-direction (see Section 4.3.1), the equating of the x- and y-MTF occurs, and as a result, the distances tend to be equal. We also see an independence of the pixel size and a decrease in the number of TDI lines as β_V increases.

Table 4.19. Optimal parameters versus the angle between the vectors $\vec{V}_{img}$ and $\vec{V}_{ch}$.

β_V	s_{12}	s_{13}	s_{23}	F	p_x	p_y	M	$SNR_{\min}$	$SNR_{\max}$
0.2	0.312	0.332	0.311	5.00	4.7	4.7	200	1.09	6.45
0.4	0.316	0.326	0.316	5.00	4.7	4.7	157	1.54	5.28

Table 4.20 shows the dependence of the subaperture distances on α_V : the stretching of the configuration in the y-direction as α_V increases. This situation is inverse to the previous one with respect to the aperture configuration, and is similar with respect to the pixel size and the number of TDI lines.

Table 4.20. Optimal parameters versus the parameter of synchronization of the velocities V_{img} and V_{ch}.

α_V	s_{12}	s_{13}	s_{23}	F	p_x	p_y	M	$SNR_{\min}$	$SNR_{\max}$
1.01	0.312	0.332	0.311	5.00	4.7	4.7	200	1.09	6.45
1.02	0.310	0.334	0.310	5.00	4.7	4.7	100	0.72	4.69

Table 4.21 shows the already known dependence of the subaperture distances on the IA and OPD errors (see Sections 4.3.1 and 4.3.2). Besides, we see an independence of the CCD parameters on a presence (Y) or an absence (N) of the IA and OPD errors.

Table 4.21. Optimal parameters versus the presence (Y) or absence (N) of the IA and OPD errors.

IA and OPD	s_{12}	s_{13}	s_{23}	F	p_x	p_y	M	$SNR_{\min}$	$SNR_{\max}$
Y	0.312	0.332	0.311	5.00	4.7	4.7	200	1.09	6.45
N	0.311	0.327	0.311	5.00	4.7	4.7	200	1.76	10.18

Table 4.22 shows the linear dependence of the pixel size on the effective focal length, i.e. 5.00 / 10.00 ≡ 4.6875 / 9.375 (see also Figure 4.27), and a practical independence of the aperture configuration on F. The number of TDI lines is independent too.

Table 4.22. Optimal parameters versus the upper bound of the effective focal length.

F_2	s_{12}	s_{13}	s_{23}	F	p_x	p_y	M	$SNR_{\min}$	$SNR_{\max}$
5.00	0.312	0.332	0.311	5.00	4.6875	4.6875	200	1.09	6.45
10.00	0.312	0.331	0.312	10.00	9.375	9.375	200	1.29	7.58

Table 4.23 shows an interesting decrease in the subaperture distances as R_{22} increases, while all the other parameters remain unchangeable. The optimal values of the outer radii equal 0.150 m.

Table 4.23. Optimal parameters versus the upper bound of the outer subaperture radii.

R_{22}	s_{12}	s_{13}	s_{23}	F	p_x	p_y	M	$SNR_{\min}$	$SNR_{\max}$
0.130	0.312	0.332	0.311	5.00	4.6875	4.6875	200	1.09	6.45
0.150	0.310	0.327	0.310	5.00	4.6875	4.6875	200	1.63	7.90

Table 4.24, like Table 4.23, shows a similar dependence of the subaperture distances as the active aperture area increases; all the other parameters remain unchangeable. The optimal values of the inner radii equal 0.045 m.

Table 4.24. Optimal parameters versus the lower bound of the inner subaperture radii.

R_{11}	s_{12}	s_{13}	s_{23}	F	p_x	p_y	M	SNR_{min}	SNR_{max}
0.055	0.312	0.332	0.311	5.00	4.6875	4.6875	200	1.09	6.45
0.045	0.309	0.333	0.310	5.00	4.6875	4.6875	200	1.09	6.85

Now let us compare the results for R = 0.5 m and R = 0.4 m. We have used the second resolution value, since one of the high resolution imaging satellite planned for launch in 2007 (OrbView-5[104] of ORBIMAGE, Dulles, VA) is required to have a panchromatic spatial resolution of 0.41 m, H = 684 km. Table 4.25, like F_2-dependence in Table 4.22, shows a linear dependence of the pixel size on the spatial resolution, i.e. 0.5 / 0.4 ≡ 4.6875 / 3.75. But the ratios of the corresponding subaperture distances are inverse proportional to the ratio of the spatial resolutions, with some greater coefficients in the range of 1.26 – 1.27.

Table 4.25. Optimal parameters versus the spatial resolution.

R	s_{12}	s_{13}	s_{23}	F	p_x	p_y	M	SNR_{min}	SNR_{max}
0.5	0.312	0.332	0.311	5.00	4.6875	4.6875	200	1.09	6.45
0.4	0.394	0.419	0.394	5.00	3.75	3.75	200	0.21	3.93

4.4. Summary

The presented results show the opportunity of solving the considered optimization problems of the aperture configuration, the effective focal length, the CCD pixel size, and the number of TDI lines for the space-based OES, using a fast convergent gradient method with the objective functions formulated on the basis of the SNR depending on the MTF of a distributed aperture. This is demonstrated on the samples of the OS consisting of two and three annular subapertures, using the SNR criterion calculated at the given value of the spatial ground resolution. The results show optimal solutions of the optimization problems depending on diverse variable parameters. The information on the magnitudes of the SNR presented in the tables can be used for determination of the number of the subapertures and their sizes while the information on the SNR decrease can be useful in design of a beam combination control system to produce necessary requirements to its accuracy on basis of permissible deteriorations of the visual perception probability.

Chapter 5

Conclusions and contributions

1. The possibility of applying gradient optimization methods to the optimization of the distributed aperture configuration is investigated. The appropriate approach based on approximation of step functions with zero-value regions by continuously differentiable functions that have no zero-value regions is proposed. The presented results show the opportunity for solving the problem of aperture configuration optimization by means of gradient methods, applying such an approximation. The method is demonstrated using examples of circular and annular subapertures typically used in space telescopes. Obviously such an approach can be also applied to the optimization of apertures including subapertures with polygonal shape which are popular for segmented mirror telescopes, and with elliptical shape occurred in the engineering design of non-axially-symmetrical OSs. It can be also used for both types of multiaperture optical telescopes, the Michelson and Fizeau, and for both space and earth science missions.

2. The influence of the residual random IA and OPD errors of the beam combination system on the OTF of the distributed OS is researched. It is described with the help of the widely used technique of the MTF. In this way, having expressed the optical MTF as a continuously changing function in the random variables of the IA and OPD errors, the problem of taking these beam combiner errors into account is reduced to the problem of finding the statistical characteristics of the OTF. On the basis of the Fraunhofer approach to the Kirchhoff diffraction theory, the analytical expression for the IOTF is deduced. It shows the dependence of the IOTF on the residual random IA and OPD errors of a beam combination system for the optical distributed aperture consisting of circular and annular subapertures. Using the Gaussian probability distributions for the random errors, the expression for the AOTF is deduced on dependence of the statistical parameters of the errors. Application of the average MTF computed on basis of the AOTF calculated with the help of the statistical modeling or the analytical technique gives an opportunity to estimate the influence of the IA and OPD errors on the quality of the resultant image in the common focal plane of the OS. The results can be used for both space and earth sciences missions.

3. Using the research results of the optimization problem of the distributed aperture configuration, and applying the deduced formulas describing the influence of the residual random IA and OPD errors on the AOTF, the software for calculation of the optimal parameters and values of:
   - aperture configuration
   - effective focal length

- geometrical size of a CCD pixel and the number of TDI lines

at the prescribe value of the spatial ground resolution is developed. This software can also help calculate the systems with the optimal parameters of the optical and electronic subsystems, and to produce the necessary requirements to the accuracy of the beam combination control system, and to the CCD characteristics in a stage of the OES engineering design.

The shown results give an opportunity to apply methods of calculation and optimization of the OESs with monolithic apertures to the development of the OESs with distributed apertures. We hope that the presented research will help to calculate the optimal parameters of the corresponding parts of the space-based OESs with distributed apertures, and make a contribution to the common work on the research and creation of the innovative space-based systems with distributed optical subsystems. It is expected that the results of this work will be a base to investigate the more complicated systems of several micro-satellites whose relative positions are continuously changing in space.

Thus, the thesis contribution related to the engineering designs of the space-based OESs with distributed apertures consists of three parts:

- application of the gradient optimization methods for optimization of the distributed optical aperture configurations calculated on basis of the objective functions having zero-values regions;

- analytical description of the influence of the random IA and OPD errors of a beam combination system on the optical characteristics of the OES expressed in terms of the MTF technique;
- a base for more complicated systems like micro-satellites moving in space.

Chapter 6

Future work

1. For the step pupil function approximation, we have used arctangent. But sometimes this function is not suitable for analytical integration, and we were obliged to utilize procedures of numerical integration which enlarged the calculation time essentially. We would like to consider some other approximation functions like the error function erf(x).

2. The analysis of the objective function is a necessary phase of the work before or together with the optimization procedure if we want to be sure in the calculated results. The greater number of the subapertures, the more complicated objective function – the greater probability to have non-global optimal solution. In this connection, one can plan to analyze the already considered objective functions for the subaperture number greater than three.

3. We have seen that the solutions of the optimization problems strongly depend on the application of the system and its possible technical parameters. In this connection, the main component of the future work related to the considered optimization problem, we see in the more accurate determination of the objective functions and constraints concerned with the real purposes of the system application. Of course, the destination of the system determines the objective function completely. But the formula description requires specific work. As to the constraints, we mean the technological restrictions imposed by the present levels of science and industry on the manufacturing of all the OES components whose characteristics are taken into account in system design stages. It relates to both the optical and electronics subsystems of the complex, i.e. production of optical subtelescopes, a beam combination system (mirrors, prism, etc.) and its control system (sensors, algorithms, actuating devices, etc.), a TDI-CCD, signal processing, etc.

References

1. "Earth observation history on technology introduction," URL: http://www.eoportal.org/documents/kramer/history.pdf, in H. J. Kramer, *Observation of the Earth and its Environment. Survey of Missions and Sensors*, 4th Ed., Springer–Verlag, Berlin (2002).

2. A. B. Meinel, "Cost scaling laws applicable to very large optical telescopes", in *Instrumentation in astronomy III*, Ed. by D. L. Crawford, Proceedings of SPIE, **172**, 2–7 (1979).

3. A. B. Meinel, M. P. Meinel, "Optical phased array configuration for an extremely large telescope," Applied Optics, **43**, 601–607 (2004).

4. A. L. Duncan, R. D. Sigler, D. M. Stubbs, "Multiple-aperture telescope array with a high fill factor," in *Highly Innovative Space Telescope Concepts*, Ed. by H. A. MacEwen, Proceedings of SPIE, **4849**, 257–268 (2002).

5. T.A. Pauls, "Origins of sparse aperture imaging," in *Aerospace Conference*, Proceedings of IEEE, **3**, 1421–1427 (2001).

6. A. Labeyrie, "Interference fringes obtained on Vega with two optical telescopes", Astrophys. J., **196**, L71–L75 (1975).

7. Jet Propulsion Laboratory, SIM PlanetQuest, URL: http://planetquest.jpl.nasa.gov/SIM/sim_index.html.

8. Jet Propulsion Laboratory, Terrestrial Planet Finder, URL: http://planetquest.jpl.nasa.gov/TPF/tpf_index.html.

9. L. Arnold, A. M. Lagrange, D. Mourard, P. Riaud, M. Ferrari, S. Gillet, P. Kern, L. Koechlin, A. Labeyrie, O. Lardière, F. Malbet, G. Perrin, G. Rousset, and M. Tallon, "High angular resolution in 2010–2020: possible post-VLT/VLTI instruments and R&D priorities," SF2A, 237–240, EDP Sciences (2002).

10. L. Arnold, A. M. Lagrange, D. Mourard, P. Riaud, M. Ferrari, S. Gillet, P. Y. Kern, L. Koechlin, A. Labeyrie, O. Lardière, F. Malbet, G. S. Perrin, G. Rousset, and M. Tallon, "High angular resolution in 2010–2020: a comparison between possible post-VLT/VLTI instruments," in *Interferometry for Optical Astronomy II*, Ed. by W. A. Traub, Proceedings of SPIE, **4838**, 134–143 (2003).

11. T. Cwik, W. Boncyk, K. Anderson ,"Technology challenges for Earth observation from higher orbits," in *Enabling Sensor and Platform Technologies for Spaceborne Remote Sensing*, Ed. by G. J. Komar, J. Wang, T. Kimura, Proceedings of SPIE, **5659**, 171–184 (2005).

12. L. M. Mazzuca, K. G. Carpenter, R. G. Lyon, J. Marzouk, P. Petrone III, P. Cottle, P. Dogoda, H. Huet, P. Liiva, D. Mozurkewich, J. T. Armstrong, X. Zhang, G. Solyar, L. G. Mundy, "The Fizeau interferometer testbed (FIT): developing and testing the technologies needed for space-based interferometric imaging systems," in *New*

Frontiers in Stellar Interferometry, Ed. by W. A. Traub, Proceedings of SPIE, **5491**, 1034–1042 (2004).

13. W. A. Traub, "Combining beams from separated telescopes," Applied Optics, **25**, 528–532 (1986).

14. A. Labeyrie, "Resolved imaging of extra-solar planets with future 10–100 km optical interferometric arrays", A&AS, **118**, 517–524 (1996).

15. O. Lardiere, A. Labeyrie, D. Mourard, P. Riaud, L. Arnold, J. Dejonghe, S. Gillet, "VIDA (VLTI imaging with a densified array): a densified pupil combiner proposed for snapshot imaging with the VLTI," in *Interferometry for Optical Astronomy II*, Ed. by W. A. Traub, Proceedings of SPIE, **4838**, 1018–1027 (2003).

16. M. Faucherre, B. Delabre, P. Dierickx, and F. Merkle, "Michelson- versus Fizeau-type beam combination: is there a difference?" in *Amplitude and Intensity Spatial Interferometry*, Ed. by J. B. Breckinridge, Proceedings of SPIE, **1237**, 206–217 (1990).

17. A. J. den Dekker, A. van den Bos, "Resolution: a survey", JOSA A, **14**, 547–557 (1997).

18. Merriam-Webster Online Dictionary, URL: http://www.m-w.com/.

19. A.B. Meinel, M.P. Meinel, N. J. Woolf, "Multiple aperture telescope diffraction images," Applied optics and optical engineering, **9**, 149–201 (1983).

20. J. E. Harvey and R. A. Rockwell, "Performance characteristics of phased array and thinned aperture optical telescopes," Optical Engineering, **27**, 762–768 (1988).

21. J. Flores, G. Paez, and M. Strojnik, "Diluted-aperture mirror with a performance equivalent to that of the Keck," in *Spaceborne Remote Sensing VII*, Ed. By M. Scholl, Proceedings of SPIE, **3759**, 389–397 (1999).

22. J. L. Flores, G. Paez, and M. Strojnik, "Design of a diluted aperture by use of the practical cutoff frequency," Applied Optics, **38**, 6010–6018 (1999).

23. J. L. Flores, G. Paez, and M. Strojnik, "Optimal aperture configuration for a segmented and partially diluted extremely large telescope," Journal of Modern Optics, **50**, 729–742 (2003).

24. A.B. Meinel, "Aperture synthesis using independent telescopes," Applied Optics, **9**, 2501–2504 (1970).

25. R. V. Shack, J. D. Rancourt, H. Morrow, "Effects of dilution on a six-element synthetic aperture," Applied Optics, **10**, 257–259 (1971).

26. J. E. Harvey, A. Kotha, and R. L. Phillips, "Image characteristics in applications utilizing dilute subaperture arrays," Applied Optics, **34**, 2983–2992 (1995).

27. R. Barakat, "Dilute aperture diffraction imagery and object reconstruction," Optical Engineering, **29**, 131–139 (1990).

28. J. E. Harvey, A. K. Thompson, R. L. Phillips, "Fundamental limitations of reciprocal path imaging through the atmosphere with dilute subaperture arrays," in *Atmospheric*

Propagation and Remote Sensing III, Ed. by W. A. Flood, W. B. Miller, Proceedings of SPIE, **2222**, 470–484 (1994).

29. H. F. A. Tschunko, P. J. Sheehan, "Aperture configuration and imaging performance," Applied Optics, **10**, 1432–1438 (1971).

30. C. Rollins, P. E. Nebolsine, N. Humer, D. Mozurkewich, L. J. Rickard, "Enhancement of sparse aperture imaging through multiwavelength synthesis," in *Highly Innovative Space Telescope Concepts*, Ed. by H. A. MacEwen, Proceedings of SPIE, **4849**, 124–133 (2002).

31. R. B. Hindsley, L. J. Rickard, "The general image quality equation and the structure of the modulation transfer function," New Frontiers in Stellar Interferometry, Ed. by W. A. Traub, Proceedings of SPIE, **5491**, 1557–1562 (2004).

32. J. R. Fienup, "MTF and integration time versus fill factor for sparse-aperture imaging systems," in *Imaging Technology and Telescopes*, Ed. by J. W. Bilbro, J. B. Breckinridge, R. A. Carreras, S. R. Czyzak, M. J. Eckart, R. D. Fiete, P. S. Idell, Proceedings of SPIE, **4091**, 43–47 (2000).

33. R. D. Fiete, J. A. Mooney, T. A. Tantalo, J. R. Calus, "Image quality assessment of sparse-aperture designs with decreasing fill factors," in *Imaging Technology and Telescopes*, Ed. by J. W. Bilbro, J. B. Breckinridge, R. A. Carreras, S. R. Czyzak, M. J. Eckart, R. D. Fiete, P. S. Idell, Proceedings of SPIE, **4091**, 64–73 (2000).

34. R. B. Hindsley, D. Mozurkewich, "Signal to noise in sparse aperture imaging," in *Aerospace Conference*, Proceedings of IEEE, **3**, 1429–1443 (2001).

35. R. Fiete, T. Tantalo, J. Calus, J. Mooney, "Image quality assessment of sparse aperture designs", in *Applied Imagery Pattern Recognition Workshop*, Proceedings of IEEE, **29**, 269 – 282 (2000).

36. R. D. Fiete, T. A. Tantalo, J. R. Calus, and J. A. Mooney, "Image quality of sparse-aperture designs for remote sensing," Optical Engineering, **41**, 1957–1969 (2002).

37. J. E. Harvey, A. B. Wissinger, and A. N. Bunner, "A parametric study of various synthetic aperture telescope configurations for coherent imaging applications," in *Infrared, Adaptive, and Synthetic Aperture Optical Systems*, Ed. by R. B. Johnson, W. L. Wolfe and J. S. Fender, Proceedings of SPIE, **643**, 194–207 (1986).

38. S. M. Watson and J. P. Mills, "Two-point resolution criterion for multiaperture optical telescopes," JOSA A, **5**, 893–903 (1988).

39. "The VLT interferometer implementation plan," ESO/VLT Interferometry Panel, Ed. by J. M. Beckers, VLT Report 59b, European Southern Observatory, Garching, Germany (1989).

40. M. Faucherre, F. Merkle, and F. Vakili, "Beam combination in aperture synthesis from space: field of view limitations and (u, v) plane coverage optimization," in *New Technologies for Astronomy*, Ed. by J.-P. Swings, Proceedings of SPIE, **1130**, 138–145 (1989).

41. J. P. Fitch and T. W. Lawrence, "Placement of multiple apertures for imaging telescopes," in *Amplitude and Intensity Spatial Interferometry*, Ed. by J. B. Breckinridge, Proceedings of SPIE, **1237**, 61–69 (1990).

42. L. Damé and M. Martic, "Study of an optimized configuration for interferometric imaging of complex and extended solar structures," in *Targets for Space-Based Interferometry*, Ed. by C. Mattok, Proceedings of ESA, **SP-354**, 201–208 (1992).

43. J. L. Flores, M. Strojnik, G. Paez, "Diluted-aperture mirror with a constraint on the cut-off frequency," in *Infrared Spaceborne Remote Sensing VI*, Ed. by M. Strojnik, B. F. Andresen, Proceedings of SPIE, **3437**, 416–423 (1998).

44. E. M. Sabatke and J. M. Sasián, "Phase theory for multiple aperture systems," Optical Engineering, **41**, 647–655 (2002).

45. L. M. Mugnier, G. Rousset, and F. Cassaing, "Aperture configuration optimality criterion for phased arrays of optical telescopes," JOSA A, **13**, 2367– 2374 (1996).

46. R. L. Lucke, "Fundamentals of wide-field sparse-aperture imaging," in *Aerospace Conference*, Proceedings of IEEE, **3**, 1401–1419 (2001).

47. M. J. E. Golay, "Point arrays having compact, nonredundant autocorrelations," JOSA, **61**, 272–273 (1971).

48. F. Roddier , "Redundant versus nonredundant beam recombination in an aperture synthesis with coherent optical arrays," JOSA A, **4**, 1396–1401 (1987).

49. J. R. P. Angel, "Sensitivity of optical interferometers with coherent image combination," in *Interferometry for Optical Astronomy II*, Ed. by W. A. Traub, Proceedings of SPIE, **4838**, 126–133 (2003).

50. J. D. Monnier, R. Millan-Gabet, P. G. Tuthill, W. A. Traub, N. P. Carleton, V. C. du Foresto, W. C. Danchi, M. G. Lacasse, S. Morel, G. S. Perrin, I. L. Porro, "Aperture synthesis using multiple facilities: Keck aperture masking and the IOTA interferometer," in *Interferometry for Optical Astronomy II*, Ed. by W. A. Traub, Proceedings of SPIE, **4838**, 379–386 (2003).

51. R. G. Lyon, J. E. Dorband, J. M. Hollis , "Computational complexity in space-based optical systems," in *Wavelet Applications VII*, Ed. by H. H. Szu, M. Vetterli, W. J. Campbell, J. R. Buss, Proceedings of SPIE, **4056**, 86–98 (2000).

52. W. H. Swann, "Constrained optimization by direct search," Chapter VII, in P. E. Gill and W. Murray, *Numerical Methods for Constrained Optimization*, Academic Press, London, pp. 191–217 (1974).

53. M. S. Bazarra, C. M. Shetty, *Nonlinear programming: theory and algorithms*, Wiley, New York (1979).

54. L. D. Weaver, J. S. Fender, C. R. de Hainut, "Design considerations for multiple telescope imaging arrays," Optical Engineering, **27**, 730–735 (1988).

55. Z. Hu, S. Le, and D. Yang, "Effects of the phased errors on beams combination," in *Free-Space Laser Communication Technologies IV*, Ed. by D. L. Begley, B. D. Seery, Proceedings of SPIE, **1635**, 118–125 (1992).

56. S.-J. Chung, D. W. Miller, O. L. de Weck, "Design and implementation of sparse aperture imaging systems," in *Highly Innovative Space Telescope Concepts*, Ed. by H. A. MacEwen, Proceedings of SPIE, **4849**, 181–192 (2002).

57. D. W. McCarthy Jr., E. M. Sabatke, R. J. Sarlot, P. M. Hinz, and J. H. Burge, "Cryogenic beam-combiner for very low background, 2–20 micron interferometry on the 22.8 m Large Binocular Telescope," in *Interferometry in Optical Astronomy*, Ed. by P. J. Léna, A. Quirrenbach, Proceedings of SPIE, **4006**, 659–672 (2000).

58. J. E. Harvey, M. J. MacFarlane, and J. L. Forgham, "Design and performance of ranging telescopes: monolithic versus synthetic aperture," Optical Engineering, **24**, 183–188 (1985).

59. R. Kwong, "Analytic expression for the MTF of an array of circular unaberrated phased apertures," Applied Optics, **27**, 2055–2060 (1988).

60. J. E.Harvey, C. Ftaclas, "Field-of-view limitations of phased telescope arrays," Applied Optics, **34**, 5787–5798 (1995).

61. J. E. Baldwin, C. A. Haniff, "The application of interferometry to optical astronomical imaging," Phil. Trans. R. Soc. Lond. A 360, 969–986 (2002).

62. M. Schoeller, "Fizeau beam combination with optical interferometers: some ideas for second-generation VLTI instrumentation," in *Interferometry in Optical Astronomy*, Ed. by P. J. Lena, A. Quirrenbach, Proceedings of SPIE, **4006**, 116–123 (2000).

63. L. Abe, "Specificities of interferometric beam combination techniques for direct imaging," in *New Frontiers in Stellar Interferometry*, Ed. by W. A. Traub, Proceedings of SPIE, **5491**, 1519–1527 (2004).

64. Y. Lin, R. D. Bartos, R. P. Korechoff, and S. B. Shaklan, "Space beam combiner for long-baseline interferometry," in *Sensors, Cameras, and Systems for Scientific/Industrial Applications*, Ed. by M. M. Blouke, G. M. Williams Jr., Proceedings of SPIE, **3649**, 134–143 (1999).

65. S.-J. Chung, D. W. Miller, O. L. de Weck, "ARGOS testbed: study of multidisciplinary challenges of future spaceborne interferometric arrays," Optical Engineering, **43**, 2156–2167 (2004).

66. J. L. Flores, M. Strojnik, G. Páez, G. García-Torales , "Effects of misalignment errors on the optical transfer functions of synthetic aperture telescopes," Applied Optics, **43**, 5926–5932 (2004).

67. F. Baron, F. Cassaing, A. Blanc, D. Laubier, "Cophasing a wide field multi-aperture array by phase-diversity: influence of aperture redundancy and dilution," in *Interferometry in Space*, Ed. by M. Shao, Proceedings of SPIE, **4852**, 663–673 (2003).

68. R. L. Lucke, "Influence of Seidel distortion on combining beams from a phased telescope array," Applied Optics, **38**, 4776–4783 (1999).

69. F. Tasker, B. Plourde, L. Palecki, A. Reed, "Efficient simulation of the effect of random metrology errors on a sparse aperture system," in *Aerospace Conference*, Proceedings of IEEE, **4**, 1781–1789 (2003).

70. G. Chanan, and M. Troy, "Strehl ratio and modulation transfer function for segmented mirror telescopes as functions of segment phase error," Applied Optics, **38**, 6642–6647 (1999).

71. B. Mennesson, and J. M. Mariotti, "Array configurations for a space infrared nulling interferometer dedicated to the search for Earthlike extrasolar planets", ICARUS, **128**, 202–212 (1997).

72. I. Tcherniavski, M. Kahrizi, "Optimization of the optical sparse array configuration," Optical Engineering, **44**, 103201 (2005).

73. I. Tcherniavski, M. Kahrizi, "Influence of the random image alignment and optical path difference errors of a beam combination system on the OTF of the optical sparse array," Submitted (Journal of Optical Engineering, 2005).

74. I. Tcherniavski, M. Kahrizi, "Optimization of the aperture configuration, the effective focal length, the size of a CCD pixel, and the number of TDI lines of the space-based optical-electronic system with a distributed aperture," Submitted (Journal of Optical Engineering, 2006).

75. J. W. Goodman, *Introduction to Fourier optics*, 2nd Ed., McGraw-Hill, New York, (1996), p. 145.

76. J. W. Goodman, *Statistical Optics*, Wiley, New York, (2000), p. 321.

77. *Principles of Optics*, by Max Born and Emil Wolf, 6th Ed., Pergamon Press (1980), p.385.

78. J. A. McCormick, R. Alter-Gartenberg, F. O. Huck, "Image gathering and restoration: information and visual quality," JOSA A, **6**, 987–1005 (1989).

79. J. M. Irvine, "National Imagery Interpretability Rating Scale (NIIRS)," in *Encyclopedia of Optical Engineering*, Ed. by R. G. Driggers, Marcel Dekker, Inc., pp. 1442–1456 (2003).

80. J. C. Leachtenauer, "Image quality equations and NIIRS," in *Encyclopedia of Optical Engineering*, Ed. by R. G. Driggers, Marcel Dekker, Inc., pp. 794–811 (2003).

81. R. D. Fiete and Th. Tantalo, "Comparison of SNR image quality metrics for remote sensing systems," Optical Engineering, **40**, 574–585 (2001).

82. J. Johnson, "Analysis of image forming systems," Proceedings of the Image Intensifier Symposium, U. S. Army Engineering Research Development Laboratories, Fort Belvoir, Virginia, October 1958.

83. F. A. Rosell, R. H. Willson, "Recent psychophysical experiments and the display signal-to-noise ratio concept," Chapter 5, in *Perception of displayed information*, Ed. by L. M. Biberman, Plenum Press (1973).

84. J. A. Hall, "Signal and noise in the display of images," in P. G. Jespers, F. Van de Wiele, and M. H. White, *Solid State Imaging*, Noordhoff, Leyden, The Netherlands, pp. 637–658 (1976).

85. J. M. Lloyd, *Thermal Imaging Systems*, Plenum Press, New York (1975), p. 400.

86. Reference 85, p. 144.

87. ASTM G173-03 Reference Spectra Derived from SMARTS v. 2.9.2,URL: http://rredc.nrel.gov/solar/spectra/am1.5/ASTMG173/ASTMG173.html.

88. ASTER spectral library, URL: http://speclib.jpl.nasa.gov/.

89. Class: Image Processing Laboratory for Remote Sensing, URL: http://www.ece.arizona.edu/~dial/ece531/UA%20CALIBRATION.pdf.

90. A. Berk, G. P. Anderson, L. S.Bernstein, P. K. Acharya, H. Dothe, M. W. Matthew, S. M. Adler-Golden, J. H. Chetwynd, Jr., S. C. Richtsmeier, B. Pukall, C. L. Allred, L. S. Jeong, and M. L. Hoke, "MODTRAN4 radiative transfer modeling for atmospheric correction," in *Optical Spectroscopic Techniques and Instrumentation for Atmospheric and Space Research III*, Ed. by A. M. Larar, Proceedings of SPIE, **3756**, 348–353 (1999).

91. F. Roddier, "The effects of atmospheric turbulence in optical astronomy," in *Progress in Optics*, Ed. by E. Wolf, **XIX**, 281–376 (1981).

92. V. I. Tatarski, *Wave Propagation in a Turbulent Medium*, McGraw-Hill, New York (1961).

93. R. E. Hufnagel, N. R. Stanley, "Modulation transfer function associated with image transmission through turbulent media," JOSA, **54**, 52–61 (1964).

94. D. L. Fried, "Optical resolution through a randomly inhomogeneous medium for very long and very short exposures," JOSA, **56**, 1372–1379 (1966).

95. D. L. Fried, "Limiting resolution looking down through the atmosphere," JOSA, **56**, 1380–1384 (1966).

96. D. L. Fried, "Statistics of a geometric representation of wavefront distortion," JOSA, **55**, 1427–1435 (1965).

97. D. F. Barbe, "Time delay and integration image sensors," in P. G. Jespers, F. Van de Wiele, and M. H. White, in *Solid State Imaging*, Noordhoff, Leyden, The Netherlands, pp. 659–671 (1976).

98. M. H. White, "Design of solid-state imaging arrays," in P. G. Jespers, F. Van de Wiele, and M. H. White, in *Solid State Imaging*, Noordhoff, Leyden, The Netherlands, pp. 485–522 (1976).

99. Photometrics encyclopedia: Saturation and Blooming, URL: http://www.photomet.com/library_enc_saturation.shtml

100. Photometrics glossary: noise, URL: http://www.photomet.com/library_glossary.html#noise

101. CCD525 Time Delay Integration Line Scan Sensor, URL: http://www.fairchildimaging.com/main/documents/CCD525DataSheet.pdf.

102. QuickBird, URL: http://www.digitalglobe.com/about/quickbird.html

103. WorldView 1, URL: http://space.skyrocket.de/doc_sdat/worldview-1.htm

104. OrbView-5, URL: http://www.orbimage.com/corp/orbimage_system/ov5/index.html

Appendix A

Gradient expressions for solving the aperture configuration problem

The gradient of the objective function (2.10) is

$$\nabla J(S_f) =$$

$$= 2\iint_{S_f}[MTF_{OS}(f_u,f_v) - mtf_{des}(f_u,f_v)]\cdot[\nabla MTF_{OS}(f_u,f_v) - \nabla mtf_{des}(f_u,f_v)]df_u df_v. \quad \text{(A.1)}$$

We consider the case when $mtf_{des}(f_u,f_v)$ is a constant, hence $\nabla mtf_{des}(f_u,f_v) \equiv 0$. Since the pupil functions (2.5) and (2.6) are nonnegative real, then, using Eq.(2.14), the MTF is

$$MTF_{OS}(f_u,f_v) = \frac{\frac{1}{\pi^2}\iint_{A_0} s_0 \cdot s_1(u_f,v_f)dudv}{\frac{1}{\pi^2}\iint_{A_0} s_0^2 dudv}, \quad \text{(A.2)}$$

where for the circular subapertures the sums s_0 and $s_1(u_f,v_f)$ are

$$s_0 = \sum_{i=1}^{N}\left\{\frac{\pi}{2} - \arctan\left[\eta\cdot\left((u-u_i)^2 + (v-v_i)^2 - r_i^2\right)\right]\right\}, \quad \text{(A.3)}$$

$$s_1(u_f,v_f) \equiv s_1 = \sum_{j=1}^{N}\left\{\frac{\pi}{2} - \arctan\left[\eta\cdot\left((u-u_j-u_f)^2 + (v-v_j-v_f)^2 - r_j^2\right)\right]\right\}; \quad \text{(A.4)}$$

and for the annular subapertures:

$$s_0 = \sum_{i=1}^{N} \{\arctan[\eta \cdot ((u-u_i)^2 + (v-v_i)^2 - r_{1i}^2)] -$$

$$- \arctan[\eta \cdot ((u-u_i)^2 + (v-v_i)^2 - r_{2i}^2)]\}, \tag{A.5}$$

$$s_1 = \sum_{j=1}^{N} \{\arctan[\eta \cdot ((u-u_j-u_f)^2 + (v-v_j-v_f)^2 - r_{1j}^2)] -$$

$$- \arctan[\eta \cdot ((u-u_j-u_f)^2 + (v-v_j-v_f)^2 - r_{2j}^2)]\}. \tag{A.6}$$

Then the gradient of the optical MTF (A.2) can be written as

$$\nabla MTF_{OS}(f_u, f_v) =$$

$$= \frac{\iint_{A_0} [\nabla s_0 \cdot s_1 + s_0 \cdot \nabla s_1] dudv}{\iint_{A_0} s_0^2 dudv} - \frac{\iint_{A_0} s_0 \cdot s_1 dudv \cdot 2 \iint_{A_0} s_0 \cdot \nabla s_0 dudv}{\left[\iint_{A_0} s_0^2 dudv\right]^2}, \tag{A.7}$$

where the vectors ∇s_0 and ∇s_1 are ones of the partial derivatives. For the circular subapertures, they are the $1 \times 3N$ vectors:

$$\nabla s_0 = \left[\frac{\partial s_0}{\partial u_1} \quad \frac{\partial s_0}{\partial v_1} \quad \frac{\partial s_0}{\partial r_1} \quad \frac{\partial s_0}{\partial u_2} \quad \frac{\partial s_0}{\partial v_2} \quad \frac{\partial s_0}{\partial r_2} \quad \cdots \quad \frac{\partial s_0}{\partial u_N} \quad \frac{\partial s_0}{\partial v_N} \quad \frac{\partial s_0}{\partial r_N}\right] \tag{A.8}$$

and

$$\nabla s_1 = \left[\frac{\partial s_1}{\partial u_1} \quad \frac{\partial s_1}{\partial v_1} \quad \frac{\partial s_1}{\partial r_1} \quad \frac{\partial s_1}{\partial u_2} \quad \frac{\partial s_1}{\partial v_2} \quad \frac{\partial s_1}{\partial r_2} \quad \cdots \quad \frac{\partial s_1}{\partial u_N} \quad \frac{\partial s_1}{\partial v_N} \quad \frac{\partial s_1}{\partial r_N}\right] \tag{A.9}$$

whose components are

$$\frac{\partial s_0}{\partial u_i} = \frac{2\eta \cdot (u-u_i)}{1 + [\eta \cdot ((u-u_i)^2 + (v-v_i)^2 - r_i^2)]^2}, \tag{A.10}$$

$$\frac{\partial s_0}{\partial v_i} = \frac{2\eta \cdot (v-v_i)}{1 + [\eta \cdot ((u-u_i)^2 + (v-v_i)^2 - r_i^2)]^2}, \tag{A.11}$$

$$\frac{\partial s_0}{\partial r_i} = \frac{2\eta \cdot r_i}{1+\left[\eta \cdot \left((u-u_i)^2 + (v-v_i)^2 - r_i^2\right)\right]^2}; \tag{A.12}$$

$$\frac{\partial s_1}{\partial u_j} = \frac{2\eta \cdot (u-u_j-u_f)}{1+\left[\eta \cdot \left((u-u_j-u_f)^2 + (v-v_j-v_f)^2 - r_j^2\right)\right]^2}, \tag{A.13}$$

$$\frac{\partial s_1}{\partial v_j} = \frac{2\eta \cdot (v-v_j-v_f)}{1+\left[\eta \cdot \left((u-u_j-u_f)^2 + (v-v_j-v_f)^2 - r_j^2\right)\right]^2}, \tag{A.14}$$

$$\frac{\partial s_1}{\partial r_j} = \frac{2\eta \cdot r_j}{1+\left[\eta \cdot \left((u-u_j-u_f)^2 + (v-v_j-v_f)^2 - r_j^2\right)\right]^2}. \tag{A.15}$$

For the annular subapertures, they are the $1 \times 4N$ vectors:

$$\nabla s_0 =$$

$$= \left[\frac{\partial s_0}{\partial u_1} \quad \frac{\partial s_0}{\partial v_1} \quad \frac{\partial s_0}{\partial r_{11}} \quad \frac{\partial s_0}{\partial r_{21}} \quad \frac{\partial s_0}{\partial u_2} \quad \frac{\partial s_0}{\partial v_2} \quad \frac{\partial s_0}{\partial r_{12}} \quad \frac{\partial s_0}{\partial r_{22}} \quad \cdots \quad \frac{\partial s_0}{\partial u_N} \quad \frac{\partial s_0}{\partial v_N} \quad \frac{\partial s_0}{\partial r_{1N}} \quad \frac{\partial s_0}{\partial r_{2N}}\right] \tag{A.16}$$

and

$$\nabla s_1 =$$

$$= \left[\frac{\partial s_1}{\partial u_1} \quad \frac{\partial s_1}{\partial v_1} \quad \frac{\partial s_1}{\partial r_{11}} \quad \frac{\partial s_1}{\partial r_{21}} \quad \frac{\partial s_1}{\partial u_2} \quad \frac{\partial s_1}{\partial v_2} \quad \frac{\partial s_1}{\partial r_{12}} \quad \frac{\partial s_1}{\partial r_{22}} \quad \cdots \quad \frac{\partial s_1}{\partial u_N} \quad \frac{\partial s_1}{\partial v_N} \quad \frac{\partial s_1}{\partial r_{1N}} \quad \frac{\partial s_1}{\partial r_{2N}}\right] \tag{A.17}$$

whose components are

$$\frac{\partial s_0}{\partial u_i} = 2\eta \cdot (u-u_i) \cdot \left[\frac{-1}{1+\left[\eta \cdot \left((u-u_i)^2 + (v-v_i)^2 - r_{1i}^2\right)\right]^2} + \right.$$

$$\left. + \frac{1}{1+\left[\eta \cdot \left((u-u_i)^2 + (v-v_i)^2 - r_{2i}^2\right)\right]^2}\right], \tag{A.18}$$

$$\frac{\partial s_0}{\partial v_i} = 2\eta \cdot (v - v_i) \cdot \left[\frac{-1}{1 + \left[\eta \cdot \left((u-u_i)^2 + (v-v_i)^2 - r_{1i}^2\right)\right]^2} + \right.$$

$$\left. + \frac{1}{1 + \left[\eta \cdot \left((u-u_i)^2 + (v-v_i)^2 - r_{2i}^2\right)\right]^2} \right], \tag{A.19}$$

$$\frac{\partial s_0}{\partial r_{1i}} = \frac{-2\eta \cdot r_{1i}}{1 + \left[\eta \cdot \left((u-u_i)^2 + (v-v_i)^2 - r_{1i}^2\right)\right]^2}, \tag{A.20}$$

$$\frac{\partial s_0}{\partial r_{2i}} = \frac{2\eta \cdot r_{2i}}{1 + \left[\eta \cdot \left((u-u_i)^2 + (v-v_i)^2 - r_{2i}^2\right)\right]^2}; \tag{A.21}$$

$$\frac{\partial s_1}{\partial u_j} = 2\eta \cdot (u - u_j - u_f) \cdot \left[\frac{-1}{1 + \left[\eta \cdot \left((u-u_j-u_f)^2 + (v-v_j-v_f)^2 - r_{1j}^2\right)\right]^2} + \right.$$

$$\left. + \frac{1}{1 + \left[\eta \cdot \left((u-u_j-u_f)^2 + (v-v_j-v_f)^2 - r_{2j}^2\right)\right]^2} \right], \tag{A.22}$$

$$\frac{\partial s_1}{\partial v_j} = 2\eta \cdot (v - v_j - v_f) \cdot \left[\frac{-1}{1 + \left[\eta \cdot \left((u-u_j-u_f)^2 + (v-v_j-v_f)^2 - r_{1j}^2\right)\right]^2} + \right.$$

$$\left. + \frac{1}{1 + \left[\eta \cdot \left((u-u_j-u_f)^2 + (v-v_j-v_f)^2 - r_{2j}^2\right)\right]^2} \right], \tag{A.23}$$

$$\frac{\partial s_1}{\partial r_{1j}} = \frac{-2\eta \cdot r_{1j}}{1 + \left[\eta \cdot \left((u-u_j-u_f)^2 + (v-v_j-v_f)^2 - r_{1j}^2\right)\right]^2}, \tag{A.24}$$

$$\frac{\partial s_1}{\partial r_{2j}} = \frac{2\eta \cdot r_{2j}}{1 + \left[\eta \cdot \left((u-u_j-u_f)^2 + (v-v_j-v_f)^2 - r_{2j}^2\right)\right]^2}. \tag{A.25}$$

To use the gradient optimization method, we need also to have the gradient matrix of the constraint functions. The inequalities (2.16), (2.17), and (2.19), (2.20) give us the $N+N(N-1)/2 \times 1$ vector G_c of the constraint functions:

$$G_c = \left[\left[(g_i)_{1n} \right] \quad \left[(g_{ij})_{1m} \right] \right]^T =$$

$$= \left[g_1 \quad g_2 \quad \cdots \quad g_N \quad g_{12} \quad g_{13} \quad \cdots \quad g_{1N} \quad g_{23} \quad g_{24} \quad \cdots \quad g_{2N} \quad \cdots \quad g_{(N-1)N} \right]^T, \quad \text{(A.26)}$$

where: $i = 1, \ldots, N\text{-}1$; $j = i+1, \ldots, N$; $n = 1, \ldots, N$, $m = 1, \ldots, N(N\text{-}1)/2$.

Then, for the circular subapertures, the $N+N(N-1)/2 \times 3N$ gradient matrix ∇G_c of the constraint functions is

$$\nabla G_c =$$

$$= \begin{bmatrix}
\frac{\partial g_1}{\partial u_1} & \frac{\partial g_1}{\partial v_1} & \frac{\partial g_1}{\partial r_1} & 0 & 0 & 0 & 0 & 0 & 0 & 0 & 0 & 0 & 0 & \cdots \\
0 & 0 & 0 & \frac{\partial g_2}{\partial u_2} & \frac{\partial g_2}{\partial v_2} & \frac{\partial g_2}{\partial r_2} & 0 & 0 & 0 & 0 & 0 & 0 & 0 & \cdots \\
\cdots & \cdots & \cdots & \cdots & \cdots & \cdots & \cdots & \cdots & \cdots & \cdots & \cdots & \cdots & \cdots & \cdots \\
0 & 0 & 0 & 0 & 0 & 0 & 0 & 0 & 0 & 0 & 0 & 0 & 0 & \cdots \\
\frac{\partial g_{12}}{\partial u_1} & \frac{\partial g_{12}}{\partial v_1} & \frac{\partial g_{12}}{\partial r_1} & \frac{\partial g_{12}}{\partial u_2} & \frac{\partial g_{12}}{\partial v_2} & \frac{\partial g_{12}}{\partial r_2} & 0 & 0 & 0 & 0 & 0 & 0 & 0 & \cdots \\
\frac{\partial g_{13}}{\partial u_1} & \frac{\partial g_{13}}{\partial v_1} & \frac{\partial g_{13}}{\partial r_1} & 0 & 0 & 0 & \frac{\partial g_{13}}{\partial u_3} & \frac{\partial g_{13}}{\partial v_3} & \frac{\partial g_{13}}{\partial r_3} & 0 & 0 & 0 & 0 & \cdots \\
\cdots & \cdots & \cdots & \cdots & \cdots & \cdots & \cdots & \cdots & \cdots & \cdots & \cdots & \cdots & \cdots & \cdots \\
\frac{\partial g_{1N}}{\partial u_1} & \frac{\partial g_{1N}}{\partial v_1} & \frac{\partial g_{1N}}{\partial r_1} & 0 & 0 & 0 & 0 & 0 & 0 & 0 & 0 & 0 & 0 & \cdots \\
0 & 0 & 0 & \frac{\partial g_{23}}{\partial u_2} & \frac{\partial g_{23}}{\partial v_2} & \frac{\partial g_{23}}{\partial r_2} & \frac{\partial g_{23}}{\partial u_3} & \frac{\partial g_{23}}{\partial v_3} & \frac{\partial g_{23}}{\partial r_3} & 0 & 0 & 0 & 0 & \cdots \\
0 & 0 & 0 & \frac{\partial g_{24}}{\partial u_2} & \frac{\partial g_{24}}{\partial v_2} & \frac{\partial g_{24}}{\partial r_2} & 0 & 0 & 0 & \frac{\partial g_{24}}{\partial u_4} & \frac{\partial g_{24}}{\partial v_4} & \frac{\partial g_{24}}{\partial r_4} & 0 & \cdots \\
\cdots & \cdots & \cdots & \cdots & \cdots & \cdots & \cdots & \cdots & \cdots & \cdots & \cdots & \cdots & \cdots & \cdots \\
0 & 0 & 0 & \frac{\partial g_{2N}}{\partial u_2} & \frac{\partial g_{2N}}{\partial v_2} & \frac{\partial g_{2N}}{\partial r_2} & 0 & 0 & 0 & 0 & 0 & 0 & 0 & \cdots \\
\cdots & \cdots & \cdots & \cdots & \cdots & \cdots & \cdots & \cdots & \cdots & \cdots & \cdots & \cdots & \cdots & \cdots \\
0 & 0 & 0 & 0 & 0 & 0 & 0 & 0 & 0 & 0 & 0 & 0 & 0 & \cdots
\end{bmatrix}$$

$$
\begin{bmatrix}
\cdots & 0 & 0 & 0 & 0 & 0 & 0 & 0 \\
\cdots & 0 & 0 & 0 & 0 & 0 & 0 & 0 \\
\cdots & \cdots & \cdots & \cdots & \cdots & \cdots & \cdots & \cdots \\
\cdots & 0 & 0 & 0 & 0 & \dfrac{\partial g_N}{\partial u_N} & \dfrac{\partial g_N}{\partial v_N} & \dfrac{\partial g_N}{\partial r_N} \\
\cdots & 0 & 0 & 0 & 0 & 0 & 0 & 0 \\
\cdots & 0 & 0 & 0 & 0 & 0 & 0 & 0 \\
\cdots & \cdots & \cdots & \cdots & \cdots & \cdots & \cdots & \cdots \\
\cdots & 0 & 0 & 0 & 0 & \dfrac{\partial g_{1N}}{\partial u_N} & \dfrac{\partial g_{1N}}{\partial v_N} & \dfrac{\partial g_{1N}}{\partial r_N} \\
\cdots & 0 & 0 & 0 & 0 & 0 & 0 & 0 \\
\cdots & 0 & 0 & 0 & 0 & 0 & 0 & 0 \\
\cdots & \cdots & \cdots & \cdots & \cdots & \cdots & \cdots & \cdots \\
\cdots & 0 & 0 & 0 & 0 & \dfrac{\partial g_{2N}}{\partial u_N} & \dfrac{\partial g_{2N}}{\partial v_N} & \dfrac{\partial g_{2N}}{\partial r_N} \\
\cdots & \cdots & \cdots & \cdots & \cdots & \cdots & \cdots & \cdots \\
\cdots & 0 & \dfrac{\partial g_{(N-1)N}}{\partial u_{N-1}} & \dfrac{\partial g_{(N-1)N}}{\partial v_{N-1}} & \dfrac{\partial g_{(N-1)N}}{\partial r_{N-1}} & \dfrac{\partial g_{(N-1)N}}{\partial u_N} & \dfrac{\partial g_{(N-1)N}}{\partial v_N} & \dfrac{\partial g_{(N-1)N}}{\partial r_N}
\end{bmatrix}
\tag{A.27}
$$

whose components are

$$
\frac{\partial g_i}{\partial u_i} = -\frac{u_i}{\sqrt{u_i^2 + v_i^2}}, \qquad \frac{\partial g_i}{\partial v_i} = -\frac{v_i}{\sqrt{u_i^2 + v_i^2}}, \qquad \frac{\partial g_i}{\partial r_i} = -1; \tag{A.28}
$$

$$
\frac{\partial g_{ij}}{\partial u_i} = 2(u_i - u_j), \qquad \frac{\partial g_{ij}}{\partial v_i} = 2(v_i - v_j), \qquad \frac{\partial g_{ij}}{\partial r_i} = -2(r_i + r_j), \tag{A.29}
$$

$$
\frac{\partial g_{ij}}{\partial u_j} = -2(u_i - u_j), \qquad \frac{\partial g_{ij}}{\partial v_j} = -2(v_i - v_j), \qquad \frac{\partial g_{ij}}{\partial r_j} = -2(r_i + r_j). \tag{A.30}
$$

For the annular subapertures, the $N+N(N\text{-}1)/2 \times 4N$ gradient matrix ∇G_c is

$$\nabla G_c =$$

$$= \begin{bmatrix}
\frac{\partial g_1}{\partial u_1} & \frac{\partial g_1}{\partial v_1} & \frac{\partial g_1}{\partial r_{11}} & \frac{\partial g_1}{\partial r_{21}} & 0 & 0 & 0 & 0 & 0 & 0 & 0 & 0 & 0 & \cdots \\
0 & 0 & 0 & 0 & \frac{\partial g_2}{\partial u_2} & \frac{\partial g_2}{\partial v_2} & \frac{\partial g_2}{\partial r_{12}} & \frac{\partial g_2}{\partial r_{22}} & 0 & 0 & 0 & 0 & 0 & \cdots \\
\cdots & \cdots & \cdots & \cdots & \cdots & \cdots & \cdots & \cdots & \cdots & \cdots & \cdots & \cdots & \cdots & \cdots \\
0 & 0 & 0 & 0 & 0 & 0 & 0 & 0 & 0 & 0 & 0 & 0 & 0 & \cdots \\
\frac{\partial g_{12}}{\partial u_1} & \frac{\partial g_{12}}{\partial v_1} & \frac{\partial g_{12}}{\partial r_{11}} & \frac{\partial g_{12}}{\partial r_{21}} & \frac{\partial g_{12}}{\partial u_2} & \frac{\partial g_{12}}{\partial v_2} & \frac{\partial g_{12}}{\partial r_{12}} & \frac{\partial g_{12}}{\partial r_{22}} & 0 & 0 & 0 & 0 & 0 & \cdots \\
\frac{\partial g_{13}}{\partial u_1} & \frac{\partial g_{13}}{\partial v_1} & \frac{\partial g_{13}}{\partial r_{11}} & \frac{\partial g_{13}}{\partial r_{21}} & 0 & 0 & 0 & 0 & \frac{\partial g_{13}}{\partial u_3} & \frac{\partial g_{13}}{\partial v_3} & \frac{\partial g_{13}}{\partial r_{13}} & \frac{\partial g_{13}}{\partial r_{23}} & 0 & \cdots \\
\cdots & \cdots & \cdots & \cdots & \cdots & \cdots & \cdots & \cdots & \cdots & \cdots & \cdots & \cdots & \cdots & \cdots \\
\frac{\partial g_{1N}}{\partial u_1} & \frac{\partial g_{1N}}{\partial v_1} & \frac{\partial g_{1N}}{\partial r_{11}} & \frac{\partial g_{1N}}{\partial r_{21}} & 0 & 0 & 0 & 0 & 0 & 0 & 0 & 0 & 0 & \cdots \\
0 & 0 & 0 & 0 & \frac{\partial g_{23}}{\partial u_2} & \frac{\partial g_{23}}{\partial v_2} & \frac{\partial g_{23}}{\partial r_{12}} & \frac{\partial g_{23}}{\partial r_{22}} & \frac{\partial g_{23}}{\partial u_3} & \frac{\partial g_{23}}{\partial v_3} & \frac{\partial g_{23}}{\partial r_{13}} & \frac{\partial g_{23}}{\partial r_{23}} & 0 & \cdots \\
\cdots & \cdots & \cdots & \cdots & \cdots & \cdots & \cdots & \cdots & \cdots & \cdots & \cdots & \cdots & \cdots & \cdots \\
0 & 0 & 0 & 0 & \frac{\partial g_{2N}}{\partial u_2} & \frac{\partial g_{2N}}{\partial v_2} & \frac{\partial g_{2N}}{\partial r_{12}} & \frac{\partial g_{2N}}{\partial r_{22}} & 0 & 0 & 0 & 0 & 0 & \cdots \\
\cdots & \cdots & \cdots & \cdots & \cdots & \cdots & \cdots & \cdots & \cdots & \cdots & \cdots & \cdots & \cdots & \cdots \\
0 & 0 & 0 & 0 & 0 & 0 & 0 & 0 & 0 & 0 & 0 & 0 & 0 & \cdots
\end{bmatrix}$$

$$\begin{bmatrix}
\cdots & 0 & 0 & 0 & 0 & 0 & 0 & 0 & 0 & 0 \\
\cdots & 0 & 0 & 0 & 0 & 0 & 0 & 0 & 0 & 0 \\
\cdots & \cdots & \cdots & \cdots & \cdots & \cdots & \cdots & \cdots & \cdots & \cdots \\
\cdots & 0 & 0 & 0 & 0 & 0 & \frac{\partial g_N}{\partial u_N} & \frac{\partial g_N}{\partial v_N} & \frac{\partial g_N}{\partial r_{1N}} & \frac{\partial g_N}{\partial r_{2N}} \\
\cdots & 0 & 0 & 0 & 0 & 0 & 0 & 0 & 0 & 0 \\
\cdots & 0 & 0 & 0 & 0 & 0 & 0 & 0 & 0 & 0 \\
\cdots & \cdots & \cdots & \cdots & \cdots & \cdots & \cdots & \cdots & \cdots & \cdots \\
\cdots & 0 & 0 & 0 & 0 & 0 & \frac{\partial g_{1N}}{\partial u_N} & \frac{\partial g_{1N}}{\partial v_N} & \frac{\partial g_{1N}}{\partial r_{1N}} & \frac{\partial g_{1N}}{\partial r_{2N}} \\
\cdots & 0 & 0 & 0 & 0 & 0 & 0 & 0 & 0 & 0 \\
\cdots & \cdots & \cdots & \cdots & \cdots & \cdots & \cdots & \cdots & \cdots & \cdots \\
\cdots & 0 & 0 & 0 & 0 & 0 & \frac{\partial g_{2N}}{\partial u_N} & \frac{\partial g_{2N}}{\partial v_N} & \frac{\partial g_{2N}}{\partial r_{1N}} & \frac{\partial g_{2N}}{\partial r_{2N}} \\
\cdots & \cdots & \cdots & \cdots & \cdots & \cdots & \cdots & \cdots & \cdots & \cdots \\
\cdots & 0 & \frac{\partial g_{(N-1)N}}{\partial u_{N-1}} & \frac{\partial g_{(N-1)N}}{\partial v_{N-1}} & \frac{\partial g_{(N-1)N}}{\partial r_{1(N-1)}} & \frac{\partial g_{(N-1)N}}{\partial r_{2(N-1)}} & \frac{\partial g_{(N-1)N}}{\partial u_N} & \frac{\partial g_{(N-1)N}}{\partial v_N} & \frac{\partial g_{(N-1)N}}{\partial r_{1N}} & \frac{\partial g_{(N-1)N}}{\partial r_{2N}}
\end{bmatrix} \tag{A.31}$$

whose components are

$$\frac{\partial g_i}{\partial u_i} = -\frac{u_i}{\sqrt{u_i^2 + v_i^2}}, \quad \frac{\partial g_i}{\partial v_i} = -\frac{v_i}{\sqrt{u_i^2 + v_i^2}}, \quad \frac{\partial g_i}{\partial r_{1i}} = 0, \quad \frac{\partial g_i}{\partial r_{2i}} = -1; \tag{A.32}$$

$$\frac{\partial g_{ij}}{\partial u_i} = 2(u_i - u_j), \quad \frac{\partial g_{ij}}{\partial v_i} = 2(v_i - v_j), \quad \frac{\partial g_{ij}}{\partial r_{1i}} = 0, \quad \frac{\partial g_{ij}}{\partial r_{2i}} = -2(r_{2i} + r_{2j}), \tag{A.33}$$

$$\frac{\partial g_{ij}}{\partial u_j} = -2(u_i - u_j), \quad \frac{\partial g_{ij}}{\partial v_j} = -2(v_i - v_j), \quad \frac{\partial g_{ij}}{\partial r_{1j}} = 0, \quad \frac{\partial g_{ij}}{\partial r_{2j}} = -2(r_{2i} + r_{2j}). \tag{A.34}$$

Appendix B

Fourier transform of the field distribution

Introducing the polar coordinate system (r,φ):

$$x - x_m = r\cos\varphi\,, \quad y - y_m = r\sin\varphi\,, \tag{B1}$$

and taking Ex. (3.13) into account, we have:

$$\int_{-\infty}^{+\infty}\int U(x,y,\lambda)\cdot\exp\left[-i2\pi(\xi x+\vartheta y)\right]dxdy =$$

$$= \sqrt{E_D}\sum_{m=1}^{N}\sqrt{\tau_m}\cdot\exp\left[-i2\pi(\xi x_m+\vartheta y_m)+ik\tilde{\Delta}_m(x_m,y_m)\right]\cdot\int_0^{\infty}\left[r_{2m}J_1(\alpha r_{2m}r)-r_{1m}J_1(\alpha r_{1m}r)\right]\times$$

$$\times\int_0^{2\pi}\exp\left\{-i2\pi r\left[\left(\frac{u_m}{\lambda F}+\xi\right)\cos\varphi+\left(\frac{v_m}{\lambda F}+\vartheta\right)\sin\varphi\right]\right\}d\varphi dr\,. \tag{B2}$$

Using the integral representation of the Bessel function of the first kind[R1]

$$J_k(z)=\frac{1}{2\pi}\int_{-\pi}^{\pi}\exp\left[-ik\varphi+iz\sin\varphi\right]d\varphi\,, \quad k=0,\ 1,\ 2,\ldots, \tag{B3}$$

it is easy to see that

$$\int_0^{2\pi}\exp\left[i(a\cos\varphi+b\sin\varphi-n\varphi)\right]d\varphi = 2\pi J_n\left(\sqrt{a^2+b^2}\right)\exp(in\theta), \tag{B4}$$

where:

$$\sin\theta = \frac{a}{\sqrt{a^2+b^2}},\ \cos\theta = \frac{b}{\sqrt{a^2+b^2}}. \tag{B5}$$

Applying Ex. (B4) to Ex. (B2), the last becomes

$$2\pi\sqrt{E_D}\sum_{m=1}^{N}\sqrt{\tau_m}\cdot\exp\left[-i2\pi\left(\xi x_m+\vartheta y_m\right)+ik\tilde{\Delta}_m(x_m,y_m)\right]\times$$

$$\times\int_0^{\infty}\left[r_{2m}J_1(\alpha r_{2m}r)-r_{1m}J_1(\alpha r_{1m}r)\right]\cdot J_0\left(2\pi r\sqrt{\left(\frac{u_m}{\lambda F}+\xi\right)^2+\left(\frac{v_m}{\lambda F}+\vartheta\right)^2}\right)dr. \tag{B6}$$

Since[R2]

$$\int_0^{\infty}J_{\mu}(ax)J_{\mu-1}(bx)dx=\begin{cases}\dfrac{b^{\mu-1}}{a^{\mu}}, & 0<b<a\\ \dfrac{1}{2b}, & 0<b=a\\ 0, & 0<a<b\end{cases}, \tag{B7}$$

we get the formula for the Fourier transform of the field distribution:

$$\int_{-\infty}^{+\infty}\int U(x,y,\lambda)\cdot\exp\left[-i2\pi\left(\xi x+\vartheta y\right)\right]dxdy=$$

$$=\lambda F\sqrt{E_D}\sum_{m=1}^{N}\sqrt{\tau_m}\cdot\exp\left[-i2\pi\left(\xi x_m+\vartheta y_m\right)+ik\tilde{\Delta}_m(x_m,y_m)\right]\times$$

$$\times\left[K(\xi,\vartheta,\lambda;u_m,v_m,r_{2m})-K(\xi,\vartheta,\lambda;u_m,v_m,r_{1m})\right], \tag{B8}$$

where:

$$K\left(\xi,\vartheta,\lambda;u_m,v_m,r_{jm}\right)=\begin{cases}1, & \sqrt{(\lambda F\xi+u_m)^2+(\lambda F\vartheta+v_m)^2}<r_{jm}\\ \dfrac{1}{2}, & \sqrt{(\lambda F\xi+u_m)^2+(\lambda F\vartheta+v_m)^2}=r_{jm}\\ 0, & \sqrt{(\lambda F\xi+u_m)^2+(\lambda F\vartheta+v_m)^2}>r_{jm}\end{cases}. \tag{B9}$$

Appendix C

Fourier transform of the irradiance distribution

The Fourier transform of the irradiance distribution is defined by Ex. (3.22), where the integration area is formed by the intersections of the areas A_n and A_m. It can be shown geometrically on a draft:[R3] taking denotation (2.12) and denoting

$$u = \lambda F \xi , \qquad v = \lambda F \vartheta , \tag{C1}$$

the integration area is an intersection of the subaperture areas of the aperture with themselves shifted by the vector $\lambda F \vec{f}$. Figure C1 shows such a case for the aperture consisting of two annular and one circular subapertures.

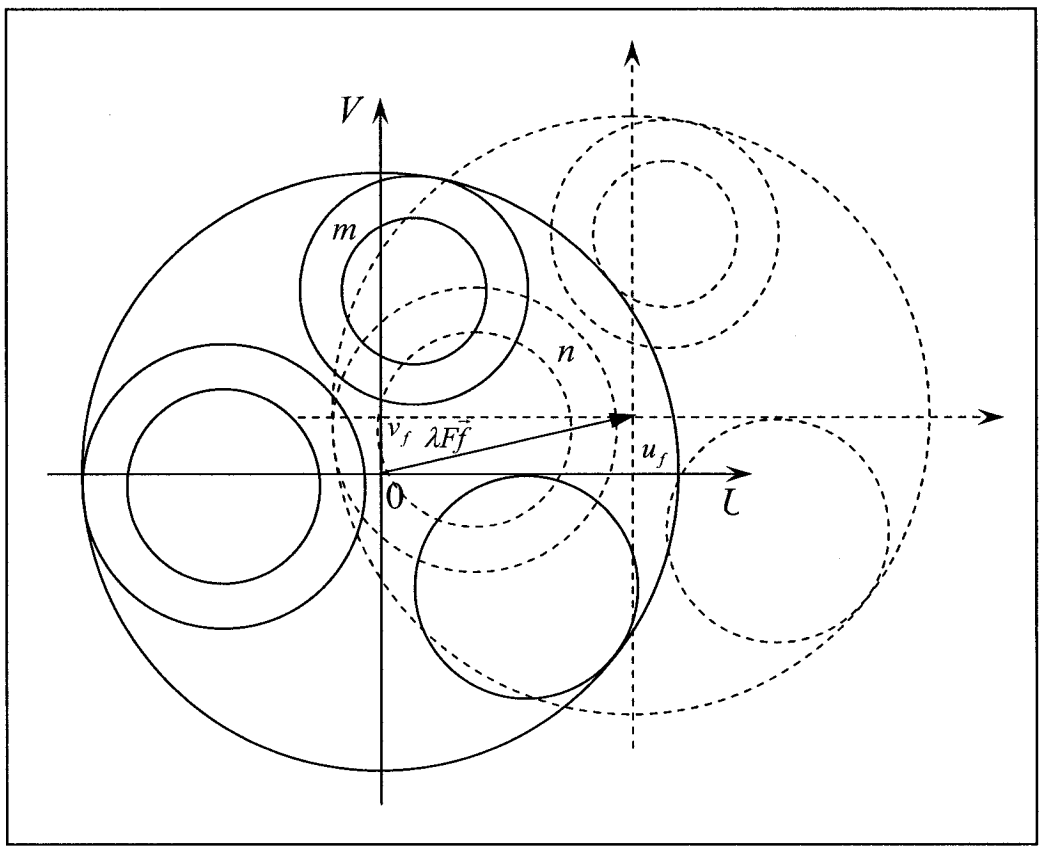

Figure C1. Two apertures shifted by the vector $\lambda F\vec{f}$.

In a mathematical form, the intersection area of the *m*th and *n*th subapertures can be written by the followig:

$$A_n \bigcap A_m =$$

$$= \left\{ \left[\sqrt{\left[\lambda F(f_u - \xi) + u_n\right]^2 + \left[\lambda F(f_v - \vartheta) + v_n\right]^2} < r_{2n} \right] \bigcap \right.$$

$$\left. \left[\sqrt{(\lambda F\xi - u_m)^2 + (\lambda F\vartheta - v_m)^2} < r_{2m} \right] \right\} \setminus$$

$$\left\{ \left[\sqrt{\left[\lambda F(f_u - \xi) + u_n\right]^2 + \left[\lambda F(f_v - \vartheta) + v_n\right]^2} < r_{1n} \right] \bigcap \right.$$

$$\left. \left[\sqrt{(\lambda F\xi - u_m)^2 + (\lambda F\vartheta - v_m)^2} < r_{2m} \right] \right\} \setminus$$

$$\left\{\left[\sqrt{\left[\lambda F\left(f_u-\xi\right)+u_n\right]^2+\left[\lambda F\left(f_v-\vartheta\right)+v_n\right]^2}<r_{2n}\right]\cap\right.$$

$$\left.\left[\sqrt{\left(\lambda F\xi-u_m\right)^2+\left(\lambda F\vartheta-v_m\right)^2}<r_{1m}\right]\right\}. \tag{C2}$$

The expression (3.22) takes the form

$$\int_{-\infty}^{+\infty}\int U(x,y,\lambda)\cdot U^*(x,y,\lambda)\cdot\exp\left[-i2\pi\left(f_u x+f_v y\right)\right]dxdy=$$

$$=E_D\sum_{n=1}^{N}\sqrt{\tau_n}\cdot\exp\left[-i\alpha\left(x_n u_f+y_n v_f\right)+ik\tilde{\Delta}_n(x_n,y_n)\right]\times$$

$$\times\sum_{m=1}^{N}\sqrt{\tau_m}\cdot\iint_{A_n\cap A_m}\exp\left\{i\alpha\left[\left(x_n-x_m\right)u+\left(y_n-y_m\right)v\right]-ik\tilde{\Delta}_m(x_m,y_m)\right\}dudv, \tag{C3}$$

where the integration areas are

$$A_n\cap A_m=$$

$$=\left\{\left[\sqrt{\left[u-\left(u_n+u_f\right)\right]^2+\left[v-\left(v_n+v_f\right)\right]^2}<r_{2n}\right]\cap\left[\sqrt{\left(u-u_m\right)^2+\left(v-v_m\right)^2}<r_{2m}\right]\right\}\setminus$$

$$\left\{\left[\sqrt{\left[u-\left(u_n+u_f\right)\right]^2+\left[v-\left(v_n+v_f\right)\right]^2}<r_{1n}\right]\cap\left[\sqrt{\left(u-u_m\right)^2+\left(v-v_m\right)^2}<r_{2m}\right]\right\}\setminus$$

$$\left\{\left[\sqrt{\left[u-\left(u_n+u_f\right)\right]^2+\left[v-\left(v_n+v_f\right)\right]^2}<r_{2n}\right]\cap\left[\sqrt{\left(u-u_m\right)^2+\left(v-v_m\right)^2}<r_{1m}\right]\right\}. \tag{C4}$$

It is obvious that if some subset is empty, the corresponding member of the integral equals zero. For calculation of the integral in (C3) over nonempty intersection areas, let me define a new right rectangular Cartesian coordinate system $U'0'V'$ so that its origin coincides with the center of the *m*th subaperture, and the axis $0'U'$ passes through the center of the shifted *n*th subaperture – Figure C2(a).

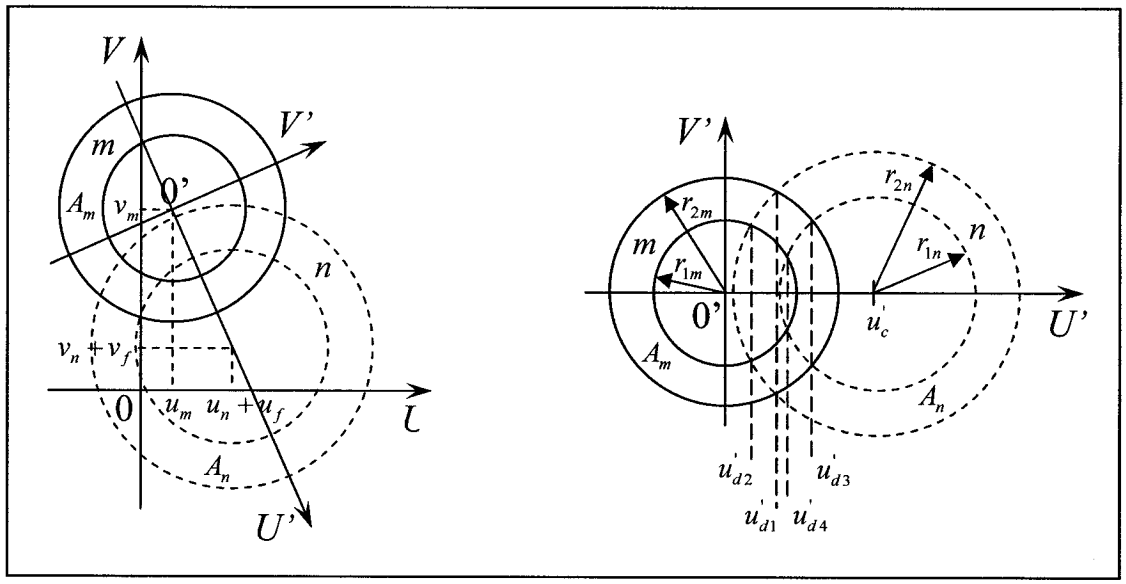

(a) **(b)**

Figure C2. New coordinate system $U'0V'$ with respect to the old one $U0V$ – (a); division of the integration area into subsets – (b).

Then the direction cosines c_{nm}^{11} and c_{nm}^{21} of the axis $0'U'$, and c_{nm}^{12} and c_{nm}^{22} of the axis $0'V'$ of the new coordinate system with respect to the old one $U0V$ are defined by the following values:

$0'U'$:

$$\begin{cases} c_{nm}^{11} = \dfrac{u_n + u_f - u_m}{\sqrt{(u_n + u_f - u_m)^2 + (v_n + v_f - v_m)^2}} \\ c_{nm}^{21} = \dfrac{v_n + v_f - v_m}{\sqrt{(u_n + u_f - u_m)^2 + (v_n + v_f - v_m)^2}} \end{cases}; \qquad \text{(C5)}$$

$0'V'$:

$$\begin{cases} c_{nm}^{12} = -\dfrac{v_n + v_f - v_m}{\sqrt{\left(u_n + u_f - u_m\right)^2 + \left(v_n + v_f - v_m\right)^2}} \\ c_{nm}^{22} = \dfrac{u_n + u_f - u_m}{\sqrt{\left(u_n + u_f - u_m\right)^2 + \left(v_n + v_f - v_m\right)^2}} \end{cases}; \tag{C6}$$

and the old coordinates (u,v) are defined in terms of the new ones (u',v') by the following expressions:

$$u = c_{nm}^{11}u' + c_{nm}^{12}v' + u_m, \qquad v = c_{nm}^{21}u' + c_{nm}^{22}v' + v_m. \tag{C7}$$

Making these substitutes into the calculated integral in (C3), we have (omitting the constant factor):

$$\iint\limits_{A_n \cap A_m} \exp\{i\alpha[(x_n - x_m)u + (y_n - y_m)v]\}dudv = \exp\{i\alpha[(x_n - x_m)u_m + (y_n - y_m)v_m]\} \times$$

$$\times \iint\limits_{A_n' \cap A_m'} \exp\left(i\alpha\left\{\left[c_{nm}^{11}(x_n - x_m) + c_{nm}^{21}(y_n - y_m)\right]u' + \left[c_{nm}^{12}(x_n - x_m) + c_{nm}^{22}(y_n - y_m)\right]v'\right\}\right)du'dv'; \tag{C8}$$

and the integration area becomes – Figure C2(b):

$$A_n' \cap A_m' = \left\{\Omega_{n1}' \cup \Omega_{m1}'\right\} \setminus \left\{\left[\Omega_{n2}' \cup \Omega_{m2}'\right] \cup \left[\Omega_{n3}' \cup \Omega_{m3}'\right] \cup \left[\Omega_{n4}' \cup \Omega_{m4}'\right]\right\}, \tag{C9}$$

where the corresponding subsets are defined by the expressions:

$$\Omega_{n1}' = \left\{u',v' :\ u_c' - r_{2n} < u' < u_{d1}',\ -\sqrt{r_{2n}^2 - \left(u_c' - u'\right)^2} < v' < \sqrt{r_{2n}^2 - \left(u_c' - u'\right)^2}\right\}, \tag{C10}$$

$$\Omega_{m1}' = \left\{u',v' :\ u_{d1}' < u' < r_{2m},\ -\sqrt{r_{2m}^2 - u'^2} < v' < \sqrt{r_{2m}^2 - u'^2}\right\}, \tag{C11}$$

$$\Omega_{n2}' = \left\{u',v' :\ u_c' - r_{2n} < u' < u_{d2}',\ -\sqrt{r_{2n}^2 - \left(u_c' - u'\right)^2} < v' < \sqrt{r_{2n}^2 - \left(u_c' - u'\right)^2}\right\}, \tag{C12}$$

$$\Omega_{m2}' = \left\{u',v' :\ u_{d2}' < u' < r_{1m},\ -\sqrt{r_{1m}^2 - u'^2} < v' < \sqrt{r_{1m}^2 - u'^2}\right\}, \tag{C13}$$

$$\Omega_{n3}^{'}=\left\{u^{'},v^{'}:\ u_c^{'}-r_{1n}<u^{'}<u_{d3}^{'},\ -\sqrt{r_{1n}^2-\left(u_c^{'}-u^{'}\right)^2}<v^{'}<\sqrt{r_{1n}^2-\left(u_c^{'}-u^{'}\right)^2}\right\}, \tag{C14}$$

$$\Omega_{m3}^{'}=\left\{u^{'},v^{'}:\ u_{d3}^{'}<u^{'}<r_{2m},\ -\sqrt{r_{2m}^2-u^{'2}}<v^{'}<\sqrt{r_{2m}^2-u^{'2}}\right\}, \tag{C15}$$

$$\Omega_{n4}^{'}=\left\{u^{'},v^{'}:\ u_c^{'}-r_{1n}<u^{'}<u_{d4}^{'},\ -\sqrt{r_{1n}^2-\left(u_c^{'}-u^{'}\right)^2}<v^{'}<\sqrt{r_{1n}^2-\left(u_c^{'}-u^{'}\right)^2}\right\}, \tag{C16}$$

$$\Omega_{m4}^{'}=\left\{u^{'},v^{'}:\ u_{d4}^{'}<u^{'}<r_{1m},\ -\sqrt{r_{1m}^2-u^{'2}}<v^{'}<\sqrt{r_{1m}^2-u^{'2}}\right\}; \tag{C17}$$

the values u_{dk} are

$$\begin{cases} u_{d1}=\dfrac{r_{2m}^2+u_c^{'2}-r_{2n}^2}{2u_c^{'}}, & u_{d2}=\dfrac{r_{1m}^2+u_c^{'2}-r_{2n}^2}{2u_c^{'}} \\ u_{d3}=\dfrac{r_{2m}^2+u_c^{'2}-r_{1n}^2}{2u_c^{'}}, & u_{d4}=\dfrac{r_{1m}^2+u_c^{'2}-r_{1n}^2}{2u_c^{'}} \end{cases}; \tag{C18}$$

and

$$u_c^{'}=\sqrt{\left(u_n+u_f-u_m\right)^2+\left(v_n+v_f-v_m\right)^2}\ . \tag{C19}$$

Then the integral in Ex. (C8) can be represented as

$$\iint\limits_{A_n^{'}\cap A_m^{'}}\exp\left(i\alpha\left\{\left[c_{nm}^{11}\left(x_n-x_m\right)+c_{nm}^{21}\left(y_n-y_m\right)\right]u^{'}+\left[c_{nm}^{12}\left(x_n-x_m\right)+c_{nm}^{22}\left(y_n-y_m\right)\right]v^{'}\right\}\right)du^{'}dv^{'}=$$

$$=\iint\limits_{A_n^{'}\cap A_m^{'}}\exp\left[i\left(a_{nm}u^{'}+b_{nm}v^{'}\right)\right]du^{'}dv^{'}=$$

$$=\left\{\left(\iint\limits_{\Omega_{n1}^{'}}+\iint\limits_{\Omega_{m1}^{'}}\right)-\left(\iint\limits_{\Omega_{n2}^{'}}+\iint\limits_{\Omega_{m2}^{'}}\right)-\left(\iint\limits_{\Omega_{n3}^{'}}+\iint\limits_{\Omega_{m3}^{'}}\right)+\left(\iint\limits_{\Omega_{n4}^{'}}+\iint\limits_{\Omega_{m4}^{'}}\right)\right\}\exp\left[i\left(a_{nm}u^{'}+b_{nm}v^{'}\right)\right]du^{'}dv^{'}, \tag{C20}$$

where:

$$a_{nm}=\alpha\left[c_{nm}^{11}\left(x_n-x_m\right)+c_{nm}^{21}\left(y_n-y_m\right)\right],\ \ b_{nm}=\alpha\left[c_{nm}^{12}\left(x_n-x_m\right)+c_{nm}^{22}\left(y_n-y_m\right)\right]. \tag{C21}$$

We see that it is enough to deduce the formulas for two type of the subset in Ex. (C20), for example, $\Omega_{n1}^{'}$ and $\Omega_{m1}^{'}$.

C.1. Integration over $\Omega_{n1}^{'}$. For $b_{nm} \neq 0$, the integral over $\Omega_{n1}^{'}$ is

$$\iint\limits_{\Omega_{n1}^{'}} \exp\left[i\left(a_{nm}u^{'} + b_{nm}v^{'}\right)\right]du^{'}dv^{'} = \int\limits_{u_c^{'}-r_{2n}}^{u_{d1}} \exp\left(ia_{nm}u^{'}\right) \int\limits_{-\sqrt{r_{2n}^2-\left(u_c^{'}-u^{'}\right)^2}}^{\sqrt{r_{2n}^2-\left(u_c^{'}-u^{'}\right)^2}} \exp\left(ib_{nm}v^{'}\right)dv^{'}du^{'} =$$

$$= \frac{1}{ib_{nm}} \int\limits_{u_c^{'}-r_{2n}}^{u_{d1}} \left\{\exp\left[ia_{nm}u^{'} + ib_{nm}\sqrt{r_{2n}^2-\left(u_c^{'}-u^{'}\right)^2}\right] - \exp\left[ia_{nm}u^{'} - ib_{nm}\sqrt{r_{2n}^2-\left(u_c^{'}-u^{'}\right)^2}\right]\right\}du^{'}. \tag{C22}$$

Making the substitution

$$u_c^{'} - u^{'} = r_{2n}\cos\varphi, \tag{C23}$$

and using the Euler's formula $\sin z = \left[\exp(iz) - \exp(-iz)\right]/2i$, the integral becomes equal to

$$-\frac{r_{2n}}{2b_{nm}}\exp\left(ia_{nm}u_c^{'}\right)\int\limits_0^{\Theta_{nm}^{22}}\left\{\exp\left[i\left(r_{2n}q_{nm}\sin(\varphi-\varphi_{nm})+\varphi\right)\right] - \exp\left[i\left(r_{2n}q_{nm}\sin(\varphi-\varphi_{nm})-\varphi\right)\right] -\right.$$

$$\left. - \exp\left[-i\left(r_{2n}q_{nm}\sin(\varphi+\varphi_{nm})-\varphi\right)\right] + \exp\left[-i\left(r_{2n}q_{nm}\sin(\varphi+\varphi_{nm})+\varphi\right)\right]\right\}d\varphi, \tag{C24}$$

where: Θ_{nm}^{22} is defined by the expression:

$$\Theta_{jl}^{gh} = \begin{cases} \pi, & \dfrac{r_{gj}^2 + u_c^{'2} - r_{hl}^2}{2r_{gj}u_c^{'}} < -1 \\ \arccos\left(\dfrac{r_{gj}^2 + u_c^{'2} - r_{hl}^2}{2r_{gj}u_c^{'}}\right), & -1 \leq \dfrac{r_{gj}^2 + u_c^{'2} - r_{hl}^2}{2r_{gj}u_c^{'}} \leq 1 \\ 0, & \dfrac{r_{gj}^2 + u_c^{'2} - r_{hl}^2}{2r_{gj}u_c^{'}} > 1 \end{cases} \tag{C25}$$

indices: g = 1, 2; and h = 1, 2;

$$q_{nm} = \sqrt{a_{nm}^2 + b_{nm}^2} = \alpha\sqrt{(x_n - x_m)^2 + (y_n - y_m)^2}\,, \tag{C26}$$

$$\sin\varphi_{nm} = \frac{a_{nm}}{q_{nm}}, \qquad \cos\varphi_{nm} = \frac{b_{nm}}{q_{nm}}. \tag{C27}$$

Making the substitution $\phi = \varphi - \varphi_{nm}$ in the first two subintegral exponential functions, and $\phi = \varphi + \varphi_{nm}$ in the second ones, Ex. (C24) takes the form

$$-\frac{r_{2n}}{2b_{nm}}\exp(ia_{nm}u_c')\left\{\int_{-\varphi_{nm}}^{\Theta_{nm}^{22}-\varphi_{nm}}\{\exp[i(r_{2n}q_{nm}\sin\phi + \phi + \varphi_{nm})] - \exp[i(r_{2n}q_{nm}\sin\phi - \phi - \varphi_{nm})]\}d\phi + \right.$$

$$\left. + \int_{\theta}^{\Theta_{nm}^{22}+\varphi_{nm}}\{-\exp[-i(r_{2n}q_{nm}\sin\phi - \phi + \varphi_{nm})] + \exp[-i(r_{2n}q_{nm}\sin\phi + \phi - \varphi_{nm})]\}d\phi\right\}. \tag{C28}$$

Grouping the integrals with the $\exp(i\varphi_{nm})$ and $\exp(-i\varphi_{nm})$ factors, we get

$$-\frac{r_{2n}}{2b_{nm}}\exp(ia_{nm}u_c')\times$$

$$\times\left\{\exp(i\varphi_{nm})\left[\int_{-\varphi_{nm}}^{\Theta_{nm}^{22}-\varphi_{nm}}\exp[i(r_{2n}q_{nm}\sin\phi + \phi)]d\phi + \int_{\varphi_{nm}}^{\Theta_{nm}^{22}+\varphi_{nm}}\exp[-i(r_{2n}q_{nm}\sin\phi + \phi)]d\phi\right] - \right.$$

$$\left. - \exp(-i\varphi_{nm})\left[\int_{-\varphi_{nm}}^{\Theta_{nm}^{22}-\varphi_{nm}}\exp[i(r_{2n}q_{nm}\sin\phi - \phi)]d\phi + \int_{\varphi_{nm}}^{\Theta_{nm}^{22}+\varphi_{nm}}\exp[-i(r_{2n}q_{nm}\sin\phi - \phi)]d\phi\right]\right\}. \tag{C29}$$

Using the Euler's formula $\exp(iz) = \cos z + i\sin z$, we can rewrite (C29) as

$$-\frac{r_{2n}}{2b_{nm}}\exp(ia_{nm}u_c')\times$$

$$\times\left\{\exp(i\varphi_{nm})\left(\int_{-\varphi_{nm}}^{\Theta_{nm}^{22}-\varphi_{nm}}\cos(r_{2n}q_{nm}\sin\phi + \phi)d\phi + \int_{\varphi_{nm}}^{\Theta_{nm}^{22}+\varphi_{nm}}\cos(r_{2n}q_{nm}\sin\phi + \phi)d\phi + \right.\right.$$

$$+i\left[\int_{-\varphi_{nm}}^{\Theta_{nm}^{22}-\varphi_{nm}}\sin\left(r_{2n}q_{nm}\sin\phi+\phi\right)d\phi-\int_{\varphi_{nm}}^{\Theta_{nm}^{22}+\varphi_{nm}}\sin\left(r_{2n}q_{nm}\sin\phi+\phi\right)d\phi\right]\Bigg)-$$

$$-\exp\left(-i\varphi_{nm}\right)\Bigg(\int_{-\varphi_{nm}}^{\Theta_{nm}^{22}-\varphi_{nm}}\cos\left(r_{2n}q_{nm}\sin\phi-\phi\right)d\phi+\int_{\varphi_{nm}}^{\Theta_{nm}^{22}+\varphi_{nm}}\cos\left(r_{2n}q_{nm}\sin\phi-\phi\right)d\phi+$$

$$+i\left[\int_{-\varphi_{nm}}^{\Theta_{nm}^{22}-\varphi_{nm}}\sin\left(r_{2n}q_{nm}\sin\phi-\phi\right)d\phi-\int_{\varphi_{nm}}^{\Theta_{nm}^{22}+\varphi_{nm}}\sin\left(r_{2n}q_{nm}\sin\phi-\phi\right)d\phi\right]\Bigg)\Bigg\}. \qquad \text{(C30)}$$

The sums and differences of the integrals can be expressed in terms of the incomplete cylindrical functions. The first sum is

$$\int_{-\varphi_{nm}}^{\Theta_{nm}^{22}-\varphi_{nm}}\cos\left(r_{2n}q_{nm}\sin\phi+\phi\right)d\phi+\int_{\varphi_{nm}}^{\Theta_{nm}^{22}+\varphi_{nm}}\cos\left(r_{2n}q_{nm}\sin\phi+\phi\right)d\phi\equiv$$

$$\equiv\left(\int_{-\varphi_{nm}}^{\Theta_{nm}^{22}-\varphi_{nm}}+\int_{\varphi_{nm}}^{\Theta_{nm}^{22}+\varphi_{nm}}\right)\cos\left(r_{2n}q_{nm}\sin\phi+\phi\right)d\phi=$$

$$=\left(\int_{-\varphi_{nm}}^{0}+\int_{0}^{\Theta_{nm}^{22}-\varphi_{nm}}+\int_{0}^{\Theta_{nm}^{22}+\varphi_{nm}}-\int_{0}^{\varphi_{nm}}\right)\cos\left(r_{2n}q_{nm}\sin\phi+\phi\right)d\phi=$$

$$=\left(-\int_{0}^{-\varphi_{nm}}+\int_{0}^{\Theta_{nm}^{22}-\varphi_{nm}}+\int_{0}^{\Theta_{nm}^{22}+\varphi_{nm}}-\int_{0}^{\varphi_{nm}}\right)\cos\left(r_{2n}q_{nm}\sin\phi+\phi\right)d\phi=$$

$$=\left(\int_{0}^{\varphi_{nm}}+\int_{0}^{\Theta_{nm}^{22}-\varphi_{nm}}+\int_{0}^{\Theta_{nm}^{22}+\varphi_{nm}}-\int_{0}^{\varphi_{nm}}\right)\cos\left(r_{2n}q_{nm}\sin\phi+\phi\right)d\phi=$$

$$=\left(\int_{0}^{\Theta_{nm}^{22}-\varphi_{nm}}+\int_{0}^{\Theta_{nm}^{22}+\varphi_{nm}}\right)\cos\left(r_{2n}q_{nm}\sin\phi+\phi\right)d\phi=$$

$$=\left(\int_{0}^{\Theta_{nm}^{22}-\varphi_{nm}}+\int_{0}^{\Theta_{nm}^{22}+\varphi_{nm}}\right)\cos\left(-\phi-r_{2n}q_{nm}\sin\phi\right)d\phi=$$

$$= \pi\left[\mathbf{J}_{-1}\left(r_{2n}q_{nm}, \Theta_{nm}^{22-}\right) + \mathbf{J}_{-1}\left(r_{2n}q_{nm}, \Theta_{nm}^{22+}\right)\right], \tag{C31}$$

where

$$\mathbf{J}_{\nu}(z,\Theta) = \frac{1}{\pi}\int_{0}^{\Theta}\cos\left(\nu\phi - z\sin\phi\right)d\phi \tag{C32}$$

is the incomplete Anger function; and

$$\Theta_{nm}^{22\pm} = \Theta_{nm}^{22} \pm \varphi_{nm}\,. \tag{C33}$$

The first difference of the integrals is

$$\int_{-\varphi_{nm}}^{\Theta_{nm}^{22}-\varphi_{nm}}\sin\left(r_{2n}q_{nm}\sin\phi + \phi\right)d\phi - \int_{\varphi_{nm}}^{\Theta_{nm}^{22}+\varphi_{nm}}\sin\left(r_{2n}q_{nm}\sin\phi + \phi\right)d\phi \equiv$$

$$\equiv \left(\int_{-\varphi_{nm}}^{\Theta_{nm}^{22}-\varphi_{nm}} - \int_{\varphi_{nm}}^{\Theta_{nm}^{22}+\varphi_{nm}}\right)\sin\left(r_{2n}q_{nm}\sin\phi + \phi\right)d\phi =$$

$$= \left(\int_{-\varphi_{nm}}^{0} + \int_{0}^{\Theta_{nm}^{22}-\varphi_{nm}} - \int_{0}^{\Theta_{nm}^{22}+\varphi_{nm}} + \int_{0}^{\varphi_{nm}}\right)\sin\left(r_{2n}q_{nm}\sin\phi + \phi\right)d\phi =$$

$$= \left(-\int_{0}^{-\varphi_{nm}} + \int_{0}^{\Theta_{nm}^{22}-\varphi_{nm}} - \int_{0}^{\Theta_{nm}^{22}+\varphi_{nm}} + \int_{0}^{\varphi_{nm}}\right)\sin\left(r_{2n}q_{nm}\sin\phi + \phi\right)d\phi =$$

$$= \left(-\int_{0}^{\varphi_{nm}} + \int_{0}^{\Theta_{nm}^{22}-\varphi_{nm}} - \int_{0}^{\Theta_{nm}^{22}+\varphi_{nm}} + \int_{0}^{\varphi_{nm}}\right)\sin\left(r_{2n}q_{nm}\sin\phi + \phi\right)d\phi =$$

$$= \left(\int_{0}^{\Theta_{nm}^{22}-\varphi_{nm}} - \int_{0}^{\Theta_{nm}^{22}+\varphi_{nm}}\right)\sin\left(r_{2n}q_{nm}\sin\phi + \phi\right)d\phi =$$

$$= -\left(\int_{0}^{\Theta_{nm}^{22}-\varphi_{nm}} - \int_{0}^{\Theta_{nm}^{22}+\varphi_{nm}}\right)\sin\left(-\phi - r_{2n}q_{nm}\sin\phi\right)d\phi =$$

$$= -\pi\left[\mathbf{E}_{-1}(r_{2n}q_{nm}, \Theta_{nm}^{22-}) - \mathbf{E}_{-1}(r_{2n}q_{nm}, \Theta_{nm}^{22+})\right], \tag{C34}$$

where

$$\mathbf{E}_{\nu}(z,\Theta)=\frac{1}{\pi}\int_{0}^{\Theta}\sin(\nu\phi-z\sin\phi)d\phi \tag{C35}$$

is the incomplete Weber function.

In a similar manner, it can be shown that:

$$\left(\int_{-\varphi_{nm}}^{\Theta_{nm}^{22}-\varphi_{nm}}+\int_{\varphi_{nm}}^{\Theta_{nm}^{22}+\varphi_{nm}}\right)\cos(r_{2n}q_{nm}\sin\phi-\phi)d\phi=\pi\left[\mathbf{J}_1(r_{2n}q_{nm},\Theta_{nm}^{22-})+\mathbf{J}_1(r_{2n}q_{nm},\Theta_{nm}^{22+})\right], \tag{C36}$$

$$\left(\int_{-\varphi_{nm}}^{\Theta_{nm}^{22}-\varphi_{nm}}-\int_{\varphi_{nm}}^{\Theta_{nm}^{22}+\varphi_{nm}}\right)\sin(r_{2n}q_{nm}\sin\phi-\phi)d\phi=-\pi\left[\mathbf{E}_1(r_{2n}q_{nm},\Theta_{nm}^{22-})-\mathbf{E}_1(r_{2n}q_{nm},\Theta_{nm}^{22+})\right]. \tag{C37}$$

So, the integral over $\Omega_{n1}^{'}$ is

$$\iint_{\Omega_{n1}^{'}}\exp\left[i\left(a_{nm}u^{'}+b_{nm}v^{'}\right)\right]du^{'}dv^{'}=\frac{\pi r_{2n}}{2b_{nm}}\exp\left(ia_{nm}u_c^{'}\right)\times$$

$$\times\left(\exp(-i\varphi_{nm})\left\{\mathbf{J}_1\left(r_{2n}q_{nm},\Theta_{nm}^{22+}\right)+\mathbf{J}_1\left(r_{2n}q_{nm},\Theta_{nm}^{22-}\right)+i\left[\mathbf{E}_1\left(r_{2n}q_{nm},\Theta_{nm}^{22+}\right)-\mathbf{E}_1\left(r_{2n}q_{nm},\Theta_{nm}^{22-}\right)\right]\right\}-\right.$$

$$\left.-\exp(i\varphi_{nm})\left\{\mathbf{J}_{-1}\left(r_{2n}q_{nm},\Theta_{nm}^{22+}\right)+\mathbf{J}_{-1}\left(r_{2n}q_{nm},\Theta_{nm}^{22-}\right)+i\left[\mathbf{E}_{-1}\left(r_{2n}q_{nm},\Theta_{nm}^{22+}\right)-\mathbf{E}_{-1}\left(r_{2n}q_{nm},\Theta_{nm}^{22-}\right)\right]\right\}\right). \tag{C38}$$

Though this expression has been deduced for $b_{nm}\neq 0$, it is easy to show that it has a corresponding finite limit at $b_{nm}\to 0$.

C.2. Integration over $\Omega_{m1}^{'}$. For $b_{nm}\neq 0$, the integral over $\Omega_{m1}^{'}$ is calculated similarly; it equals

$$\iint_{\Omega_{m1}^{'}}\exp\left[i\left(a_{nm}u^{'}+b_{nm}v^{'}\right)\right]du^{'}dv^{'}=\int_{u_{d1}}^{r_{2m}}\exp\left(ia_{nm}u^{'}\right)\int_{-\sqrt{r_{2m}^2-u^{'2}}}^{\sqrt{r_{2m}^2-u^{'2}}}\exp\left(ib_{nm}v^{'}\right)dv^{'}du^{'}=$$

$$=\frac{\pi r_{2m}}{2b_{nm}}\times$$

$$\times\left(\exp(i\varphi_{nm})\left\{\mathbf{J}_1\left(r_{2m}q_{nm},\Theta_{mn}^{22+}\right)+\mathbf{J}_1\left(r_{2m}q_{nm},\Theta_{mn}^{22-}\right)-i\left[\mathbf{E}_1\left(r_{2m}q_{nm},\Theta_{mn}^{22+}\right)-\mathbf{E}_1\left(r_{2m}q_{nm},\Theta_{mn}^{22-}\right)\right]\right\}-\right.$$

$$-\exp(-i\varphi_{nm})\times$$

$$\left.\times\left\{\mathbf{J}_{-1}(r_{2m}q_{nm},\Theta_{mn}^{22+})+\mathbf{J}_{-1}(r_{2m}q_{nm},\Theta_{mn}^{22-})-i\left[\mathbf{E}_{-1}\left(r_{2m}q_{nm},\Theta_{mn}^{22+}\right)-\mathbf{E}_{-1}\left(r_{2m}q_{nm},\Theta_{mn}^{22-}\right)\right]\right\}\right), \qquad \text{(C39)}$$

where:

$$\Theta_{mn}^{22\pm}=\Theta_{mn}^{22}\pm\varphi_{nm}, \qquad \text{(C40)}$$

and Θ_{mn}^{22} is defined by (C25).

Appendix D

Derivation of the formula components for the AOTF

Calculation of the average $A(f_u, f_v, \lambda; x_n, y_n, x_m, y_m)$. Using the definitions of the incomplete Anger and Weber functions – Exs. (C32) and (C35), and introducing the index function $T^{gh}_{jl,nm}(f_u, f_v, \lambda; x, y; u, v)$, the function $A(f_u, f_v, \lambda; x_n, y_n, x_m, y_m)$ can be written as

$$A(f_u, f_v, \lambda; x_n, y_n, x_m, y_m) = T^{22}_{nm,nm}(f_u, f_v, \lambda; x, y; u, v) + T^{22}_{mn,nm}(f_u, f_v, \lambda; x, y; -u, -v), \quad \text{(D1)}$$

where:

$$T^{gh}_{jl,nm}(f_u, f_v, \lambda; x, y; u, v) = \frac{2}{\pi}\sqrt{\tau_n \tau_m}\cdot r_{gj}\exp\left\{-i\alpha\left[x_l u_f + y_l v_f - (x_j - x_l)u_j - (y_j - y_l)v_j\right]\right\}\times$$

$$\times\exp\left\{-i\beta_j(u_j x_j + v_j y_j) + i\beta_l(u_l x_l + v_l y_l)\right\}\times$$

$$\times\frac{1}{\alpha\left[c^{12}_{nm}(x_j - x_l) + c^{22}_{nm}(y_j - y_l)\right]}\int_0^{\Theta^{gh}_{jl}}\sin\varphi\cdot\sin\left\{\alpha\left[c^{12}_{nm}(x_j - x_l) + c^{22}_{nm}(y_j - y_l)\right]r_{gj}\sin\varphi\right\}\times$$

$$\times\exp\left\{-i\alpha\left[c^{11}_{nm}(x_j - x_l) + c^{21}_{nm}(y_j - y_l)\right]r_{gj}\cos\varphi\right\}d\varphi. \quad \text{(D2)}$$

Note that we can do some changes in Ex. (D2):

$$(x_j - x_l)u_j + (y_j - y_l)v_j = (x_j - x_l)\left(u_j^0 + \frac{L}{F}x_j\right) + (y_j - y_l)\left(v_j^0 + \frac{L}{F}y_j\right)\approx$$

$$\approx (x_j - x_l)u_j^0 + (y_j - y_l)v_j^0, \tag{D3}$$

$$u_j x_j + v_j y_j \approx u_j^0 x_j + v_j^0 y_j,\ u_l x_l + v_l y_l \approx u_l^0 x_l + v_l^0 y_l. \tag{D4}$$

Besides, the direction cosines c_{nm}^{11}, c_{nm}^{21}, c_{nm}^{12}, and c_{nm}^{22} are present only in conjunction with $(x_j - x_l)$ or $(y_j - y_l)$. Hence we can not account $(x_n - x_m)$ and $(y_n - y_m)$ in Exs. (C5) and (C6) for the direction cosines, i.e. they can be written as:

$$\begin{cases} c_{nm}^{11} \approx \dfrac{u_n^0 + u_f - u_m^0}{\sqrt{(u_n^0 + u_f - u_m^0)^2 + (v_n^0 + v_f - v_m^0)^2}} \\ c_{nm}^{21} \approx \dfrac{v_n^0 + v_f - v_m^0}{\sqrt{(u_n^0 + u_f - u_m^0)^2 + (v_n^0 + v_f - v_m^0)^2}} \end{cases}; \tag{D5}$$

$$\begin{cases} c_{nm}^{12} \approx -\dfrac{v_n^0 + v_f - v_m^0}{\sqrt{(u_n^0 + u_f - u_m^0)^2 + (v_n^0 + v_f - v_m^0)^2}} \\ c_{nm}^{22} \approx \dfrac{u_n^0 + u_f - u_m^0}{\sqrt{(u_n^0 + u_f - u_m^0)^2 + (v_n^0 + v_f - v_m^0)^2}} \end{cases}. \tag{D6}$$

Also from these considerations, we suppose that the limit of integration Θ_{jl}^{gh} defined by Ex. (C25) is not dependent on x_n, x_m, y_n, and y_m, i.e. $u_c^{'}$ defined by Ex. (C19) can be written as:

$$u_c^{'} \approx \sqrt{(u_n^0 + u_f - u_m^0)^2 + (v_n^0 + v_f - v_m^0)^2}. \tag{D7}$$

It is obvious from Ex. (D1) that it is enough to find the average for only one member in Ex. (D1). Let it be for $T_{nm,nm}^{22}(f_u, f_v, \lambda; x, y; u, v)$. The calculation of the average $T_{nm,nm}^{22}(f_u, f_v, \lambda; x, y; u, v)$ is divided into two types: 1) $n \neq m$, and 2) $n = m$.

D.1. Calculation of the average $T^{22}_{nm,nm}(f_u, f_v, \lambda; x, y; u, v)$ *for* $n \neq m$. Denoting the average expression as

$$V^{22}_{nm,nm}(f_u, f_v, \lambda; u, v) =$$

$$= \int_{-\infty}^{+\infty}\int\int_{-\infty}^{+\infty}\int T^{22}_{nm,nm}(f_u, f_v, \lambda; x, y; u, v) p(x_n, y_n) dx_n dy_n p(x_m, y_m) dx_m dy_m , \quad \text{(D8)}$$

we have:

$$V^{22}_{nm,nm}(f_u, f_v, \lambda; u, v) =$$

$$= \frac{1}{2\pi\sigma_{x_n}\sigma_{y_n}\sqrt{1-\rho^2_{x_n y_n}}} \cdot \frac{1}{2\pi\sigma_{x_m}\sigma_{y_m}\sqrt{1-\rho^2_{x_m y_m}}} \cdot \int_{-\infty}^{+\infty}\int\int_{-\infty}^{+\infty}\int T^{22}_{nm,nm}(f_u, f_v, \lambda; x, y; u, v) \times$$

$$\times \exp\left\{-\frac{1}{2(1-\rho^2_{x_n y_n})}\left[\frac{(x_n - \bar{x}_n)^2}{\sigma^2_{x_n}} - \frac{2\rho_{x_n y_n}(x_n - \bar{x}_n)(y_n - \bar{y}_n)}{\sigma_{x_n}\sigma_{y_n}} + \frac{(y_n - \bar{y}_n)^2}{\sigma^2_{y_n}}\right]\right\} \times$$

$$\times \exp\left\{-\frac{1}{2(1-\rho^2_{x_m y_m})}\left[\frac{(x_m - \bar{x}_m)^2}{\sigma^2_{x_m}} - \frac{2\rho_{x_m y_m}(x_m - \bar{x}_m)(y_m - \bar{y}_m)}{\sigma_{x_m}\sigma_{y_m}} + \frac{(y_m - \bar{y}_m)^2}{\sigma^2_{y_m}}\right]\right\} \times$$

$$\times dx_n dy_n dx_m dy_m . \quad \text{(D9)}$$

This expression can be calculated using the following procedure. Let

$$V^{22}_{nm,nm}(f_u, f_v, \lambda; u, v) = \int_{-\infty}^{+\infty}\int\int_{-\infty}^{+\infty}\int G_4(x_n, y_n, x_m, y_m) dx_n dy_n dx_m dy_m , \quad \text{(D10)}$$

where $G_4(x_n, y_n, x_m, y_m)$ is an appropriate function from Ex. (D9). Introducing the new variables

$$x_1 = x_n, \quad x_2 = x_n - x_m, \quad y_1 = y_n, \quad y_2 = y_n - y_m ; \quad \text{(D11)}$$

and integrating Ex. (D10) over x_1, we have

$$V^{22}_{nm,nm}(f_x, f_y, \lambda; u, v) =$$

$$= \sqrt{\frac{\pi}{A_1}} \cdot \exp\left[\frac{(B_1 + C_1 y_1 + D_1 x_2 + E_1 y_2)^2}{4A_1}\right] \cdot \int_{-\infty}^{+\infty}\int\int G_3(y_1, x_2, y_2) dy_1 dx_2 dy_2 , \qquad \text{(D12)}$$

where:

$$A_1 = S_{x_n} + S_{x_m} ,$$

$$B_1 = 2S_{x_n}\bar{x}_n + 2S_{x_m}\bar{x}_m - S_{x_n y_n}\bar{y}_n - S_{x_m y_m}\bar{y}_m - i\alpha u_f - i\beta_n u_n^0 + i\beta_m u_m^0 ,$$

$$C_1 = S_{x_n y_n} + S_{x_m y_m} \qquad D_1 = 2S_{x_m} , \qquad E_1 = -S_{x_m y_m} ,$$

$$S_{x_n} = \frac{1}{2\sigma_{x_n}^2\left(1-\rho_{x_n y_n}^2\right)}, \quad S_{x_n y_n} = \frac{\rho_{x_n y_n}}{\sigma_{x_n}\sigma_{y_n}\left(1-\rho_{x_n y_n}^2\right)}, \quad S_{y_n} = \frac{1}{2\sigma_{y_n}^2\left(1-\rho_{x_n y_n}^2\right)},$$

$$S_{x_m} = \frac{1}{2\sigma_{x_m}^2\left(1-\rho_{x_m y_m}^2\right)}, \quad S_{x_m y_m} = \frac{\rho_{x_m y_m}}{\sigma_{x_m}\sigma_{y_m}\left(1-\rho_{x_m y_m}^2\right)}, \quad S_{y_m} = \frac{1}{2\sigma_{y_m}^2\left(1-\rho_{x_m y_m}^2\right)}; \qquad \text{(D13)}$$

and $G_3(y_1, x_2, y_2)$ is an appropriate function from Ex. (D10). Integrating Ex. (D12) over y_1, we have

$$V_{nm,nm}^{22}(f_u, f_v, \lambda; u, v) =$$

$$= \sqrt{\frac{\pi}{A_1}}\sqrt{\frac{\pi}{A_2}} \cdot \exp\left(\frac{B_1^2}{4A_1}\right) \cdot \int_{-\infty}^{+\infty}\int \exp\left[\frac{(B_2 + D_2 x_2 + E_2 y_2)^2}{4A_2}\right] G_2(x_2, y_2) dx_2 dy_2 , \qquad \text{(D14)}$$

where:

$$A_2 = S_{y_n} + S_{y_m} - \frac{C_1^2}{4A_1} ,$$

$$B_2 = 2S_{y_n}\bar{y}_n + 2S_{y_m}\bar{y}_m - S_{x_n y_n}\bar{x}_n - S_{x_m y_m}\bar{x}_m - i\alpha v_f - i\beta_n v_n^0 + i\beta_m v_m^0 + \frac{B_1 C_1}{2A_1} ,$$

$$D_2 = -S_{x_m y_m} + \frac{C_1 D_1}{2A_1}, \quad E_2 = 2S_{y_m} + \frac{C_1 E_1}{2A_1}, \qquad \text{(D15)}$$

and $G_2(x_2, y_2)$ is an appropriate function from Ex. (D12). Here the integration of Ex. (D14) is divided into two types of integration: 1) $c_{nm}^{12} \neq 0$, and 2) $c_{nm}^{12} = 0$.

D.1.1. Integration for $c_{nm}^{12} \neq 0$. Introducing the new variables x_3 and y_3, making the substitution

$$x_3 = x_2 + \frac{c_{nm}^{22}}{c_{nm}^{12}} y_2, \qquad y_3 = y_2 \tag{D16}$$

in Ex. (D14), and integrating it over y_3, we have

$$V_{nm,nm}^{22}(f_u, f_v, \lambda; u, v) =$$

$$= \sqrt{\frac{\pi}{A_1}} \sqrt{\frac{\pi}{A_2}} \sqrt{\frac{\pi}{A_5}} \cdot \exp\left(\frac{B_1^2}{4A_1} + \frac{B_2^2}{4A_2} \right) \cdot \int_{-\infty}^{+\infty} \exp\left[\frac{(B_5 + C_5 \cos\varphi + D_5 x_3)^2}{4A_5} \right] \cdot G_1(x_2) dx_2, \tag{D17}$$

where:

$$A_5 = A_3 + A_4 a_c^2 + D_3 a_c, \qquad B_5 = B_3 + B_4 a_c, \quad C_5 = i\alpha b_c r_n, \quad D_5 = 2A_4 a_c + D_3;$$

$$a_c = \frac{c_{nm}^{22}}{c_{nm}^{12}}, \qquad b_c = \frac{1}{c_{nm}^{12}};$$

$$A_4 = S_{x_m} - \frac{D_1^2}{4A_1} - \frac{D_2^2}{4A_2},$$

$$B_4 = -2S_{x_m} \bar{x}_m + S_{x_m y_m} \bar{y}_m + i\alpha(u_n^0 + u_f) - i\beta_m u_m^0 + \frac{B_1 D_1}{2A_1} + \frac{B_2 D_2}{2A_2},$$

$$A_3 = S_{y_m} - \frac{E_1^2}{4A_1} - \frac{E_2^2}{4A_2},$$

$$B_3 = -2S_{y_m} \bar{y}_m + S_{x_m y_m} \bar{x}_m + i\alpha(v_n^0 + v_f) - i\beta_m v_m^0 + \frac{B_1 E_1}{2A_1} + \frac{B_2 E_2}{2A_2},$$

$$D_3 = S_{x_m y_m} + \frac{D_1 E_1}{2A_1} + \frac{D_2 E_2}{2A_2}, \tag{D18}$$

and $G_1(x_2)$ is an appropriate function from Ex. (D14). The last integration in Ex. (D17) gives us the final result for $c_{nm}^{12} \neq 0$:

$$V_{nm,nm}^{22}(f_u, f_v, \lambda; u, v) = \frac{1}{4\alpha\sqrt{\pi}} \frac{1}{\sigma_{x_n}\sigma_{y_n}\sqrt{1-\rho_{x_n y_n}^2}} \frac{1}{\sigma_{x_m}\sigma_{y_m}\sqrt{1-\rho_{x_m y_m}^2}} \times$$

$$\times \frac{\sqrt{\tau_n \tau_m} \cdot r_{2n}}{c_{nm}^{12}\sqrt{A_1 A_2 A_5}} \times$$

$$\times \exp\left[-\left(S_{x_n}\bar{x}_n^2 + S_{y_n}\bar{y}_n^2 + S_{x_m}\bar{x}_m^2 + S_{y_m}\bar{y}_m^2\right) + S_{x_n y_n}\bar{x}_n\bar{y}_n + S_{x_m y_m}\bar{x}_m\bar{y}_m + \frac{B_1^2}{4A_1} + \frac{B_2^2}{4A_2} + \frac{B_5^2}{4A_5}\right] \times$$

$$\times \int_0^{\Theta_{nm}^{22}} \sin\varphi \exp\left[\frac{(C_5\cos\varphi + 2B_5)C_5\cos\varphi}{4A_5}\right] \times$$

$$\times \left\{\operatorname{erf}\left[\frac{D_6\sin\varphi - i(B_6 + C_6\cos\varphi)}{2\sqrt{A_6}}\right] + \operatorname{erf}\left[\frac{D_6\sin\varphi + i(B_6 + C_6\cos\varphi)}{2\sqrt{A_6}}\right]\right\} d\varphi, \quad \text{(D19)}$$

where:

$$A_6 = A_4 - \frac{D_5^2}{4A_5}, \quad B_6 = B_4 + \frac{B_5 D_5}{2A_5}, \quad C_6 = -i\alpha c_{nm}^{11} r_n + \frac{C_5 D_5}{2A_5}, \quad D_6 = \alpha c_{nm}^{12} r_n. \quad \text{(D20)}$$

D.1.2. Integration for $c_{nm}^{12} = 0$. Integrating Ex. (D14) over x_2, we have

$$V_{nm,nm}^{22}(f_u, f_v, \lambda; u, v) =$$

$$= \sqrt{\frac{\pi}{A_1}}\sqrt{\frac{\pi}{A_2}}\sqrt{\frac{\pi}{A_4}} \cdot \exp\left(\frac{B_1^2}{4A_1} + \frac{B_2^2}{4A_2}\right) \cdot \int_{-\infty}^{+\infty} \exp\left[\frac{(B_4 + C_4\cos\varphi + D_3 y_2)^2}{4A_4}\right] \cdot H_1(y_2) dy_2, \quad \text{(D21)}$$

where:

$$C_4 = -i\alpha r_n, \quad \text{(D22)}$$

and $H_1(y_2)$ is an appropriate function from Ex. (D14). Finally, the integration of Ex. (D21) gives:

$$V_{nm,nm}^{22}(f_u,f_v,\lambda;u,v)=\frac{1}{4\alpha\sqrt{\pi}}\frac{1}{\sigma_{x_n}\sigma_{y_n}\sqrt{1-\rho_{x_ny_n}^2}}\frac{1}{\sigma_{x_m}\sigma_{y_m}\sqrt{1-\rho_{x_my_m}^2}}\frac{\sqrt{\tau_n\tau_m}\cdot r_{2n}}{\sqrt{A_1A_2A_4}}\times$$

$$\times\exp\left[-\left(S_{x_n}\bar{x}_n^2+S_{y_n}\bar{y}_n^2+S_{x_m}\bar{x}_m^2+S_{y_m}\bar{y}_m^2\right)+S_{x_ny_n}\bar{x}_n\bar{y}_n+S_{x_my_m}\bar{x}_m\bar{y}_m+\frac{B_1^2}{4A_1}+\frac{B_2^2}{4A_2}+\frac{B_4^2}{4A_4}\right]\times$$

$$\times\int_0^{\Theta_{nm}^{22}}\sin\varphi\exp\left[\frac{(C_4\cos\varphi+2B_4)C_4\cos\varphi}{4A_4}\right]\times$$

$$\times\left\{\operatorname{erf}\left[\frac{D_7\sin\varphi-i(B_7+C_7\cos\varphi)}{2\sqrt{A_7}}\right]+\operatorname{erf}\left[\frac{D_7\sin\varphi+i(B_7+C_7\cos\varphi)}{2\sqrt{A_7}}\right]\right\}d\varphi, \qquad \text{(D23)}$$

where:

$$A_7=A_3-\frac{D_3^2}{4A_4},\quad B_7=B_3+\frac{B_4D_3}{2A_4},\ C_7=\frac{C_4D_3}{2A_4},\qquad D_7=\alpha r_n. \qquad \text{(D24)}$$

D.2. Calculation of the average $T_{nm,nm}^{22}(f_u,f_v,\lambda;x,y;u,v)$ *for* $n=m$. In this case,

$$T_{nn,nn}^{22}(f_u,f_v,\lambda;x,y;u,v)=\frac{2}{\pi}\tau_n r_{2n}^2\exp\left\{-i\alpha\left[x_nu_f+y_nv_f\right]\right\}\cdot\int_0^{\Theta_{nn}^{22}}\sin^2\varphi d\varphi=$$

$$=\frac{1}{\pi}\tau_n r_{2n}^2\exp\left[-i\alpha\left(x_nu_f+y_nv_f\right)\right]\cdot\left(\Theta_{nn}^{22}-\cos\Theta_{nn}^{22}\cdot\sin\Theta_{nn}^{22}\right). \qquad \text{(D25)}$$

Denoting the average expression as

$$V_{nn,nn}^{22}(f_u,f_v,\lambda;u,v)=\int_{-\infty}^{+\infty}\int T_{nn,nm}^{22}(f_u,f_v,\lambda;x,y;u,v)p(x_n,y_n)dx_ndy_n, \qquad \text{(D26)}$$

we have:

$$V_{nn,nn}^{22}(f_u,f_v,\lambda;u,v)=\frac{1}{2\pi\sigma_{x_n}\sigma_{y_n}\sqrt{1-\rho_{x_ny_n}^2}}\cdot\int_{-\infty}^{+\infty}\int T_{nn,nn}^{22}(f_u,f_v,\lambda;x,y;u,v)\times$$

$$\times\exp\left\{-\frac{1}{2\left(1-\rho_{x_ny_n}^2\right)}\left[\frac{(x_n-\bar{x}_n)^2}{\sigma_{x_n}^2}-\frac{2\rho_{x_ny_n}(x_n-\bar{x}_n)(y_n-\bar{y}_n)}{\sigma_{x_n}\sigma_{y_n}}+\frac{(y_n-\bar{y}_n)^2}{\sigma_{y_n}^2}\right]\right\}dx_ndy_n=$$

$$= \frac{1}{2\pi\sigma_{x_n}\sigma_{y_n}\sqrt{1-\rho^2_{x_n y_n}}} \frac{\tau_n r^2_{2n}}{\sqrt{A_8 A_9}} \times$$

$$\times \exp\left[-S_{x_n}\bar{x}_n^2 + S_{x_n y_n}\bar{x}_n\bar{y}_n - S_{y_n}\bar{y}_n^2 + \frac{B_8^2}{4A_8} + \frac{B_9^2}{4A_9} \right] \cdot \left(\Theta^{22}_{nn} - \cos\Theta^{22}_{nn} \cdot \sin\Theta^{22}_{nn} \right), \quad \text{(D27)}$$

where:

$$A_8 = S_{x_n}, \qquad B_8 = 2S_{x_n}\bar{x}_n - S_{x_n y_n}\bar{y}_n - i\alpha u_f, \qquad C_8 = S_{x_n y_n};$$

$$A_9 = S_{y_n} - \frac{C_8^2}{4A_8}, \qquad B_9 = 2S_{y_n}\bar{y}_n - S_{x_n y_n}\bar{x}_n - i\alpha v_f + \frac{B_8 C_8}{2A_8}; \quad \text{(D28)}$$

and values S_{x_n}, $S_{x_n y_n}$, S_{y_n} are defined by Exs. (D13).

Calculation of the average $B(\lambda, \Delta_n, \Delta_m)$. The average $B(\lambda, \Delta_n, \Delta_m)$ is calculated in accordance with the following simple formulas:

1) for $n \neq m$

$$Q_{nm}(\lambda) = \int_{-\infty-\infty}^{+\infty+\infty} B(\lambda, \Delta_n, \Delta_m) p(\Delta_n) d\Delta_n \, p(\Delta_m) d\Delta_m = \frac{1}{\sqrt{2\pi\sigma^2_{\Delta_n}}} \frac{1}{\sqrt{2\pi\sigma^2_{\Delta_m}}} \times$$

$$\times \int_{-\infty-\infty}^{+\infty+\infty} \exp[ik(\Delta_n - \Delta_m)] \exp\left\{ -\frac{(\Delta_n - \bar{\Delta}_n)^2}{2\sigma^2_{\Delta_n}} \right\} d\Delta_n \exp\left\{ -\frac{(\Delta_m - \bar{\Delta}_m)^2}{2\sigma^2_{\Delta_m}} \right\} d\Delta_m =$$

$$= \exp\left[-\frac{k^2}{2}\left(\sigma^2_{\Delta_n} + \sigma^2_{\Delta_m}\right) + ik\left(\bar{\Delta}_n - \bar{\Delta}_m\right) \right]; \quad \text{(D29)}$$

2) for $n = m$

$$Q_{nn}(\lambda) = \int_{-\infty-\infty}^{+\infty+\infty} B(\lambda, \Delta_n, \Delta_n) p(\Delta_n) d\Delta_n \equiv 1. \quad \text{(D30)}$$

References

R1. I. S. Gradshteyn and I. M. Ryzhik, *Table of Integrals, Series, and Products*, 5th Ed., Academic Press (1994), p. 961.

R2. *Handbook of Mathematical Functions with Formulas, Graphs, and Mathematical Tables*, Ed. by M. Abramowitz and I. A. Stegun (1964), p. 487.

R3. E. L. O'Neill, *Introduction to statistical optics*, Addison-Wesley Pub. Comp., Inc., Reading, Massachusetts, (1963), Chapter 5.